Improvement of a Data-Driven Method for the Simulation of the $\tau\tau$-Mass Shape in $Z \to \tau^+\tau^- \to e^+e^- + 4\nu$ for ATLAS at the LHC

Diplomarbeit
zur Erlangung des akademischen Grades
Diplom-Physiker

CERN-THESIS-2009-148
09/11/2009

vorgelegt von

Patrick Czodrowski

geboren in Mohrungen (Polen)

Institut für Kern- und Teilchenphysik
Fachrichtung Physik
Fakultät für Mathematik und Naturwissenschaften
der Technischen Universität Dresden
2009

1. Gutachter: Prof. Dr. Michael Kobel

2. Gutachter: Prof. Dr. Thomas Cowan

Datum des Einreichens der Arbeit: 09.11.2009

Abstract

At the LHC the b-quark associated Higgs boson production channel, $gb \to b+h/A/H, gg \to b\bar{b}+h/A/H, b\bar{b} \to h/A/H$, is one of the most relevant search channels for the supersymmetric Higgs bosons. In particular a largetan β value would enhance the neutral Higgs bosons decay into a τ-lepton pair significantly. For low Higgs boson masses ($m_{h/A/H} \leqslant 140\,\mathrm{GeV}$) the $Z \to \tau^+\tau^-$ decay presents an irreducible background, due to its similar kinematics. In this thesis, a data-driven method for the simulation of the $\tau\tau$-mass distribution in $Z \to \tau^+\tau^- \to e^+e^- + 4\nu$ for the ATLAS detector at the LHC is refined. As no collision data is available yet simulated data was used for the study of possible improvements of this method. $Z \to e^+e^-$ data is modified such, that the reconstructed invariant $\tau\tau$ mass spectrum, $m_{\tau\tau}$, simulates the one obtained from $Z \to \tau^+\tau^- \to e^+e^- + 4\nu$ events, this is performed by rescaling of the electron energies. The shape of an electromagnetic shower changes however depending on the energy of the incident particle. This effect is taken into account in this work. An electromagnetic shower shape parametrization was customized for the ATLAS calorimeter geometry for this task. Correction factors were determined and implemented into an algorithm. This procedure results in an invariant mass distribution which reproduces the $Z \to \tau^+\tau^- \to e^+e^- + 4\nu$ distribution from Monte Carlo data within the statistical error. The mass distribution derived this way, agrees well with the $Z \to \tau^+\tau^- \to e^+e^- + 4\nu$ distribution, even after the applying the selection cuts used in $h/A/H \to \tau\tau \to l^+l^- + 4\nu$ analysis.

Kurzfassung

Die b-Quark-assozierte Higgs Boson Produktion, $gb \to b + h/A/H, gg \to b\bar{b} + h/A/H, b\bar{b} \to h/A/H$, ist dder wichtigsten Entdeckungskanäle für supersymmetrische Higgs Bosonen am LHC. Ein großer $\tan\beta$ Wert würde die Wahrscheinlichkeit des Zerfalles eines neutralen Higgs Bosons in ein τ-Leptonen Paar erheblich erhöhen. Für kleine Higgs Boson Massen ($m_{h/A/H} \leqslant 140\,\mathrm{GeV}$) stellt der $Z \to \tau^+\tau^-$ Kanal, aufgrund der ähnlichen Kinematik, einen nicht reduziblen Untergrund dar. In dieser Arbeit wird eine datenbasierte Methode für die Simulation der Form der $\tau\tau$ Massenverteilung des $Z \to \tau^+\tau^- \to e^+e^- + 4\nu$ Untergrundes für den ATLAS-Detektor am LHC verbessert. Da noch keine Kollisionsdaten des LHC zur verfügung stehen, wurde die Studie zurWweiterentwicklung der Methode unter Zuhilfenahme von simulierten Daten durchgeführt. $Z \to e^+e^-$ Daten werden hierzu in ihren Elektronenergien umskaliert, so dass die rekonstruierte Verteilung der invarianten $\tau\tau$-Masse, $m_{\tau\tau}$, die $Z \to \tau^+\tau^- \to e^+e^- + 4\nu$ Verteilung simuliert. Die Form eines elektromagnetischen Schauers ändert sich jedoch abhängig von der Energie des auslösenden Teilchens. Dieser Effekt wird in dieser Arbeit berücksichtigt. Eine Parametrisierung elektromagnetischer Schauer ist für das Kalorimeter des ATLAS Detektors und dessen Geometrie angepasst worden. Daraus erechnete Korrekturfaktoren wurden bestimmt und in einen Algorithmus eingefügt. Die resultierende Verteilung der invarianten Masse gibt die

$Z \to \tau^+\tau^- \to e^+e^- + 4\nu$ Verteilung von Monte Carlo Daten innerhalb der statistischen Fehler wieder. Die so erhaltene Massenverteilung behält ihre gute Übereinstimmung mit der aus der Simulation erhaltenen Massenverteilung von $Z \to \tau^+\tau^- \to e^+e^- + 4\nu$ auch nach Anwendung von in $h/A/H \to \tau\tau \to l^+l^- + 4\nu$ Analysen verwandten Selektionskriterien.

Contents

1 Introduction

Mankind always perceived whatever holds the world together in its inmost folds. Democrit, in the fifth century B.C., suggested that all matter was made of infinitesimally small particles called atoms. In 1897 the British physicist J. J. Thomson [1] discovered the first subatomic particle, the electron. The last century was very fruitful concerning discoveries of new particles. "Who ordered that?" exclaimed the theorist and Nobel Laurent I. I. Rabi upon the discovery of the muon by C. D. Anderson in 1936, who also discovered the positron in 1932 [2, 3, 4]. More particles than needed to describe the visible matter were found as accelerator physics evolved. Order was reestablished in the particle zoo, after M. Gell-Mann [5] and G. Zweig [6] independently claimed in 1964, that most of the known particles at that time were composites of two or three fundamental constituents called quarks. In 1967, the base for the Standard Model (SM) was established by Glashow, Salam and Weinberg, by unification of the electromagnetic and weak forces [7, 8, 9]. The use of symmetry groups proved as very fruitful for particle physics. The Standard Model describes particles and their interactions very precisely. The requirement for local gauge invariance follows massless particles, which poses a conflict to experimental measurements and everyday experience. In order to save the well observed properties of this theory but generate a mass for particles an additional scalar field was introduced by P. Higgs, F. Englert and R. Brout in 1964 [10]. An excellent approval of the SM was the discovery of the electroweak gauge bosons within the predicted mass range in 1983 [11]. In contrast, all attempts to integrate gravity into the SM failed so far. Further questions from observations, which cannot be explained within the SM, arose. This could be a hint that the SM is only the low energy approximation of a more potential theory, which is yet to be found. The anticipated discovery of the Higgs boson would be the missing proof for the mass generating mechanism of the SM. Tevatron and LEP experiments were not able to find it, but set mass constraints on the SM Higgs boson mass: $m_{H_{SM}} > 114.4\,\mathrm{GeV}$ by LEP and an excluded mass region of $m_{H_{SM}} \notin (160 - 170)\,\mathrm{GeV}$ by the combined Tevatron experiments results [12]. The ATLAS detector at the LHC will be able to detect the Higgs boson provided its mass is below 1 TeV. At the present point of time particle physics stands at a crossroad. The further course is to be decided by the results of the LHC experiments, as new physics has to occur at the terascale energy range. Otherwise the unitarity principle would be broken. There are many theories, all possible extensions of the SM, awaiting proof or refutation by experimental data. Supersymmetry uses a further symmetry which could be realized in nature and thereby it doubles the particle content. The Minimal Supersymmetric Standard Model (MSSM) predicts five instead of one Higgs boson. Not

only the Higgs boson, but also many other processes at the high collision energies of the LHC will be able to limit the number of theories and thereby lead the direction for the future of particle physics. An interesting scenario is the MSSM with a low neutral Higgs boson mass. High values of $\tan\beta$, which is the ratio of the vacuum expectation value of the two MSSM Higgs doublets , would increase the decay of these into τ-lepton pairs significantly. Studies in this scenario of the $h/A/H \rightarrow \tau^+\tau^- \rightarrow l^+l^- + 4\nu$ channel proved $Z \rightarrow \tau^+\tau^-$ as an irreducible background process [13]. Due to the high discovery potential of this channel and the known limited accuracy of Monte Carlo (MC) simulation, a special background estimation technique was developed [14]. Based on simulated $Z \rightarrow e^+e^-$ data from the ALTAS detector it performs a reweighting of the calorimeter cell entries, minimizing MC influence, to mimic the $Z \rightarrow \tau^+\tau^- \rightarrow e^+e^- + 4\nu$ background. Several possible improvements for this reweighting method were studied, based on MC data. The longitudinal component of the shower shape showed the greatest potential for improvement and was therefore implemented in the algorithm in form of a correction factor.

An overview of the Standard Model including the Higgs mechanism and Supersymmetry is given in the next chapter, followed by a short description of the LHC and the ATLAS detector. Thereafter a chapter is dedicated to electromagnetic showers and their parametrization. Further a short introduction into the existing reweighting algorithm and a summary of the studied improvement possibilities is given. Then the results in form of invariant Tau pair mass distributions, $m_{\tau\tau}$, are shown. Finally, a conclusion is drawn. An outlook on further improvement and other possible fields of application for this method is given in the last chapter.

2 The Standard Model and Beyond

2.1 The Standard Model and its Limits

2.1.1 Particles, Fields and Forces

The Standard Model (SM) of particle physics is a quantum field theory (QFT) which describes the known particles and their interactions. Based on the gauge symmetry $SU(3)_C \times SU(2)_L \times U(1)_Y$ it is consistent with all available data gathered at high energy physics experiments [7, 8, 9].

Its fundamental particles are fermions carrying a spin of $|s| = \frac{1}{2}$, called leptons and quarks. Both carry electric (Q) as well as weak charge ($\vec{I}$). The quarks have one additional quantum number of the strong force called color (C). The single color charges are named red, green, blue, with corresponding anti-colors. As a results of the required local gauge symmetry forces are mediated by exchange of particles carrying an integer spin, which are called gauge bosons. The photon, γ, is the exchange particle of the electromagnetic force. Since the photon mass is zero the electromagnetic force has infinite range. Weak forces are mediated via $W^{\pm}$ and Z^0 bosons. The weak charge, $\vec{I}$, was introduced similar to the strong isospin to correctly describe this interaction. Charged and neutral weak interactions exist. The names were given historically depending if the electric charge of a particles changed by one unit during the interaction or not. Mediators of the charged weak force, $W^{\pm}$, couple to left chiral particles and right chiral antiparticles only. A useful tool to connect the third component of the weak with the electrical charge is the Gell-Mann-Nishijima formula, introducing the hypercharge, Y, important for the Glashow-Weinberg-Salam theory

$$Q = \frac{Y}{2} + I_3^W. \tag{2.1}$$

Due to its very short range the weak force got its name. The values of the coupling "constants" do change with the scale of interaction energy, as depicted in Figure 2.1. This effect is called the running of coupling constants. The range of a force can be approximated following the Yukawa hypothesis, which makes use of Heisenbergs uncertainty principle $\Delta x \cdot \Delta p \geq \frac{\hbar}{2}$. Therefore a force range, R_f, can be calculated by $R_f = \frac{\hbar c}{2p}$. Using the $W^{\pm}$ mass, listed in Table 2.2, as input for this equation one finds the range of the weak force in the order of 10^{-18} m. The massless glouns, mediators of the strong force, do not follow this rule. They carry two quantum numbers, one color and one anti-color, leading to eight linear combinations. Due to this, the gluons interact with each other, an effect called self-coupling. A phenomenon which only occurs in non-Abelian gauge theories. This

family or generation			quantum numbers		
I	II	III	I_3^W	Q	Y^W
$\begin{pmatrix}\nu_e\\e^-\end{pmatrix}_L$	$\begin{pmatrix}\nu_\mu\\\mu^-\end{pmatrix}_L$	$\begin{pmatrix}\nu_\tau\\\tau^-\end{pmatrix}_L$	$\begin{pmatrix}+\frac{1}{2}\\-\frac{1}{2}\end{pmatrix}$	$\begin{matrix}0\\-1\end{matrix}$	$\begin{matrix}-1\\-1\end{matrix}$
$\begin{pmatrix}u\\d'\end{pmatrix}_L$	$\begin{pmatrix}c\\s'\end{pmatrix}_L$	$\begin{pmatrix}t\\b'\end{pmatrix}_L$	$\begin{pmatrix}+\frac{1}{2}\\-\frac{1}{2}\end{pmatrix}$	$\begin{matrix}+\frac{2}{3}\\-\frac{1}{3}\end{matrix}$	$\begin{matrix}+\frac{1}{3}\\+\frac{1}{3}\end{matrix}$
ν_{e_R}	ν_{μ_R}	ν_{τ_R}	0	0	0
e_R^-	μ_R^-	τ_R^-	0	-1	-2
u_R	c_R	t_R	0	$+\frac{2}{3}$	$+\frac{4}{3}$
d'_R	s'_R	b'_R	0	$-\frac{1}{3}$	$-\frac{2}{3}$

Table 2.1: Fermions ordered in electroweak multiplets with selected quantum numbers.

results in confinement: no particle carrying a color charge can be observed above a length of 10^{-15} m, which is about the size of a nucleus. The field theory describing interactions of the colored particles is the quantum chromo dynamics (QCD). Color neutral mesons are

interaction	boson	mass	Q	R_f
electromagnetic	γ	$< 10^{-18}$ eV	0	∞
neutral weak	Z	91.19 GeV	0	10^{-18} m
charged weak	$W^\pm$	80.40 GeV	±1	10^{-18} m
strong	g	< 20 MeV	0	10^{-15} m

Table 2.2: Gauge Bosons of the Standard Model of particle physics, masses or their upper limits are determinated by experimental data [16, 17, 18].

made up of a quark pair, one carrying a color and the other the corresponding anticolor. Baryons consist of three quarks each having one of the three different either colors or anticolors. Confinement is also the reason for hadronisation of quarks and glouns in high energy interactions, which leads to jets of hadronic particles.

Leptons and quarks are grouped into iso-duplets and singlets. These are arranged in three families or generations according to their mass. The leptons are paired up in one carrying electric charge, like the electron e^-, the muon μ^-, the tau τ^- and their weak interacting partners, the electron, muon and tau neutrinos, ν_e, ν_μ, ν_τ. As the left chiral fermions and their partners have the same weak quantum number they are sorted into electroweak multiplets, depicted in Table 2.1. The quark pairs consist of one up- and one down-type quark, named after the first generation quarks, which carry an electric charge of

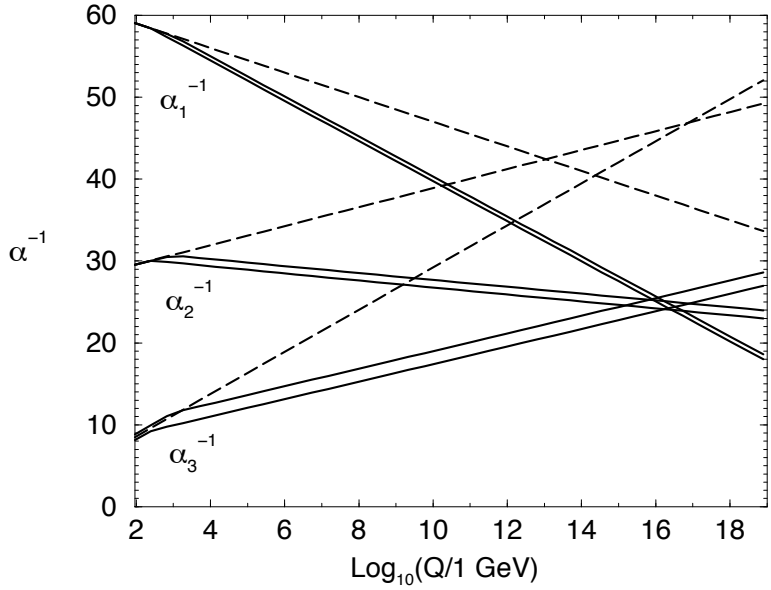

Figure 2.1: Evolution of the inverse gauge couplings α^{-1} in the Standard Model (dashed) and the MSSM (solid lines, with sparticle mass tresholds between 250 GeV and 1 TeV, also $\alpha_3(m_Z)$ between 0.113 and 0.123) [15].

$+\frac{2}{3}$ and $-\frac{1}{3}$, respectively. Charm and strange are the names given to the second generation quarks. Top and bottom, sometimes called truth and beauty, are the quarks belonging to the third generation. The top quark stands out, as it is heavier then the weak gauge bosons ($m_{top} > m_{W^\pm}, m_{Z^0}$). Due to this high mass it decays faster than the formation of a $t\bar{t}$ bound state. Top quark studies could therefore reveal the nature of "free" quarks.
Most of the visible matter in the universe consists of the first fermion generation. All

family	lepton	mass (MeV)	Q	generation	quark	mass (MeV)	Q
I	e^-	0.5110	-1	I	u	1.5-3.3	$+\frac{2}{3}$
	ν_e	< 0.002	0		d	3.5-6.0	$-\frac{1}{3}$
II	μ^-	105.7	-1	II	c	1270	$+\frac{2}{3}$
	ν_μ	< 0.19	0		s	104	$-\frac{1}{3}$
III	τ^-	1777	-1	III	t	171200	$+\frac{2}{3}$
	ν_τ	< 18.2	0		b	4200	$-\frac{1}{3}$

Table 2.3: Fermions of the Standard Model of particle physics [16].

fermions from the 2^{nd} and 3^{rd} generations and therefore higher masses, as listed in Table 2.3, decay to the lightest stable quark or lepton, respecting the conservation of lepton or baryon number. Recent neutrino experiments confirm that neutrinos are massive particles.

The neutrino mass eigenstates are not equal to their electroweak ones, quite similar to the quarks. A consequence is neutrino oscillation as predicted by Pontecorvo [19, 20, 21, 22]. The Pontecorvo-Maki-Nakagawa-Sakata- (PMNS-) matrix provides a relation between the mass and electroweak eigenstates of the neutrinos. The Cabibbo-Kobayashi-Maskawa- (CKM-) matrix does the same for the quarks [23]. The imaginary phase in the CKM-matrix is very important, because it is the source of CP-violation and a small contribution to the imbalance between matter and antimatter in the universe. Oscillations are observed in $D\bar{D}$ and $B\bar{B}$ systems. These are measured and studied by the BaBar and KEK experiments to exactly determine the CKM-components and study the source of CP-violation.

2.1.2 Gauge Theory in a Nutshell

The unification of the electromagnetic and weak force was accomplished by S. L. Glashow, A. Salam and S. Weinberg (GSW) [7, 8, 9]. An important step for this procedure was that the weak neutral and charged currents taken together form the symmetry group $SU(2)_L \times U(1)_Y$. The subscript L indicates that the weak isospin current only couples to lefthanded fermions and righthanded antifermions. It originates from the "vector minus axial" (V-A) nature of the charged currents [24]. A weak isospin singlet, was called weak hypercharge current. The hypercharge Y was defined by the Gell-Mann-Nishijima-Formula (2.1). Thus the symmetry group $SU(2)_L \times U(1)_Y$ contains the electromagnetic and weak interaction. The GSW-theory was very successful, as it relates the masses of the weak gauge bosons to the gauge couplings. Invariance under local gauge transformations of the Lagrangian which describes particle states is considered a basic principle to describe also their interactions. A Lagrangian density, $\mathscr{L}$, itself cannot be derived from underlying principles, but has to be found and validated using the basic principle of physics and nature: the principle of least action (2.2). It states, that the action S during transition of a physical system between two states has to be minimal. In case of quantum field theories S is a functional of the Lagrangian density $\mathscr{L}$.

$$S = \int_{state_1}^{state_2} \mathrm{d}^4x \mathscr{L}(\partial_\mu\psi(x), \partial_\mu\bar{\psi}(x), \psi(x), \bar{\psi}(x)) \tag{2.2}$$

With the Lagrangian of a relativistic massive fermion (2.3) and the Euler-Lagrange formalism (2.4) the Dirac equation (2.5) can be derived. It describes the propagation of a fermion through spacetime.

$$\mathscr{L} = \bar{\psi}(x)(i\partial_\mu\gamma^\mu - m)\psi(x) \tag{2.3}$$

$$\frac{\partial\mathscr{L}}{\partial\bar{\psi}(x)} - \partial_\mu\frac{\partial\mathscr{L}}{\partial(\partial_\mu\bar{\psi}(x))} = 0 \tag{2.4}$$

$$(i\partial_\mu\gamma^\mu - m)\psi(x) = 0, \tag{2.5}$$

where $\psi(x)$ is a Dirac field. It has to be noted, that the field itself is not an observable, but only $|\psi(x)|^2$. Applying a global phase α at all spacetime points x, the gauge transformation on $\psi(x) \rightarrow e^{i\alpha}\psi(x)$ does not change the associated Lagrangian $\mathscr{L}$ (2.3). However when using a local gauge transformation, with $\alpha(x)$ varying at each point of spacetime $\psi(x) \rightarrow e^{i\alpha(x)}\psi(x)$ does change the Lagrangian $\mathscr{L}$, which is not desired. To make the Lagrangian invariant under local gauge transformation a method called minimal coupling is applied. The derivative ∂_μ is replaced by the so called covariant derivative D_μ. This introduces a new field, in this case a vector field, $A_\mu(x)$:

$$\partial_\mu \rightarrow D_\mu(x) = \partial_\mu - ieA_\mu(x). \tag{2.6}$$

The modified Lagrangian $\mathscr{L}'$ is invariant under the local gauge transformation, as terms of the covariant derivative, compensate the troublesome terms. The $A_\mu(x)$ field is interpreted as the field of the photon, γ. A mass term, $\frac{1}{2}M_\gamma^2 A_\mu(x)A^\mu(x)$, would however destroy the just restored local gauge symmetry. The QED Lagrangian for fermions and massless photons is thus given by:

$$\mathscr{L}_{QED} = \bar{\psi}(x)(i\gamma_\mu\partial^\mu - m)\psi(x) - \frac{1}{4}F_{\mu\nu}(x)F^{\mu\nu}(x) + eQ\bar{\psi}(x)\gamma_\mu A^\mu(x)\psi(x), \tag{2.7}$$

with $F_{\mu\nu}$ the the "field strength tensor" defined as [25]

$$F_{\mu\nu}(x) = \partial_\mu A_\nu(x) - \partial_\nu A_\mu(x). \tag{2.8}$$

Fermion masses are added by hand to the Lagrangian $\mathscr{L}_{QED}$. The electroweak Lagrangian $\mathscr{L}_{EW}$ must be extended by the gauge fields $\vec{W}_\mu$ and B_μ of the $SU(2)_L \times U(1)_Y$ group. It is rather troublesome that the requirement for local gauge invariance of $\mathscr{L}_{EW}$ does also not allow any mass terms, neither for the $\vec{W}_\mu$-field and B_μ-field nor the fermions, as the weak interaction couples differently to left and right chiral particles.

$$\mathscr{L}_{EW} = \bar{\chi}_L\gamma^\mu D_\mu\chi_L + \bar{\nu}_R\gamma^\mu D_\mu\nu_R + \bar{e}_R\gamma^\mu D_\mu e_R - \frac{1}{4}\vec{W}_{\mu\nu}\vec{W}^{\mu\nu} - \frac{1}{4}B_{\mu\nu}B^{\mu\nu} \tag{2.9}$$

where

$$D_\mu = i\partial_\mu - g\frac{1}{2}\vec{\tau}\cdot\vec{W}_\mu - g'\frac{Y}{2}B_\mu \tag{2.10}$$

$$\chi_L = \begin{pmatrix} e \\ \nu \end{pmatrix}_L$$

and

$$\vec{W}_{\mu\nu} = \partial_\mu\vec{W}_\nu - \partial_\nu\vec{W}_\mu - gW_\mu \times W_\nu \tag{2.11}$$

$$B_{\mu\nu}(x) = \partial_\mu B_\nu - \partial_\nu B_\mu \tag{2.12}$$

These gauge fields cannot be directly associated with a physical field or particle. The physical neutral current fields, A_μ and Z_μ, identified with the gauge bosons γ and Z^0, are linear combinations of the third component of the $\vec{W}_\mu$-field and the B_μ-field [26]. This mixing of fields is given by the weak mixing angle θ_W:

$$\begin{pmatrix} A_\mu \\ Z_\mu \end{pmatrix} = \begin{pmatrix} \cos\theta_W & \sin\theta_W \\ -\sin\theta_W & \cos\theta_W \end{pmatrix} \cdot \begin{pmatrix} B_\mu \\ W_\mu^3 \end{pmatrix}. \tag{2.13}$$

The weak mixing angle θ_W has an experimentally determined value of $\sin^2(\theta_W) \approx 0.23$. The physical $W^\pm$ bosons are a linear combination of the remaining first and second component of the W_μ-field:

$$W^\pm = \frac{1}{\sqrt{2}}(W_\mu^1 \mp W_\mu^2). \tag{2.14}$$

The masses for the gauge bosons Z^0 and $W^\pm$, as well for fermions, should according the GSW-theory be zero, in contradiction to experiments. The GSW-theory was and still is very successful in describing the electroweak interactions of particles. For instance, interference of the Z^0 and γ in the process $e^-e^+ \to \mu^-\mu^+$ introduces a forward-backward-asymmetry which would not occur if only quantum electrodynamic contributions are considered. This was first discovered by the PETRA experiments [24]. The GSW model has to be extended by a mechanism that generates gauge boson and fermion mass and respects local gauge symmetry.

2.1.3 The Higgs Mechanism of the Standard Model

A thin plastic strip between thumb and index finger will, if force is applied, either curve to the right or the left. These states are ground states of the new system, both break the left-right symmetry [24, 25]. Replacing the strip with a thin rod the step from discrete to continuous symmetry is taken, as a rod can take any bent position as ground state. A simple analogy, which can be used as illustration of spontaneous symmetry breaking. This is the basis of the Higgs mechanism [10]. Breaking the global gauge invariance of a system would, according to the Goldstone theorem result in one or more massless Goldstone bosons [27]. There is no experimental evidence for such bosons. However by breaking the local gauge symmetry the Goldstone bosons can be absorbed by the gauge bosons, gaining an additional degree of freedom. The longitudinal polarization, additionally to the two transverse ones, just what is needed for the bosons to acquire mass [28]. By adding $\mathscr{L}_{Higgs}$ (2.16), invariant under local $SU(2)$ gauge transformations and containing four scalar fields ϕ_i, to $\mathscr{L}_{EW}$ massive gauge bosons can be generated. These fields can be arranged in an isospin doublet Φ with weak hypercharge $Y^W = 1$:

$$\Phi = \begin{pmatrix} \Phi^+ \\ \Phi^0 \end{pmatrix} = \frac{1}{\sqrt{2}} \begin{pmatrix} \phi_1 + i\phi_2 \\ \phi_3 + i\phi_4 \end{pmatrix} \tag{2.15}$$

$$\mathscr{L}_{Higgs} = (D_\mu \Phi)^\dagger (D^\mu \Phi) - V(\Phi) \tag{2.16}$$

$$V(\Phi) = \mu^2 \Phi^\dagger \Phi + \lambda (\Phi^\dagger \Phi)^2, \tag{2.17}$$

where D_μ is the same as in $\mathscr{L}_{EW}$, stated in Equation 2.9. The Higgs potential, $V(\Phi)$, is relevant for mass generation if $\mu^2 < 0$ and $\lambda > 0$ (see Figure 2.2). Only then it acquires a non-trivial minimum with a finite value for $\langle \Phi^\dagger \Phi \rangle = -\frac{\mu^2}{2\lambda}$. Without loss of generality, the field can be expanded pertubatively around the minimum:

$$\Phi_0 = \frac{1}{\sqrt{2}} \begin{pmatrix} 0 \\ v \end{pmatrix}, \tag{2.18}$$

with

$$\phi_3^2 = -\frac{\mu^2}{\lambda} \equiv v^2. \tag{2.19}$$

Relation 2.18 defines the vacuum expectation value v (VEV). Expanding $\Phi(x)$ around the

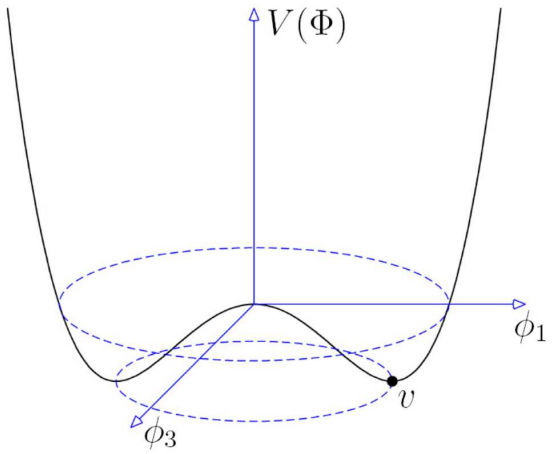

Figure 2.2: The Higgs potential, $V(\Phi)$, as a function of two out of four ϕ_i- fields.

chosen minimum, Φ_0, yields:

$$\Phi_0 = \frac{1}{\sqrt{2}} \begin{pmatrix} 0 \\ v + h(x) \end{pmatrix}. \tag{2.20}$$

Plugging Φ_0 into (2.16) reveals masses for the boson field in the first term: $\frac{g^2 \nu^2}{8}[(W_\mu^2)^2 + (W_\mu^1)^2 + (W_\mu^3)^2]$. The field $h(x)$ is the field of the scalar Higgs boson, H [29]. The masses

of bosons and fermions can be extracted from the complete Lagrangian [24]:

$$\begin{aligned} m_{W^\pm} &= \frac{v}{2}g \\ m_Z &= \frac{v}{2}\sqrt{g^2+g'^2} \\ m_H &= v\sqrt{2\lambda} \\ m_f &= v\frac{\lambda_f}{\sqrt{2}}, \end{aligned}$$

with the Yukawa coupling λ_f in the fermion mass term. These couplings are free parameters proportional to the fermions masses m_f, which therefore cannot be derived from theory. Downtype fermions need an additional Higgs doublet for mass generation, which is the charge conjugated of Φ. The values of g and g' are related to the weak mixing angle θ_W by the formula $g' = g \cdot \tan\theta_W$. The tree level relation of the weak boson masses follows: $M_W = M_Z \cdot \cos\theta_W$. Eventually θ_W and v are related to the Fermi constant G_F, measured in muon decay, via:

$$\frac{1}{2\nu^2} = \frac{G_F}{\sqrt{2}}. \tag{2.21}$$

Its value is experimentally determined to $v = 246\,\mathrm{GeV}$. The masses of the weak bosons were predicted impressively precise even 15 years before their discovery at CERN (Conseil Européen pour la Recherche Nucléaire) in 1983 [11]. To be physically relevant the QFT of the SM has to be renormalizable. This nontrivial proof for the Higgs mechanism extension of the GSW-model was completed by 't Hooft in 1971, approximately four years after the theory was presented originally.
The Higgs boson is the last undiscovered particle of the SM. Theoretical upper bounds of its mass are given at around 1 TeV, where the scattering of longitudinally polarized $W^\pm$ bosons would violate unitarity without another particle appearing in the interaction [30]. An exclusion limit is given by the combined LEP experiments for Higgs masses below 114.4 GeV [31]. Additionally a mass window from 160 GeV to 170 GeV is excluded for the SM Higgs by the combined results of the two Tevatron experiments, CDF and DØ[12]. These limits are visualized by Figure 2.3.

The decay channels of the Higgs boson in the SM depend on its mass [32]. $H \to \gamma\gamma$ gives the possibility of high precision mass measurement, but the branching ration, stays in the per mille region. In the "low mass" range ($100\,\mathrm{GeV} \lesssim m_H \lesssim 130\,\mathrm{GeV}$) decays to $b\bar{b}$ dominate with branching ratios $\sim 50-75\,\%$, followed by $\tau^+\tau^-$ pairs with $\sim 5-7\,\%$. In the mass range ($130\,\mathrm{GeV} \lesssim m_H \lesssim 180\,\mathrm{GeV}$) the $b\bar{b}$ branching ratio would drop to the level of a few percent when the WW-threshold ($m_H \approx 2m_{W^\pm}$) is passed. In the high masses ($m_H \gtrsim 2m_{Z^0}$) the Higgs decays merely to W^+W^- ($\sim \frac{2}{3}$) and Z^0Z^0 ($\sim \frac{1}{3}$). Finally crossing the $2m_t \approx 340\,\mathrm{GeV}$ threshold adds a 20 % $t\bar{t}$ contribution which decreases below 10 % at $m_H \sim 800\,\mathrm{GeV}$.

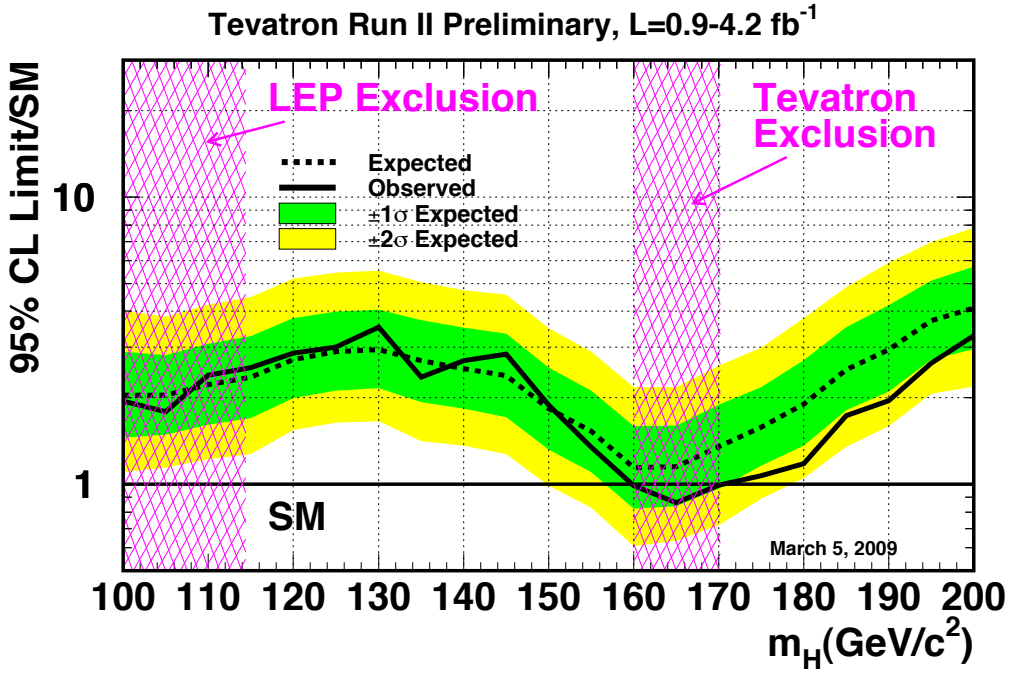

Figure 2.3: SM Higgs mass exclusion by LEP and Tevatron, observed and calculated median of the background only hypothesis. Bands indicate the 68 % and 95 % probability regions. [12]

2.2 Supersymmetry and the MSSM

The SM describes matter particles and interactions down to quantum corrections and at per mille level. Still some problems remain unresolved. For example, dark matter is not explained in the SM, unnatural precise fine tuning of the Higgs mass at Born level, also known as the hierarchy problem, is necessary and gravity is not included. The unification of the three forces, electromagnetic, weak and strong does not occur in the SM. The theory describing such a scenario is called Grand Unified Theory (GUT). The Haag-Łopuszański-Sohnius-theorem [33], an extension of the Coleman-Mandula theorem [34], states, that possible extensions of the standard model, which provide mass gaps, do not necessarily have to be members of the Poincaré group or an internal symmetry. As a nontrivial extension of the Poincaré algebra supersymmetry (SUSY) is a valid possibility. In the following the Minimal Supersymmetric Standard Model (MSSM), a special SUSY model is considered. The generators of SUSY have to satisfy an algebra of anticommutation and commutation relations, with P^μ, the four-momentum generator of spacetime translations, of the form [15]:

$$\{Q, Q^\dagger\} = P^\mu \tag{2.22}$$

$$\{Q, Q\} = \{Q^\dagger, Q^\dagger\} = 0 \tag{2.23}$$

$$[P^\mu, Q] = \left[P^\mu, Q^\dagger\right] = 0 \tag{2.24}$$

This symmetry introduces a superpartner for each SM particle. Applying the operator Q on a fermionic state creates a bosonic state and vice versa.

$$Q|boson\rangle = |fermion\rangle \quad Q|fermion\rangle = |boson\rangle \tag{2.25}$$

The SM field and superpartners created by applying Q belong to a supermultiplet. They have a spin $s_{SUSY} = s_{SM} - \frac{1}{2}$, except the Higgs bosons, where $\frac{1}{2}$ is added. All quantum numbers, these are listed in Table 2.4, except s and all couplings are equal. The nomenclature for SUSY-particles states, that SUSY-bosons or "scalar" fermions get a "s-" as prefix. SUSY-fermions, the gauginos, are indicated with an appendix "-ino". This leads to sparticle names as for example selectron $\widetilde{e}$, the Winos $\widetilde{W}^\pm$ and stop $\widetilde{t}$. The SUSY-particles are marked with a tilde ($\widetilde{}$). Due to effects of electroweak symmetry breaking the higgsinos and electroweak gauginos mix. The charged higgsinos ($\widetilde{h}_u^+$ and $\widetilde{h}_d^-$) and winos ($\widetilde{W}^\pm$) form two mass eigenstates with an electric charge of ± 1, called charginos ($\widetilde{\chi}_i^\pm$). Following this pattern neutral higgsinos ($\widetilde{h}_u^0$ and $\widetilde{h}_d^0$) and neutral gauginos ($\widetilde{W}^0$ and $\widetilde{B}^0$) form four mass eigenstates, the neutralinos ($\widetilde{\chi}_i^0$), as listed in Table 2.5. In most SUSY models the neutralino $\widetilde{\chi}_1^0$ is found as lightest particle. Usually, the indices i are given by increasing sparticle masses. The MSSM states that Higgs doublets mix, forming five mass eigenstates, as three Goldstone bosons are absorbed by Z^0 and $W^\pm$ in order to produce their mass.

Names	$s=0$	$s=\frac{1}{2}$	$(SU(3)_C, SU(2)_L, U(1)_Y$
sleptons,	$(\widetilde{\nu}\ \widetilde{e}_L)$	$(\nu\ e_L)$	$(1, 2, -\frac{1}{2})$
leptons	$\widetilde{e}_R$	e_R	$(1, 1, 1)$
($\times$3 families)			
squarks,	$(\widetilde{u}_L\ \widetilde{d}_L)$	$(u_L\ d_L)$	$(3, 2, \frac{1}{6})$
quarks	$\widetilde{u}_R$	u_R	$(\bar{3}, 1, -\frac{2}{3})$
($\times$3 families)	$\widetilde{d}_R$	d_R	$(\bar{3}, 1, \frac{1}{3})$
Higgs,	$(h_u^+\ h_u^0)$	$(\widetilde{h}_u^+\ \widetilde{h}_u^0)$	$(1, 2, +\frac{1}{2})$
Higgsinos	$(h_d^0\ h_d^-)$	$(\widetilde{h}_d^0\ \widetilde{h}_d^-)$	$(1, 2, -\frac{1}{2})$

Names	$s=\frac{1}{2}$	$s=1$	$(SU(3)_C, SU(2)_L, U(1)_Y$
gluino, gluon	$\widetilde{g}$	g	$(8, 1, 0)$
winos, W bosons	$\widetilde{W}^\pm\ \widetilde{W}^0$	$W^\pm\ W^0$	$(1, 3, 0)$
bino, B boson	$\widetilde{B}^0$	B^0	$(1, 1, 0)$

Table 2.4: Field content of the MSSM [15].

The massive scalar Higgs bosons of the MSSM are therefore:

- h^0 light CP-even
- H^0 heavy CP-even
- $H^\pm$ charged Higgs bosons
- A^0 CP-odd.

Higgs masses, especially h^0 and A^0, as well as $\tan\beta$ are commonly used, the value of $\tan\beta$ is the ratio of VEVs of the two Higgs doublets v_u and v_d:

$$\tan\beta = \frac{v_u}{v_d}. \tag{2.26}$$

The assumed decay fractions of the different Higgs bosons are not determined by their mass alone. A small selection of MSSM scenarios will be given here. The "decoupling regime", with $m_A \gtrsim 150\,\text{GeV}$ for $\tan\beta = 30$ and $m_A \gtrsim 400 - 500\,\text{GeV}$ for $\tan\beta = 3$. The last values result in the highest h^0-mass in this regime. It then follows the decay schema drawn for the SM Higgs [32]. Heavier Higgs bosons decay channels are very sensible to the $\tan\beta$ value. An interesting issue is the strong enhancement of the couplings to the down-type fermions for $\tan\beta \gg 1$, leading to the decay of A^0 and H^0 into almost exclusively $b\bar{b}$ ($\sim 90\,\%$) and $\tau^+\tau^-$ ($\sim 10\,\%$). In "anti-decoupling" regime, $\tan\beta \gtrsim 10$ and $m_A \lesssim m_{h^0}^{max}$, h^0 and A^0 decay via fermions $b\bar{b}$ ($\sim 90\,\%$) and $\tau^+\tau^-$ ($\sim 10\,\%$).

$H^{\pm}$ almost always decays into $\tau^{\pm}\nu_{\tau}$. The "intense-coupling" regime, $\tan\beta \gtrsim 10$ and $m_A \sim 100 - 140\,\text{GeV}$, stands out with a very strong suppression of the neutral Higgs into $\gamma\gamma$ decay, compared to the SM. As the ATLAS detector will operate at the Large Hadron Collider (LHC), the QCD background is predicted to be large. A detailed look at the channel neutral Higgs to $\tau^+\tau^-$ at $\tan\beta = 30$ reveals a further important parameter, μ, from the $\mathscr{L}_{Higgs}$ (2.16). Variations of μ between $-1\,\text{TeV}$ and $1\,\text{TeV}$ lead to branching ratios of the neutral Higgs to $\tau^+\tau^-$ differing by a factor of two.

Names	Spin	P_R	Gauge Eigenstates	Mass Eigenstates
Higgs bosons	0	+1	$h_u^0\ h_d^0\ h_u^+\ h_d^-$	$h^0\ H^0\ A^0\ H^{\pm}$
squarks	0	-1	$\widetilde{u}_L\ \widetilde{u}_R\ \widetilde{d}_L\ \widetilde{d}_R$	(same)
			$\widetilde{s}_L\ \widetilde{s}_R\ \widetilde{c}_L\ \widetilde{c}_R$	(same)
			$\widetilde{t}_L\ \widetilde{t}_R\ \widetilde{b}_L\ \widetilde{b}_R$	$\widetilde{t}_1\ \widetilde{t}_2\ \widetilde{b}_1\ \widetilde{b}_2$
sleptons	0	-1	$\widetilde{e}_L\ \widetilde{e}_R\ \widetilde{\nu}_e$	(same)
			$\widetilde{\mu}_L\ \widetilde{\mu}_R\ \widetilde{\nu}_{\mu}$	(same)
			$\widetilde{\tau}_L\ \widetilde{\tau}_R\ \widetilde{\nu}_{\tau}$	$\widetilde{\tau}_1\ \widetilde{\tau}_2\ \widetilde{\nu}_{\tau}$
Neutralinos	$\frac{1}{2}$	-1	$\widetilde{B}^0\ \widetilde{W}^0\ \widetilde{h}_u^0\ \widetilde{h}_d^0$	$\widetilde{\chi}_1^0\ \widetilde{\chi}_2^0\ \widetilde{\chi}_3^0\ \widetilde{\chi}_4^0$
Charginos	$\frac{1}{2}$	-1	$\widetilde{W}^{\pm}\ \widetilde{h}_u^+\ \widetilde{h}_d^-$	$\widetilde{\chi}_1^{\pm}\ \widetilde{\chi}_2^{\pm}$
gluino	$\frac{1}{2}$	-1	$\widetilde{g}$	(same)
goldstino (gravitino)	$\frac{1}{2}$ ($\frac{3}{2}$)	-1	$\widetilde{G}$	(same)

Table 2.5: Undiscovered particles of the MSSM (with sfermion mixing of the first two families assumed as negligible) [15].

GUT (Grand Unified Theory)

The intersection of the three coupling constants α_i at the energy scale of new physics and below the Planck scale ($M_P = (8\pi G_{Newton})^{-\frac{1}{2}} = 2.4 \times 10^{18}\,\text{GeV}$), would be the first step towards the GUT. M_P is the energy scale where quantum gravitational effects become important for particle interactions. Unfortunately this α_i crossing does not occur in the SM, as the interpolation towards higher interaction energies in Figure 2.1 shows. Due to the additional particle content of MSSM-models the evolution of the coupling constants is modified, such that an intersection of all three forces at interaction energies in the order of the GUT scale ($10^{15}\,\text{GeV}$) seems possible.

Gravity

A globally broken supersymmetry implies the existence of a massless Weyl fermion called the goldstino. With supersymmetry as local symmetry it forms a new theory called supergravity [15]. It contains the superpartner of the graviton, the gravitino with spin $s = \frac{3}{2}$. This sparticle absorbs the goldstino and thereby acquires mass. This, due to its analogy, is called the super-Higgs mechanism. The interactions of the gravitino are suspected to be in the order of gravitational strength, thus will not play a role in present day collider physics. The mass $m_{\frac{3}{2}}$, is expected in the order of some 100 GeV, at least in a "Planck-scale-Mediated Supersymmetry Breaking" (PMSB) scenario, where the gravitino should be in the mass range of other sparticles. Supergravity and some other MSSM scenarios raise hope for an unification of all four forces below M_P.

Dark Matter

Only a few percent of the matter in the universe is made of SM particles. This result is obtained from astronomical observations and calculations concerning the movement of matter that at these scales be should dominated by the gravitational force only. Models show that mass not directly observable has to drive the outer part of galaxies rotation velocity. As stated in the first section of this chapter neutrinos have mass. Calculations using the measured upper limits (see Table 2.3) show neutrinos do not make up dark matter exclusively. They rather are a very small piece of the puzzle. SUSY provides the lightest SUSY particle (LSP), the $\widetilde{\chi}_1^0$ in Table 2.5. It is predicted to be heavier than the neutrinos, the reason for the mass difference will be provided in the following. As this sparticle neither carries strong nor electric charge it can only interact weakly or gravitationaly, thereby making it a promising candidate for cold dark matter (CDM), if it is stable. A new discrete symmetry the R-parity is introduced [35]:

$$P_R = (-1)^{(2s+3B+L)}, \tag{2.27}$$

with L the leptonic, B the baryonic quantum number and s the spin. With this definition SM particles have a R-parity value of 1 and therefore a R-parity of -1 follows for SUSY particles. The decay of the LSP is then prohibited by the R-parity conservation. Further consequence of P_R-conservation is the exclusive SUSY particle production in pairs. The reason for introducing this parity is the superpotential W_{MSSM}, which describes the Yukawa interactions of the MSSM. In its most common form it leads to a renormalizable Lagrangian density which contains Lepton and Baryon number violating terms, that would lead to a fast decay of the proton. Experimentally the proton was found to have a lifetime greater then 10^{31} years. The R-parity conservation suppresses this decay. Another possible scenario is R-parity non-conservation, which leads to a stable proton only if the Yukawa couplings λ' and λ'' are small.

Hierarchy Problem

Measuring the properties of weak interactions provides $\langle H \rangle = \sqrt{\frac{-m_H^2}{2\lambda}} \approx 174\,\text{GeV}$, therefore m_H^2 is very roughly in the order $(100\,\text{GeV})^2$. This m_H^2 receives quantum corrections from all particles interacting with the Higgs field directly and indirectly [36]. Two examples are shown in Figure 2.4. Here f is a massive fermion and couples with a term $\lambda_f H \bar{f} f$ in the Lagrangian and a heavy scalar particle S with mass m_S couples with the term $\lambda_S |H|^2 |S|^2$. This would lead to the following corrections of m_H^2:

$$\Delta m_H^2 = -\frac{|\lambda_f|^2}{8\pi^2} \Lambda_{UV}^2 + \cdots \tag{2.28}$$

$$\Delta m_H^2 = -\frac{|\lambda_S|^2}{16\pi^2} \left[\Lambda_{UV}^2 - 2 m_S \ln\left(\frac{\Lambda_{UV}}{m_S}\right) + \cdots \right]. \tag{2.29}$$

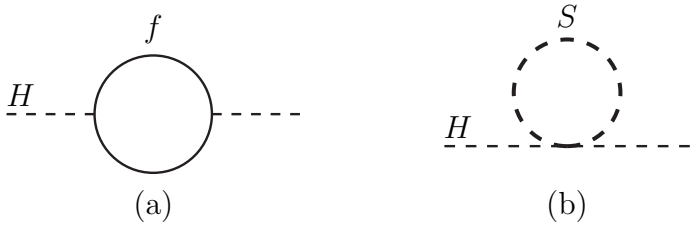

Figure 2.4: One-loop quantum corrections to the Higgs squared mass parameter m_H^2, due to (a) a Dirac fermion f, and (b) a scalar S.

Λ_{UV} is the ultraviolet momentum cutoff, used in QFT to regulate the loop integral, it seems reasonable to replace it with a scale where new physics should appear, for example the GUT scale. Choosing dimensional regularization on the loop integral instead of momentum cutoff, the Λ_{UV} terms vanish. The term containing m_S^2 cannot be eliminated without introducing a counter term meant for this sole purpose. In the momentum cutoff procedure counter terms performing mass tuning at Born level would have to reach a precision within the order of $\frac{m_H^2}{\Lambda^2} \approx 10^{-26}$. SUSY solves this fine tuning problem with its additional particle content, as sparticle mass corrections do have an opposite sign with respect to the fermion loop contributions. The same is true for the boson loops and their SUSY partners. Therefore physically motivated and exact counter terms for the hierarchy problem are generated. The downside of this argument is that there is no experimental evidence for a selectron of the mass 511 keV. This means that supersymmetry has to be broken in the vacuum state. The mass correction then goes like:

$$\Delta m_H^2 \approx O(\alpha) |m_{\tilde{f}}^2 - m_f^2| \approx O(10^{-2}) \cdot m_{SUSY}^2. \tag{2.30}$$

Where m_{SUSY}^2 stands for the SUSY scale, approximately the median masses of its particles, if this mechanism is realized in nature, m_{SUSY} needs to be $\lesssim 1\,\text{TeV}$.

2.2.1 Sources of Supersymmetry Breaking

The Hierarchy problem shows that supersymmetry has to be broken, otherwise it would have already been discovered. A beautiful aspect of the MSSM is that no new parameters except the Yukawa couplings are introduced. This property is lost after the SUSY breaking. In the worst case scenario up to 105 free parameters would have to be introduced. In order to not end up with terms which lead to quadratic divergences supersymmetry breaking must be "soft". Several models for supersymmetry breaking exist, some will be shortly outlined here.

Supersymmetry breaking by non-zero term vacuum expectation value
These non soft breaking models build upon a vacuum state not invariant under supersymmetry caused by a non-vanishing term leading to a non-zero VEV. Such theories are separated into two groups, depending on the form of the non vanishing term. Fayet-Iliopoulos (D-term) breaking introduces a term linear to the auxiliary field of the gauge supermultiplet. If this term drives the breaking, it would have to belong to a $U(1)$. Not the $U(1)_Y$, as this would only break color and/or electromagnetism, but not the supersymmetry. This Ansatz only works if a hidden sector is assumed, in which a yet unknown $U(1)$ symmetry is realized and hardly couples to the visible world. A further problem is that in the D-term breaking scenario it is difficult to give the MSSM sparticles, especially the gauginos, appropriate masses. This downside brought this theory close to being ruled out.
The F-term or O'Raifeartaigh models have brighter phenomenological prospects. These introduce a dimensional ([mass]^2) multiplicative parameter k of a linear chiral supermultiplet term in the superpotential. Although it seems unnatural that k needs to be tiny compared to the Planck scale, to create the right order of magnitude for the soft MSSM breaking, it fulfills most criteria of a physically relevant candidate.
Models with dynamical supersymmetry breaking make use of dimensional transmutation. A new non-Abelian gauge symmetry with gauge coupling, g, being pertubative at M_P is the idea behind this breaking mechanism. Taking QCD as an analogy g gets stronger at smaller scales than the Planck scale.

Hidden sector supersymmetry breaking
These theories assume that the source of symmetry breaking lies in an sector of particles which have no or only very small direct couplings to the "visible" sector. It is therefore called "hidden", a general scheme is provided in Figure 2.5. This category has famous members as the "gravity-mediated", also called the Planck-scale-Mediated Supersymmetry Breaking scenario, as it assumes that near M_P new physics including gravity enters. A special member of this group is the minimal SUperGRAvity, short mSUGRA introducing only 5 additional parameters. The second competing theory family is the "gauge-mediated supersymmetry breaking" (GMSB). In this model the flavor-blind mediating interactions for supersymmetry are the ordinary electroweak and QCD gauge interactions and intro-

duce new chiral multiplets, messenger particles, coupling to a supersymmetry breaking vacuum expectation value.
Further hidden sector SUSY breaking theory members are hidden behind the acronyms XMSB (eXtra-dimensional-Mediated Supersymmetry Breaking) and AMSB (Anomaly-Mediated-Supersymmetry Breaking). Reference [15] provides further details and references.

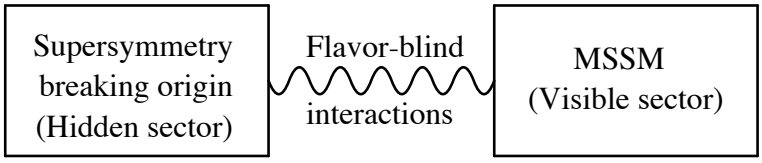

Figure 2.5: Schematic structure for supersymmetry breaking via a hidden sector [15].

3 The ATLAS Experiment at the LHC

3.1 The Large Hadron Collider

The Large Hadron Collider (LHC) is situated at the European Organization for Nuclear Research (CERN). It is located in a tunnel 50 m to 175 m beneath the surface, mostly on the french side of the swiss-french border close to Geneva. Prime motivation to design, accept and construct this enormous project was to find the source of electroweak symmetry breaking, presumably the Higgs field. The LHC machine consists of 1232 dipoles and around 8000 other magnets, as well an immense cryogenic system. With superfluid helium it creates and ensures a working temperature of 1.9 K, necessary for superconducting magnets, otherwise the 8.33 Tesla needed to hold the proton beam were hard to achieve. LEP (Large Electron Positron collider), LHC's predecessor, was abandoned end of 2000 with a peak center of mass energy of 209 GeV to free its 26.659 km long tunnel for the terascale proton-proton collider. A design energy of 7 TeV per proton beam results in a center of mass energy of 14 TeV. This is higher than the Tevatron, a proton-antiproton machine situated at the Fermilab, USA, which currently provides a center of mass energy of 1.96 TeV.

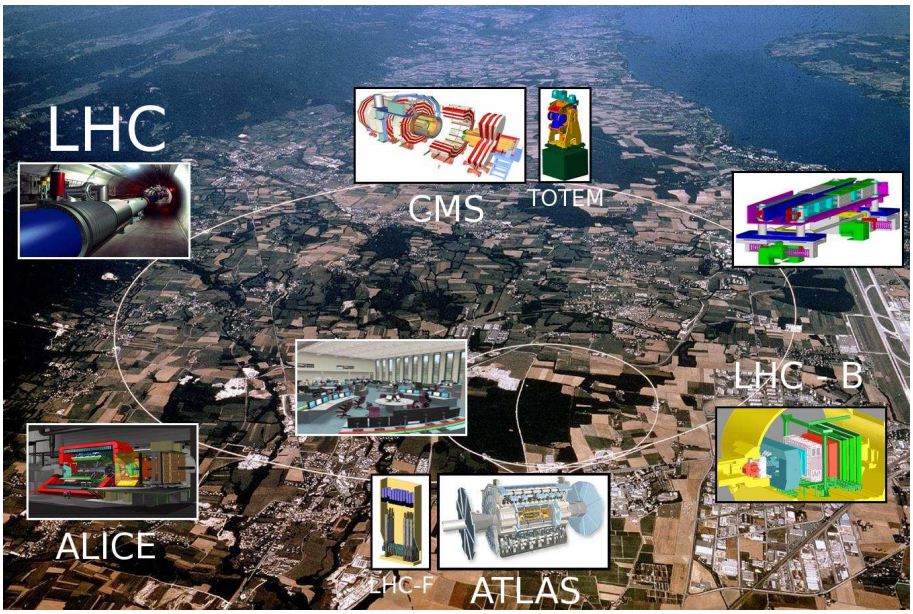

Figure 3.1: The LHC and its experiments.

The LHC started up on 10th of September 2008. Nine days after the first beam passed

the complete ring an accident occurred. A faulty electric connection between two dipoles was the source. This forced the LHC into a long repairing and safety upgrading phase of about one year. Several dipoles and multipoles were brought to the surface to be repaired. Other similar faulty connections were detected and replaced. Next anticipated start up date is the end of November 2009. Due to this major drawback in time the usual winter shutdown at CERN is to be skipped 2009/2010. Further consequence of the incident is that the LHC beam energy schedule was changed. Starting with lower energies, at 3.5 TeV per beam and ramping the energy up slower than originally intended. Increasing to 5 TeV per beam before the winter shutdown in 2010, allowing the magnets and the operation personal a longer training period before the design beam energies are reached. Due to the changed policy it is yet unknown if the design luminosity of $10^{34}\,\frac{1}{\mathrm{cm}^2\mathrm{s}}$ will be reached after three years of operation, as originally planned [37].

The proton beams will be stored in the ring as 2808 bunches, each containing about $110 \cdot 10^9$ protons, with a distance of 25 ns, thus roughly 7 m between each other. Collisions or bunch-crossings will occur at a frequency of 40.08 MHz where the major experiments ATLAS (A Toroidal LHC ApparatuS), CMS (Compact Muon Solenoid), ALICE (A Large Ion Collider Experiment) and LHCb (Large Hadron Collider beauty) are located, compare Figure 3.1. At design luminosity an average of 23 inelastic proton-proton interactions per bunch crossing is anticipated.

The acceleration is not achieved by the LHC alone. A chain of accelerators is involved, which is illustrated in Figure 3.2, with the LINAC (LINear ACcelerator), which provides 50 MeV, as the first step. The following PSB (Proton Synchrotron Booster) passes the beam at 1.4 GeV on to the PS (Proton Synchrotron), which injects it with 26 GeV into the SPS (Super Proton Synchrotron). In 1983 the $W^{\pm}$- and Z^0-boson were discovered at this storage ring. As the last preaccelerator the SPS injects the beam into the LHC with an energy of 450 GeV. The dimensional differences of the SPS, measuring 7 km, to the LHC, former LEP, around 27 km in circumference, are visualized in Figure 3.3.

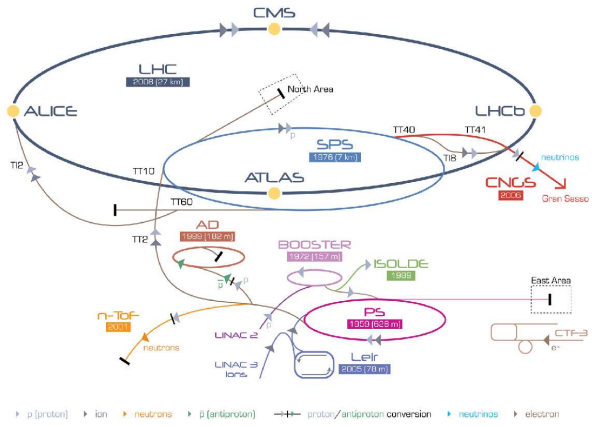

Figure 3.2: The CERN accelerator complex.

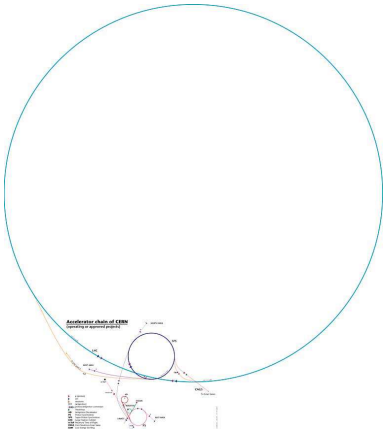

Figure 3.3: The LHC and its preaccelerator system unscaled.

Special operation phases, during which lead ions will be injected into the LHC, are scheduled. The fully stripped Pb^{82+} ions will be accelerated to 2.76 $\frac{\text{TeV}}{\text{u}}$, translating to a center of mass energy of 1.15 PeV. Aim of the ion collision phases is the study of the quark-gluon plasma, a state of the early universe. An upgrade of the LHC to sLHC (super Large Hadron Collider), which amongst others should increase luminosity, is planned for the future. The LHC hosts six experiments, four major ones at interaction points and two forward particle experiments. The latter mentioned are LHCf (Large Hadron Collider forward), consisting of two small detectors each placed at distance 149 m from the ATLAS interaction point and TOTEM (TOTal Elastic and diffractive cross section Measurement), with a total length of 440 m set up close to the CMS detector.

Two general purpose detectors, CMS, with a collaboration of about 2000 scientists and ATLAS, counting around 1800 collaborators, both from 37 countries, were designed for Higgs boson, SUSY-particle and other beyond standard model physics search. This includes extra dimensions and dark matter. The utilized detector techniques distinguish these two experiments. Thus made observations and discoveries can be verified or falsified, like UA1 did with UA2 (Underground Area 1&2) and CDF (Collider Detector at Fermilab) with DØ. CMS is 21 m long, 15 m wide, 15 m high and weights 12.5 t. Its solenoid provides a magnetic field of 4 Tesla, double the field strength of ATLAS. This allows roughly half the size, while keeping a similar muon reconstruction performance [38]. ATLAS in comparison rather is a huge lightweight with 46 m length, 25 m width and 25 m height and weights 7 t. Another significant difference are the implemented electromagnetic calorimeters. ATLAS has a lead liquid argon electromagnetic sampling calorimeter opposed to CMS's novel lead tungstate ($PbWO_4$) crystal technique.

ALICE, a collaboration of over 1000 scientists, had its detector design optimized for physics of the strong force. This includes confinement, quark-gluon plasma, free quarks and gluons, but also the mechanism of mass generation [39].

LHCb, with around 700 active members, wants to collect b-physics relevant data from the LHC collisions. The planar detector is build very close to the beam line to detect forward particles. These have high velocities and therefore should make b-quark decays observable inside the detector [40].

TOTEM, with a comparably small group of around 50 scientists, is build stretching 440 m around the beam pipe, with the aim to observe very forward particles, which the general purpose detectors cannot detect [41]. It will contribute to the luminosity measurement of the LHC and situated close to the CMS detector, their data sets could be used to complement each other.

LHCf's goal is the detection of cascade particles, as initiated by cosmic rays, produced by the LHC collisions. The 22 man group set up two detectors at equal distance from the ATLAS interaction point. Using their and ATLAS data they will be able to verify or improve cosmic particle shower-cascade models, which are of highest importance for terrestrial-based astro-particle-physics experiments [42].

3.2 The ATLAS Detector

Atlas, the titan, son of Japetus and Asia punished by the gods to hold the sky, Uranus, upon his shoulders to prevent it from reuniting with Gaia, the earth. In particle physic circles this name is rather associated with the acronym ATLAS, short hand for "A Toroidal LHC ApparatuS", the largest volume particle detector ever constructed. The logo of the collaboration depicts the titan holding a celestial sphere, also depicted in the lower right corner of Figure 3.4.

Design of the ATLAS detector, as most of the latest multipurpose detectors, is a layer layout with an overall cylindrical shape, as depicted in Figure 3.5. Separated in a central part, the so called barrel and two wheels, called end-caps, to cover the forward and backward region. These provide a good overall detector serviceability. In the barrel components are shaped cylindrical, whereas in the end-caps systems are arranged as discs in the x-y-plane. This separation repeats in each system of the ATLAS detector. Subsystems and particles which they are able to detect are shown in the schema depicted in Figure 3.4. The innermost layer, called inner detector (ID) or tracker, consists of three subsystems and measures momenta of electric charged particles, as the surrounding central solenoid provides a magnetic field with a mean value of 2 Tesla. Energy measurement with high resolution is the main purpose of the electromagnetic (ECAL) and hadronic calorimeters (HCAL). Both designed to fully absorb the particles belonging to the main interaction group they are named after. Muons passing all these layers with only a small energy loss will be precisely measured by the muon spectrometer. Together with the air core toroid magnets it is responsible for ATLAS vast spacial extension.

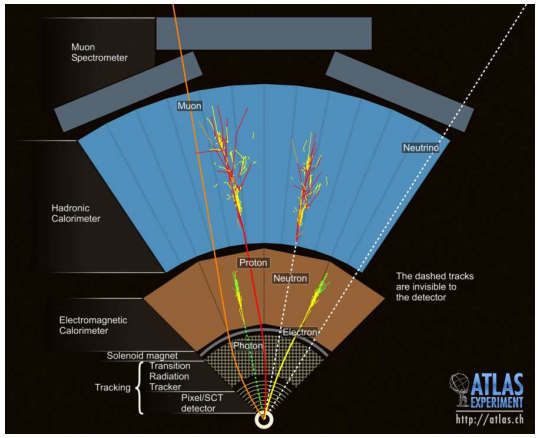

Figure 3.4: Schematic view of the layers of the ATLAS detector, also showing a selection of particles and in which part they will be detected.

Design precisions, resolutions and efficiencies, for the subdetectors to fulfill, were calculated to maximize the discovery potential of new physics. Most systems outperform

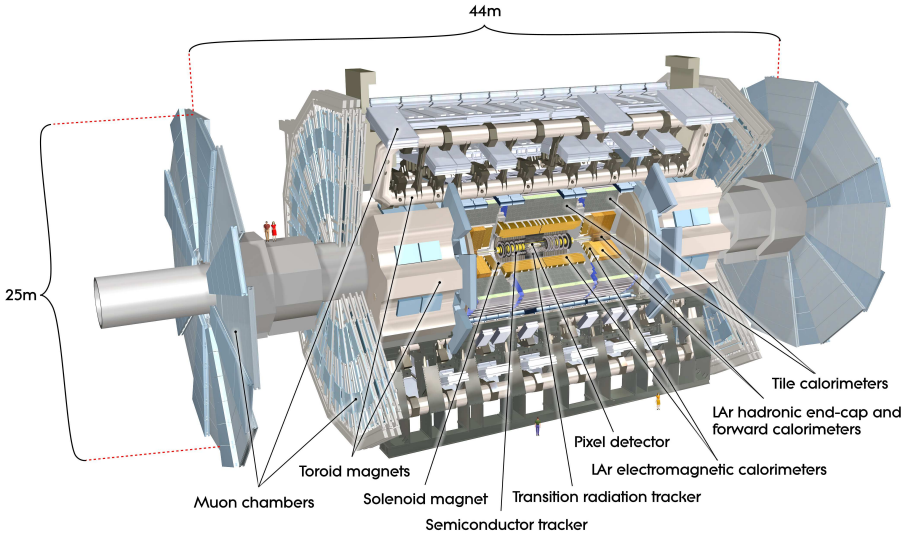

Figure 3.5: Cut-away view of the ATLAS detector showing all subsystems.

these numbers. At the design luminosity of the LHC a mean of 23 inelastic proton-proton collisions per bunch-crossing will occur. The ATLAS detector occupancy will stay below $2-3\,\%$, thus decreasing the impact of pile-up. The term pile-up describes signals created by particles or their secondaries from different $p-p$ collisions, superimposing in the detector. The probability for such events will rise after the sLHC upgrade. Parts of the experiments collaborations are researching techniques to gain control of this future issue. A further important and challenging detail of the detector design was the avoidance cracks. Particles of interest, except neutrinos, should not escape undetected. Cracks pointing back towards the interaction point were successfully obviated. A short description of the subdetectors and the magnet system is given in the following sections.

The origin of the ATLAS detector coordinate system is the interaction point (IP). In right-handed Cartesian coordinates the positive x-axis is defined pointing towards the center of the LHC ring, the positive y-axis points towards the surface. Therefore the z-axis follows the direction of the beam pipe. Cylindrical coordinates are used to describe a particle position, as this reflects the detector geometry. Protons consist of subparticles, called partons, shorthand for gluons and quarks. These partons, are the interacting particles during a collision, carry an unknown fraction of the proton momentum. Conservation of momentum in the transverse plane motivates the usage of transverse momentum, p_T, defined as:

$$p_T = \sqrt{p_x^2 + p_y^2}.$$

The polar angle, θ, measured from the positive z-axis to the particle, helps to define the pseudorapidity η, illustrated in Figure 3.6:

$$\eta = -\ln\left[\tan\left(\frac{\theta}{2}\right)\right].$$

Reason for using η is its feature, that the produced number of QCD events, as a function of η is approximately a constant. The azimuthal angle $\phi = 0$ corresponds to the positive x-axis. ϕ increases clock-wise looking in the positive z-direction and is measured in a range from $-\pi$ to $+\pi$.

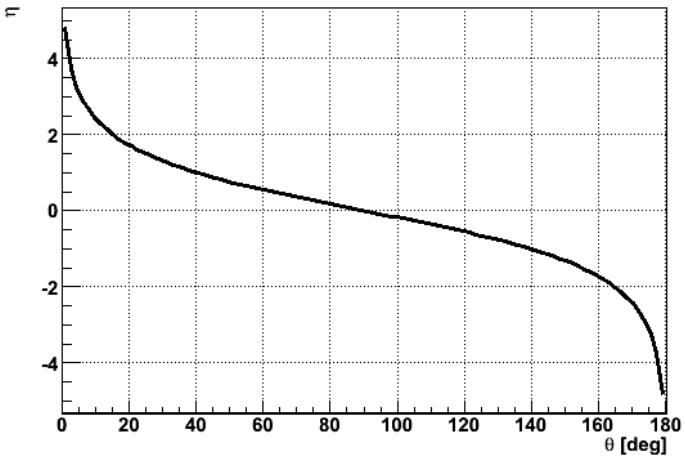

Figure 3.6: Pseudorapidity η as a function of the polar angle θ.

3.2.1 Magnet Systems

The conceptual design of the magnet system was one prime issue of the detector, as all subdetectors had to be planned to function in its environment. Limits of budget and experimental cavern size, combined with the requirement to measure muons, possessing a momentum of 1 GeV, with a precision of 10 %, led to the choice of superconducting technology. The installed system creates a magnetic field over a volume of approximately 12 000 m^3 (defined as the region in which the field exceeds 50 mT). The magnet system consists of one small radius, thin walled solenoid and three air-core toroids. Situated before the barrel ECAL and integrated in its cryostat, optimization of solenoid material was crucial to minimize its impact on the calorimeters performance. A thickness of about 0.66 radiation lengths (X_0) in radial direction was achieved. This limits the the ECAL barrel resolution in the region $1.2 < |\eta| < 1.4$ to some extent. With an inner diameter of 2.4 m and an axial length of 5.8 m the central solenoid does not cover the whole inner detector. This leads to a field non-uniformity at the end of the tracker volume. It provides an axial magnetic field of around 2 T. The three superconducting air-core toroids, one located in the barrel region, the other two in the end-caps, are each build up of eight independent coils. With an axial length of 25.3 m, an inner diameter of 9.4 m and an outer diameter of 20.1 m, weighting 830 tons, the barrel toroid provides a torodial field of approximately 0.5 Tesla for the muon detectors. The end-cap toroids together contribute with approximately 1 Tesla, weighting 239 tons each, span from a diameter of 1.7 m to 10.7 m.

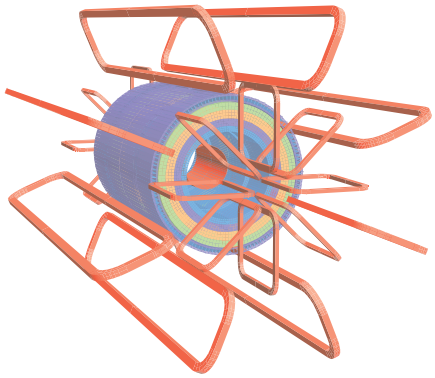

Figure 3.7: Shown is the layout of magnet systems (in red) of the ATLAS detector, with a model of the calorimeter systems magnetic properties (various colors) [43].

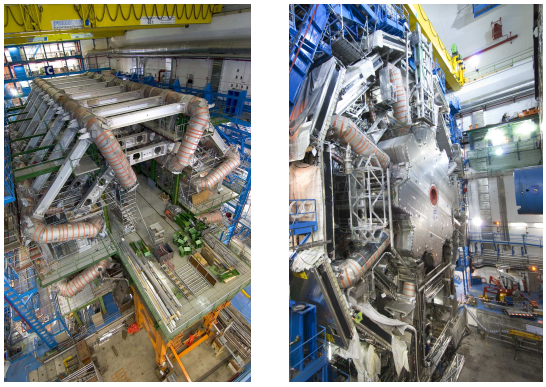

Figure 3.8: The barrel toroid system with support structure (left) and one installed end-cap toroid (right).

The magnetic field was mapped with B-field-sensors, based on the Hall effect. Discrepancies between the modeled and the measured magnetic field usually ranged from $2-5\,\mathrm{mT}$, although some locations showed differences up to $50\,\mathrm{mT}$. Further investigation to improve the model of the magnetic field is in progress, as this is crucial for the precision of the muon spectrometer system. The long term goal was set to drive the discrepancies below $0.2\,\mathrm{mT}$.

3.2.2 Inner Detector

The ATLAS inner detector (ID) was designed to provide momentum measurement, robust and redundant pattern recognition as well as primary and secondary vertex measurement for charged tracks with a p_T above $0.5\,\mathrm{GeV}$ in a pseudorapidity range of $|\eta| < 2.5$. Precise measurements of the second vertex are very important for heavy flavor tagging and identification of hadronically decaying τ-leptons. Additionally it provides a very efficient electron identification for $|\eta| < 2.0$. A very high granularity is needed to separate particles close to the interaction point. The ID consists of three independent supplementary subdetectors, a pixel detector, the silicon microstrip sensors also called SemiConductor Tracker (SCT) and a Transition Radiation Tracker (TRT). They are build close around the beam pipe, which in the region of the ID is manufactured of beryllium. Meeting the physics requirements to provide a robust and stable operation over years was the probably most challenging part of the ID systems design. Withstanding the harsh radiation conditions near the interaction point stood in conflict with the requirement for a low material budget. The material budget of trackers steadily rose over the years, reaching up to $1.2\,\mathrm{X}_0$) at $\eta \approx 1.7$ [44]. By cooling the pixel detector and the SCT to approximately -5 to -10 degrees Celsius, radiation induced doping concentration changes of the silicon pn-diodes will decelerated. The ID, including its envelope, measures $7\,\mathrm{m}$ in length and $1.15\,\mathrm{m}$ in radius.

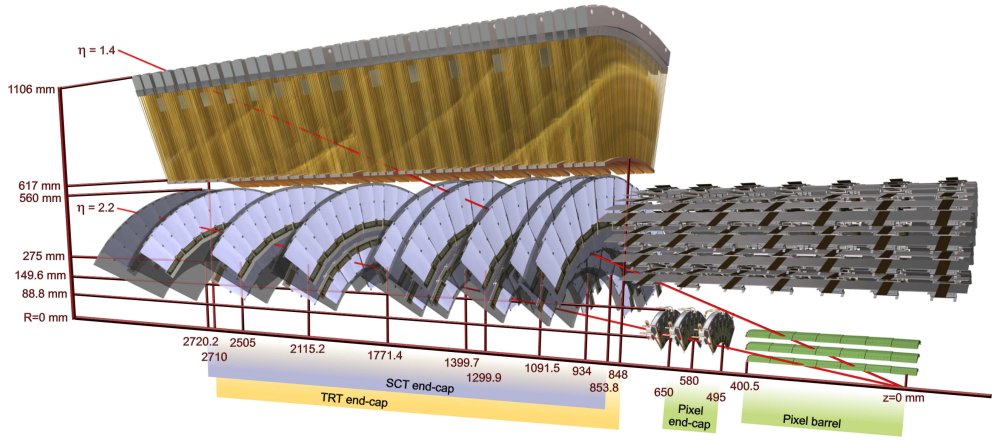

Figure 3.9: Inner detector with red lines indicating charged tracks with $p_T = 10\,\text{GeV}$ of $\eta = 1.4$ and $\eta = 2.2$ transversing the ID. The barrel part of the TRT is not depicted [43].

The pixel detector sensors are 250 μm thick and made of double sided processed, oxygenated n-type wafers. This novel design allows good charge collection efficiency, even after type inversion, invoked by radiation. Highly oxygenated material showed good radiation tolerance to charged hadrons in long term studies. The operation voltage is assumed to rise from initially approximately 150 V to around 600 V after ten years of operation. The pixel detector consists of three layers in the central region situated at the following given radii measured from the IP, 50.5 mm, directly on the beam pipe of the LHC, 88.5 mm and 121.2 mm. Three discs at distances of $z = \pm 495\,\text{mm}$, $z = \pm 580\,\text{mm}$ and $z = \pm 650\,\text{mm}$ cover the higher η-regions. The spacial resolution of the pixel detector is designed to achieve 10 μm in the $R - \phi$ plane and 115 μm in z- in the barrel and R-direction the end-caps.

For reasons of cost and reliability the SCT uses a classical single-sided p-in-n technology with AC-coupled readout strips. The SCT sensors operation voltage will be increased from approximately 150 V to $250 - 300\,\text{V}$ after ten years of use to ensure good charge collection efficiency. Using a small angle (40 mrad) stereo strip technology results in the ability of reconstructing the z-coordinate of a track, by measurement of R and ϕ. This technique allows a separation of two charged tracks, if their interspace, while passing the SCT, is greater then 200 μm. The four double layers of strips in the barrel provide eight measurements per track. Nine discs in each end-cap, consisting of double layer strips, complete the SCT. The spacial arrangement of the layers is depicted in Figure 3.10, axial distances, $|z|$, from the IP are included in Figure 3.9. The designed resolution of the SCT is 17 μm in the $R-\phi$ plane and 580 μm in z- in the barrel and in R-direction in the end-caps.

The basic detector elements of the TRT are polyimide drift tubes, also called straw tubes. They posses a diameter of 4 mm and are filled with a gas mixture of 70 % Xe, 27 % CO_2 and 3 % O_2. Consisting of a multi-layer system, containing Al-, graphite-, and polyimide-layers, they are optimized for good mechanical and electrical properties. The straw resistance is below $300\,\frac{\Omega}{\text{m}}$. A 31 μm diameter very pure and gold plated tungsten wire is the anode of

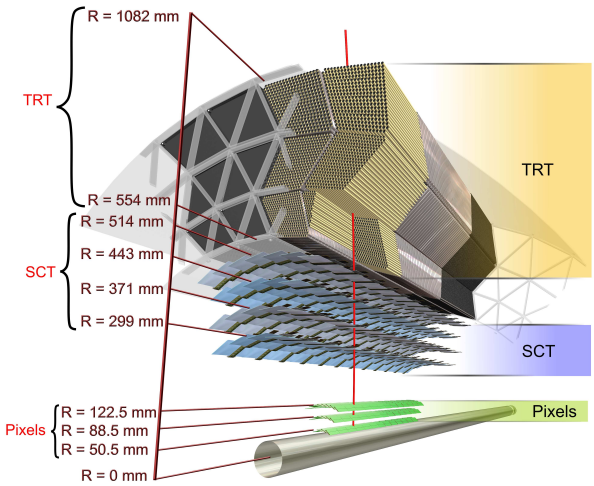

Figure 3.10: Inner detector barrel with its systems in detail, the red line indicating a charged track with $p_T = 10\,\text{GeV}$ and $\eta = 0.3$ [43].

the straw system, it is kept at ground-potential and directly connected to the front-end electronics. Filled with $5-10\,\text{mbar}$ over-pressure of the gas mixture and a cathode nominal operational voltage of $1530\,\text{V}$, the achieved gain is in the order of 2.5×10^4. Charged particles traversing the straws ionize the filling gas and by second ionization a measurable current is created. The special feature of the TRT are the different dielectrical constants of the straw layer structure. This invokes transition radiation especially for electrons, thereby easier identified. Straw bundles of $144\,\text{cm}$ length, arranged in three layers, are placed in the barrel, covering the radial range of $554 - 1082\,\text{mm}$, compare Figure 3.10. The barrel straw anodes are electrically split and mechanically supported in the middle. Each half is read out from the outer end. Radial arranged straws with a length of $37\,\text{cm}$ cover charged tracks up to $\eta = 2.0$. The straws only provide $R-\phi$ -measurement in the barrel and $z-\phi$ -measurement in the end-caps with an intrinsic accuracy of $130\,\mu\text{m}$. The track indicated in Figure 3.10 hits 36 straws, which is close to the estimated average for $\eta \leq 2.0$ of 35 straw hits per charged track. Opposed to pixel detector and SCT the TRT will operate at room temperature.

The required p_T-resolution of the inner detector is $\frac{\sigma(p_T)}{p_T} = (0.05 p_T \oplus 1)\%$ [43]. For particles from the primary vertex with a $p_T > 1\,\text{GeV}$ and $\eta < 2.5$ the track parameter resolutions are given by:

$$\sigma_X(p_T) = \sigma_X(\infty) \left(1 \oplus \frac{p_X}{p_T}\right).$$

The resolution is a function of the particle p_T, with $\oplus$ denoting addition in quadrature. Table 3.1 lists the input values for the formula stated above for two η-regions depending on the parameter of interest.

Track parameter	$0.25 < \|\eta\| < 0.50$		$1.50 < \|\eta\| < 1.75$	
	$\sigma_x(\infty)$	p_x(GeV)	$\sigma_x(\infty)$	p_x(GeV)
Inverse transverse momentum $(\frac{q}{p_t})$	$0.34\,\text{TeV}^{-1}$	44	$0.41\,\text{TeV}^{-1}$	80
Azimuthal angle (ϕ)	$70\,\mu$rad	39	$92\,\mu$rad	49
Polar angle $(\cot\theta)$	0.7×10^{-3}	5.0	1.2×10^{-3}	10
Transverse impact parameter (d_0)	$10\,\mu$m	14	$12\,\mu$m	20
Longitudinal imp. par. $(z_0 \times \sin\theta)$	$91\,\mu$m	2.3	$71\,\mu$m	3.7

Table 3.1: Expected track-parameter resolutions (RMS) shown for the barrel and end-cap region [45].

3.2.3 Calorimeter Systems

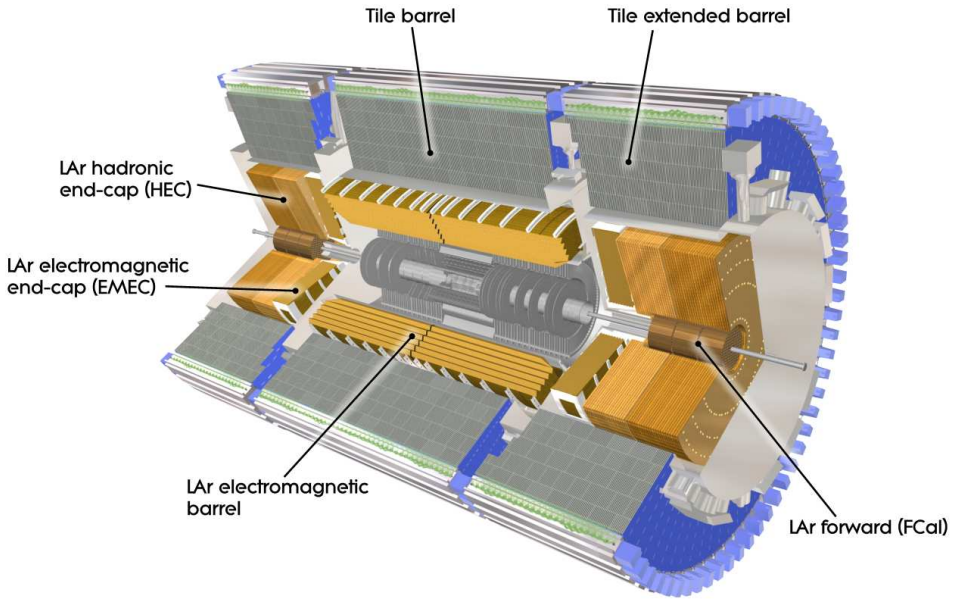

Figure 3.11: Calorimeter systems with labels pointing out the single components[43].

The calorimeter technology and design of the ATLAS detector succeeds the basic working principles of the UA1-detector and the H1-detector at HERA (Hadron Electron Ring Accelerator). From the first it adopted full coverage in total transverse energy. The latter mentioned was the first detector that featured a lead liquid argon (LAr) sampling calorimeter. In contrast to magnetic spectrometer systems the intrinsic resolution of a calorimeter

improves with higher particle energies. The ATLAS calorimeter system consists of an electromagnetic and a hadronic calorimeter. It was constructed to precisely measure energies and positions of electromagnetic, like electrons and photons, and strong interacting particles, the hadrons. The overall layout is depicted in Figure 3.11. It will also contribute to the Level-1 trigger. The hadronic calorimeter reached one of its design goals already: complete coverage of the region $|\eta| < 4.9$. This makes missing energy determination possible, an important indicator for neutrinos or new physics. Both sampling calorimeters posses full ϕ-symmetry and ϕ-coverage, though with different materials and geometries. In the passive absorber material secondary shower particles are initiated by charged particles. Measuring their quantity and thereby the energy deposited is the function of the active detector material. The design ensures enough radiation lengths (X_0) and interaction lengths (λ) in the path of the particle to capture the most the shower initiated by incident particle with energies of up to several TeV. This enables these calorimeters to measure and reconstruct its energy. Several layers, usually three, in longitudinal or η-direction of the calorimeters enhance the shower-pointing accuracy.

Electromagnetic Calorimetry

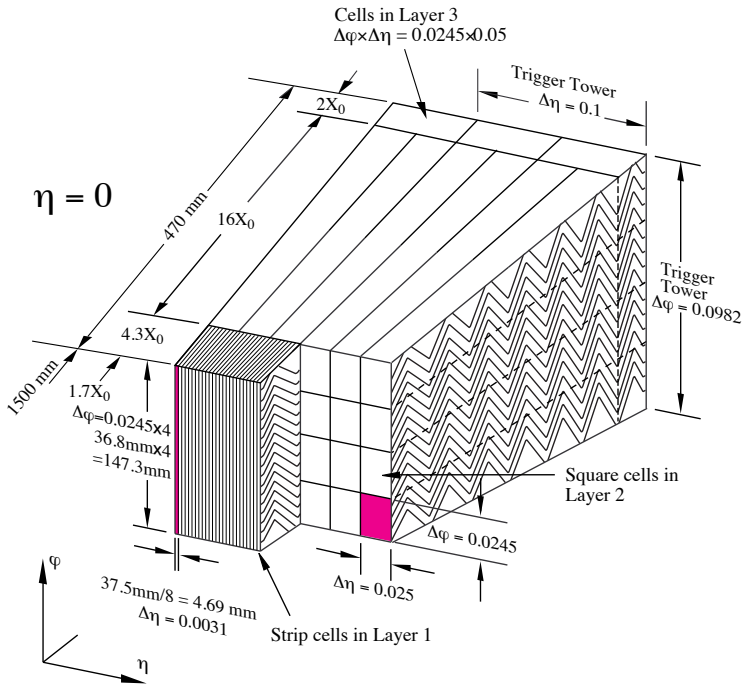

Figure 3.12: Layers, cells and spacial dimensions of the electromagnetic calorimeter at $\eta = 0$, depicting the samplings different granularities [43].

The precision electromagnetic calorimeter system is a lead liquid argon sampling detector. It consists of a barrel (EMB) and two end-cap calorimeters (EMEC). The barrel is

build of two identical halves, each with an axial length of 320 cm, spanning over the radial range from 140 cm to 200 cm. They are divided by a gap of 0.6 cm at $z = 0$ cm. The wheels of the EMECs are 63 cm thick, with inner and outer radii of 33 cm and 209.8 cm, positioned at $|z| = 374.4$ cm. One wheel is mechanically subdivided into two wheels, the outer covering $1.375 < |\eta| < 2.5$ and the inner $2.5 < |\eta| < 3.2$. The gap of 0.3 cm is mostly filled with low density material. The position of the wheels was changed by $|z| = +4$ cm, from the nominal position, yielding inner detector services. This degenerates the designed projectivity of the geometry slightly. An overlap region between the barrel $|\eta| < 1.475$ and the EMEC $1.375 < |\eta| < 3.2$ was designed to avoid cracks. Choosing an accordion geometry for the absorbers and the kapton electrodes of the electromagnetic calorimeters naturally provides a full ϕ-coverage. The folding angles of the accordion waves were optimized, depending on the radius, to keep the LAr gap constant, as can be evinced in Figure 3.12. To limit the decrease of the sampling fraction F_S, as $|\eta|$ increases, the absorber lead plates thickness changes from 1.53 mm for $|\eta| < 0.8$ to 1.13 mm for $|\eta| > 0.8$ in the barrel. In the end-cap calorimeters the plates have a thickness of 1.7 mm for $|\eta| < 2.5$ and 2.2 mm for $|\eta| > 2.5$. To provide mechanical stability these are glued between two 0.2 mm thick stainless-steel sheets. The electrodes are made of three conductive copper layers separated by insulating polyimide sheets, located between the absorber plates.

	granularity $[\Delta\eta \times \Delta\phi]$ versus $\|\eta\|$			
	barrel		end-cap	
Presampler	0.025×0.1	$\|\eta\| < 1.52$	0.025×0.1	$1.5 < \|\eta\| < 1.8$
Layer 1	$0.025/8 \times 0.1$	$\|\eta\| < 1.40$	0.050×0.1	$1.375 < \|\eta\| < 1.425$
	0.025×0.025	$1.40 < \|\eta\| < 1.475$	0.025×0.1	$1.425 < \|\eta\| < 1.5$
			$0.025/8 \times 0.1$	$1.5 < \|\eta\| < 1.8$
			$0.025/6 \times 0.1$	$1.8 < \|\eta\| < 2.0$
			$0.025/4 \times 0.1$	$2.0 < \|\eta\| < 2.4$
			0.025×0.1	$2.4 < \|\eta\| < 2.5$
			0.1×0.1	$2.5 < \|\eta\| < 3.2$
Layer 2	0.025×0.025	$\|\eta\| < 1.40$	0.050×0.025	$1.375 < \|\eta\| < 1.425$
	0.075×0.025	$1.40 < \|\eta\| < 1.475$	0.025×0.025	$1.425 < \|\eta\| < 2.5$
			0.1×0.1	$2.5 < \|\eta\| < 3.2$
Layer 3	0.050×0.025	$\|\eta\| < 1.35$	0.050×0.025	$1.5 < \|\eta\| < 2.5$

Table 3.2: Granularity of the electromagnetic calorimeter depending of the $|\eta|$-region [43]

The η-segmentation was realized by etching patterns on the different layers. Ganging together an appropriate number of electrodes, as shown in Figure 3.12, results in ϕ-separation.

Segments of the ECAL that are read out together are called cells. Granularity of the EMB and EMEC cells in dependence of $|\eta|$ are listed in Table 3.2.

High energy electrons in matter predominately lose their energy by bremsstrahlung [16]. High energetic photons, γ, traversing matter preferably perform electron-positron production. The e^+ and e^- produce bremsstrahlung again, thus an electromagnetic shower is formed. In the electromagnetic calorimeter the charged shower particles ionize the liquid argon. The produced charges travel, due to an electrical field, to the electrodes, where a signal is registered. The nominal voltage applied is given with 2000 V. Muons are so called minimal ionizing particles (MIP) and will hardly leave a trace in the calorimeters. Rare events of δ-rays or knock-on electrons, where the muon transfers momentum to an electron from the detector material, constitute an exception.

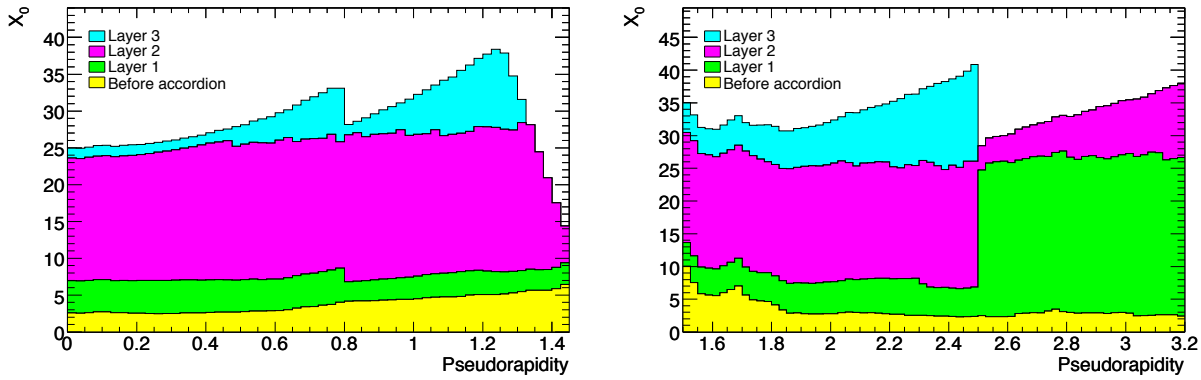

Figure 3.13: Cumulative material before and of the electromagnetic calorimeter in X_0, showing the different layers color coded for the barrel (left) and the end-caps (right) [43].

An additional separate layer, the presampler, consisting of single active layer of liquid argon with a thickness of 11 mm for the barrel up to $|\eta| = 1.52$ and 2 mm for the EMEC $1.5 < |\eta| < 1.8$, was installed. Main reason for this coarsely granulated layer is the large amount of material accumulated in front of the electromagnetic calorimeter. In the region $|\eta| < 1.8$ it reaches several radiation lengths X_0, as can be seen in Figure 3.13. X_0 is defined as both, the mean distance over which a high energy electron loses energy to $\frac{1}{e}$ of its initial value by bremsstrahlung and for a high energetic photon it is $\frac{7}{9}$ of the mean free path for pair production, usually measured in $\frac{g}{cm^2}$ or cm. An electromagnetic shower may therefore begin before reaching the calorimeter. Corrections for upstream energy losses, using the presampler information, will improve the energy reconstruction quality.

The region of $|\eta| < 2.5$ is also called the precision-measurement-region, as the granularity is very fine and the longitudinal direction is covered by at least three sampling layers. Energy resolution is degenerated in the overlap region $1.375 \lesssim |\eta| \lesssim 1.5$, as the cells are coarser and only two samplings per calorimeter are provided, as listed in Table 3.2. Sometimes this region, due to its worse energy resolution is referred to as crack-region. In the inner wheel $2.5 < |\eta| < 3.2$ the ECAL is equipped with only two layers in η-direction.

The granularity of the cells in the first or strip layer is finely segmented in η, thus optimized for electron and jet separation. By providing an equal fine granularity in ϕ and η the second layer allows electron and photon shower positions and directions to be determinated. It is the base for the separation of photons from the IP and π^0-decay photons. With its depth of approximately $16\,X_0$ this layer is designed to absorb the largest part of the electromagnetic showers induced by electromagnetic interacting particles with energies up to several TeV. The coarser third sampling allows rejection of early beginning hadron shower, which will occur at low rates and punch through to the hadronic calorimeter.

The calibration of the ECAL in situ, which will provide the final relative and absolute calibration constants, is an important issue. The ATLAS ECAL, due to its layout and construction is uniform to a level below 0.5 %, when considering areas of $0.2\,\Delta\eta \times 0.4\,\Delta\phi$. This was shown in test beam results [46, 47]. 384 sectors will have to be calibrated for a region of $|\eta| < 2.4$. Using the Z^0-mass constrain with $Z^0 \rightarrow ee$ events, without reference to the ID, the goal is to reach an intercalibration of better than 0.5 % [45]. A second goal, which can be achieved using the same events is the determination of the absolute electromagnetic energy scale to an accuracy in the order of 0.1 %. The greatest challenge will be to detect and correct for additional inner detector material.

A required energy resolution of $\frac{\sigma_E}{E} = \left(\frac{10}{\sqrt{E}} \oplus 0.7\right)$ % is given by [43]. The fractional energy resolution of the electromagnetic calorimeter is conventionally parametrized as

$$\frac{\sigma_E}{E} = \frac{a}{E} \oplus \frac{b}{\sqrt{E}} \oplus c.$$

Where a is the noise term, b the sampling term and c is the constant term. Cluster corrections can help to reduce c from 0.65 % to 0.43 %, this is stated in [45] as an example for a photon at $|\eta| = 0.3$. The expected performance is nearly similar for photons and electrons. For higher $|\eta|$-values the energy resolution degenerates faster for electrons than photons, this is due to the impact of the larger amount of accumulated material in front of the calorimeter in this region. The sampling term is anticipated to be (10.17 ± 0.33) % for the barrel and (14.5 ± 1.0) % in the end-cap region [45].

Test beam measurements were carried out at the SPS H8 and H6 beam lines. The test beam data of a barrel module fitted after the noise was subtracted is depicted in Figure 3.14, which also states figures for b and c [43].

Hadronic Calorimetry

This part of the calorimetry system uses two different techniques. The barrel covering $|\eta| < 1.0$ and extended barrel tile, covering $0.8 < |\eta| < 1.7$ consist of scintillating plastic tiles and steel plates. The second component is the hadronic end-cap (HEC) located in the wheels, covering $1.5 < |\eta| < 3.2$. It uses a copper-liquid argon technique similar to the lead-LAr of the EMEC. The cryostats are therefore shared by EMEC, HEC and forward calorimeters (FCals), as shown in Figure 3.17. Latter cover $3.1 < |\eta| < 4.9$ and also use the LAr technology. With a radial range from 2.28 m to 4.25 m the barrel and extended

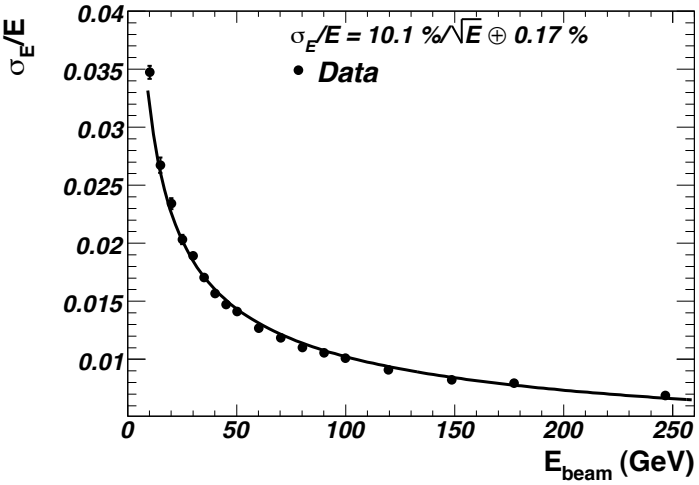

Figure 3.14: Fractional energy resolution of the electromagnetic barrel calorimeter at $|\eta| = 0.687$ depicted as a function of the test beam energy [43].

tile provide approximately $7.4\,\lambda$ in this direction. λ, the (nuclear) interaction length, is defined as the mean free distance a relativistic particle passes through matter, before its energy decreases to $\frac{1}{e}$ of the initial value, usually measured in $\frac{\mathrm{g}}{\mathrm{cm}^2}$, for a given material in cm. The cumulative amount of the ATLAS detector material in units of λ as a function of the pseudorapidity is provided in Figure 3.18.

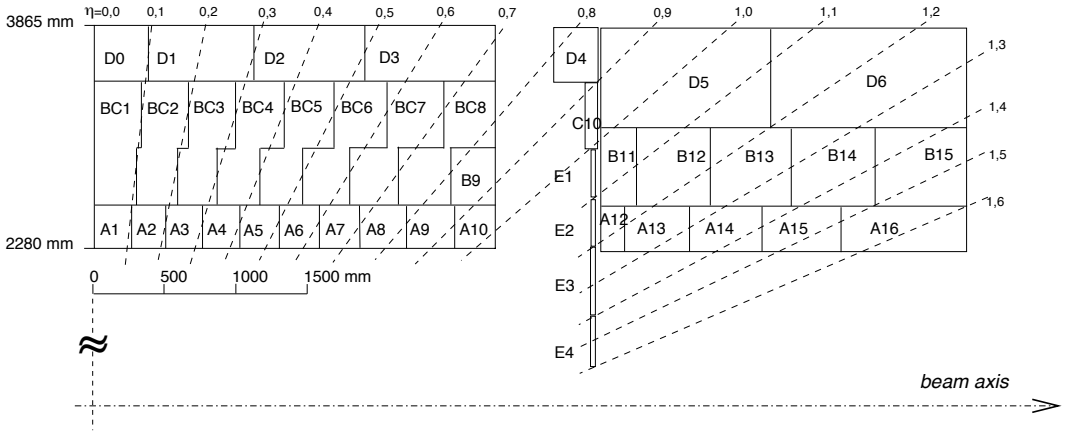

Figure 3.15: Segmentation of the hadronic tile calorimeter in η and depth, the central barrel (left) and the extended barrel (right) [43].

Fundamental elements of the sampling tile calorimeters are scintillating plastic tiles and steel plates. Tiles provided in eleven sizes, all 3 mm thick, with radial lengths ranging from 97 mm to 187 mm and azimuthal lengths from 200 mm to 400 mm, are the active detector material. Steel plates used as the passive absorber material are thicker, so an approximate volume ratio of 4.7 : 1 is achieved. A schematic view of this stacking structure is given in

Figure 3.16. Ionizing secondary shower particles produce ultraviolet scintillation light in the polystyrene. Each tile is read out by two flour doped wavelength shifting fibres. By grouping and coupling of the fibres a three dimensional cell structure is created, depicted in Figure 3.15. The visible light of the fibre bunches creates an electrical signal in the photo-multipliers (PMTs), which is read out. Three radial samplings with approximately 1.5 λ, 4.1 λ and 1.8 λ at $|\eta| = 0$, have a granularity in $\Delta\eta \times \Delta\phi$ of 0.1×0.1 for the first two and 0.2×0.1 for the third layer. Long term irradiation tests of tile-fibre-systems indicate, that a light loss of less then 10 % is expected after a ten year operation period of the LHC. The tile calorimeters are equipped with three calibration systems, namely a charge injection, a laser and a ^{137}Cs radioactive source. These test optical as well as digitized signals and help to set the PMT gains to an uniformity of ± 3 %.

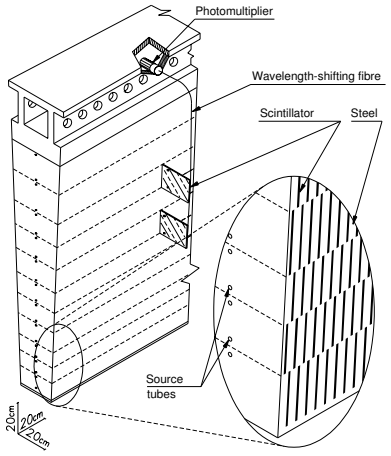

Figure 3.16: Schematic view of a hadronic calorimeter module including the read out components [43].

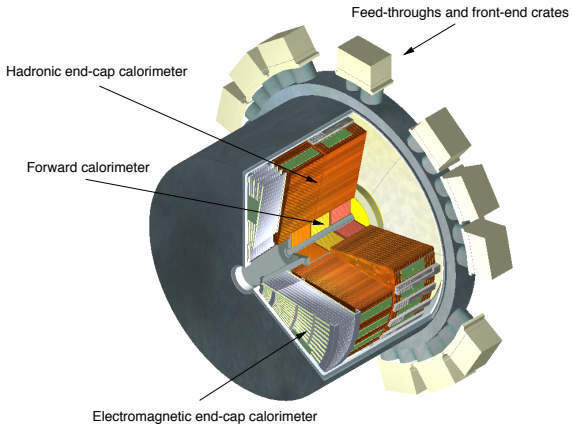

Figure 3.17: Cut-away view of the three end-cap calorimeters situated in the end-cap cryostat extending 3.17 m in length and an outer radius of 2.25 m [43].

The HEC is situated behind the EMEC, as Figure 3.17 shows. It consists of two wheels, HEC1, the front wheel, and HEC2, rear wheel and provides four longitudinal layers. Modules of the HEC are build of copper plates. HEC1 begins with a 12.5 mm thick front plate, followed by 24 discs of 25 mm. HEC2 provides a coarser sampling fraction with 16 plates each 50 mm thick plus a 25 mm front plate. Corresponding thicknesses in interaction lengths along the η-axis of the HEC are depicted in Figure 3.18, here HEC0 indicates the first sampling of HEC1. The inner radius changes from 372 mm for the first nine plates of HEC1 to 475 mm for the following HEC plates. Gaps filled with liquid argon, the active material, are kept constant at 8.5 mm in the whole HEC. Cell structure, created by etching a pattern on the central foil in each gap, provides a semi-pointing geometry with cell sizes of 0.1×0.1 for $|\eta| < 2.5$ and 0.2×0.2, in $\Delta\eta \times \Delta\phi$ for higher $|\eta|$-values.

The FCals, which cover the highest $|\eta|$-regions are exposed to high particle fluxes. They

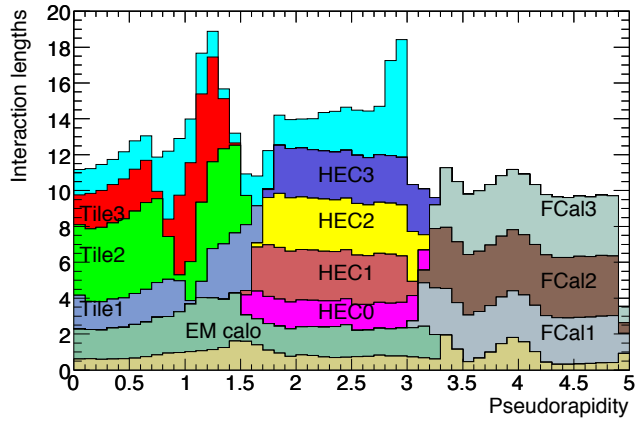

Figure 3.18: Cumulative amount of material measured in λ, also showing the material before the first layer of the muon spectrometer in lighter blue up to $|\eta| = 3.0$ [43].

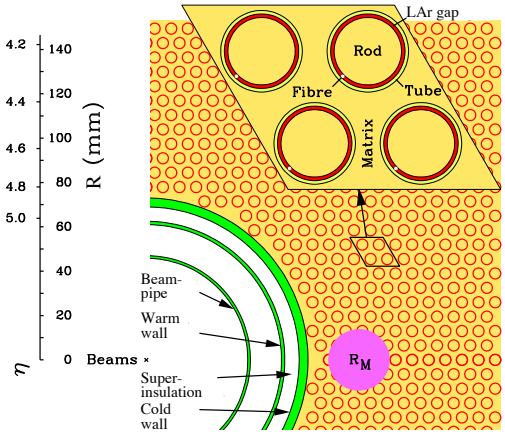

Figure 3.19: Schematic of the FCal electrode structure, with the Molière radius R_M represented by a solid disc [43].

are located at a distance of approximately 4.7 m from the interaction point. This resulted in a design of very small liquid argon gaps, smaller than the usual 2.1 mm of the barrel. The FCal is divided into three 45 cm deep modules. This adds up to a total depth of 9.94 λ or 208.1 X_0. Electrodes are small diameter rods running in a matrix of high precision drilled holes parallel to the beam line. A radiation hard plastic fibre wound around the rod provides the LAr gap. A detailed view of FCal1 and the electrode structure is given in Figure 3.19. The first partition, FCal1, is made of copper plates. This material improves heat removal and optimizes resolution for electromagnetic interacting particles. The LAr gap width of 0.269 mm, with 27.6 X_0 depths, is designed to absorb electromagnetic showers. For FCal2 and FCal3 tungsten was used as the base material. This minimizes the lateral spread of hadronic showers and with absorption lengths of 3.68 λ and 3.60 λ is designed to provide full containment. The LAr gap sizes are designed wider the further the distance from the interaction point, 0.376 mm for FCal2 and 0.508 mm for FCal3. Higher readout currents and thereby better energy measurement resolutions are achieved by this. A plug made of copper alloy was mounted behind the FCal3, as a shield against background radiation. Resolutions required from the hadronic calorimeters are given by [43] as follows:

$$\frac{\sigma_E}{E} = \left(\frac{50}{\sqrt{E}} \oplus 3\right)\% \quad \text{for} \quad |\eta| < 3.2$$

$$\frac{\sigma_E}{E} = \left(\frac{100}{\sqrt{E}} \oplus 10\right)\% \quad \text{for} \quad 3.1 < |\eta| < 4.9.$$

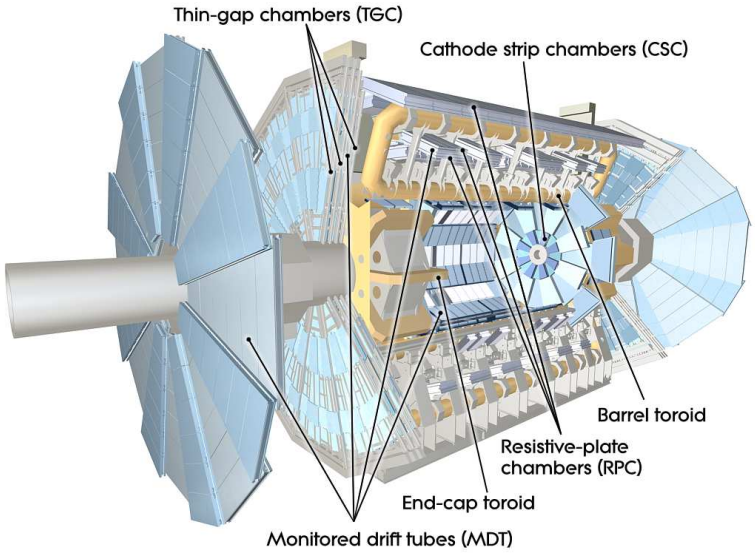

Figure 3.20: Muon spectrometer with its four chamber subsystems [43].

3.2.4 Muon Spectrometer

The ATLAS muon system was designed to achieve a transverse momentum, p_T-, resolution for 1 $\frac{\text{TeV}}{\text{c}}$ tracks in stand-alone mode of approximately 10 %. Considering the magnetic field and geometrical setup of the spectrometer, this translates into a sagitta along the z- (or beam-) axis of about 500 μm, with a resolution below 50 μm. The lower boundary for muon detectability is given with a muon momentum of approximately $3 - 4\,\frac{\text{GeV}}{\text{c}}$. On average, energy of this order is lost by muons in the detector material between IP and the muon systems. Resistive Plate Chambers (RPC), well-proven in the L3@LEP and BaBar experiments, situated in the barrel part $|\eta| < 1.05$. Thin Gap Chambers (TGC), a technology also used by the OPAL (Omni-Purpose Apparatus at LEP) experiment also at LEP, in the end-cap $1.05 < |\eta| < 2.4$, both additionally provide Level-1 trigger signals. To achieve the design resolution, a strict alignment requirement of $\pm 30\,\mu$m was set. An optical system of around 5000 sensors was set up to permanently control the placement of the muon system components. This allows potential offline data corrections, in case of in situ displacements. Further, around 1700 three-dimensional Hall probes are arranged on the chambers providing precise information about position and shape of the conductors of each coil. It will be used to determinate the magnetic field with high accuracy throughout the whole volume, a necessity for high precision muon measurement. In the region of $|\eta| < 1.0$ the barrel toroid and for the region $1.4 < |\eta| < 2.7$ the end-cap toroids provide the magnetic field. In the so called intermediate region $1.0 < |\eta| < 1.4$, where these fields overlap, modeling calculations are nontrivial. Partial reduction of the bending power occurs in this region. Detectors placed in concentric cylindrical shells around the barrel at radii of 5 m, 7.5 m and 10 m. Large wheels containing in the end-cap spectrometer systems are placed at distances

of $|z| \approx 7.4\,\text{m}$, $10.8\,\text{m}$, $14\,\text{m}$ and $21.5\,\text{m}$. Varying gaps in ϕ at $|\eta| \approx 0$, with sizes of up to $2\,\text{m}$, were left open for services of the inner detector, solenoid and calorimeters.

Highest precision momentum measurement is achieved by the Monitored Drift Tube cham-

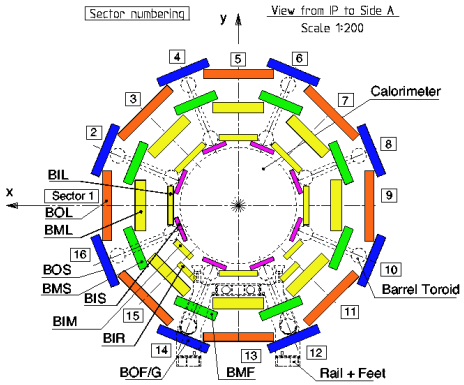

Figure 3.21: Barrel muon system cross section, perpendicular to the beam axis or non bending plane, the outer diameter measures about 20 m [43].

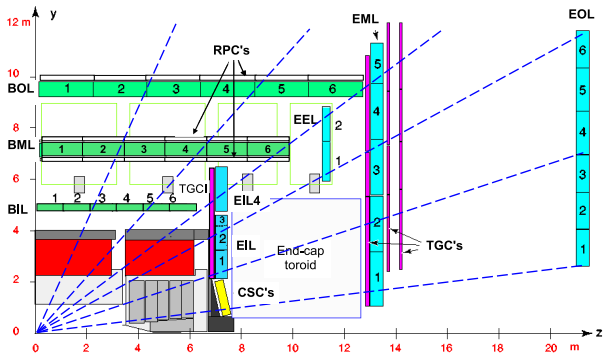

Figure 3.22: Cross section of the muon system in the bending plane, with dashed lines representing muons, demonstrating, that typically three systems are transversed [43].

bers (MDTs), covering the whole muon spectrometers η-range. They combine simplicity of construction and predictability of mechanical deformations. An average resolution of $80\,\mu\text{m}$ per tube or about $35\,\mu\text{m}$ per chamber, each containing three to eight layers of MDTs, is achieved. In the innermost layer of the end-cap Cathode-Strip Chambers (CSCs) instead of MDTs were installed, due to their higher rate capacity and better time resolution. CSCs are multiwire proportional chambers, with cathode plates segmented into orthogonal strips, allowing a measurement of both coordinates. They have a resolution of $40\,\mu\text{m}$ in the bending plane (η) and 5 mm in the transverse plane (ϕ). To tag a special beam crossing a system has to provide signals in a spread below 25 ns. The technology of the RPCs and TGCs delivers signals even below this spread, while measuring coordinates of the track in η and ϕ. As the MDTs are designed to perform as precision trackers for the η coordinate only. This measurement is then matched with trigger detector hits. In case of a successful match the non-bending plane coordinate of the trigger is adopted as the second coordinate for the MDT. Table 3.3 lists further details about resolutions and readout times of subsystems used in the muon spectrometer. A p_T-resolution stated by [43] of $\frac{\sigma_{p_T}}{p_T} = 10\,\%$ for muons with a $p_T = 1\,\text{TeV}$ is required from the spectrometer.

Type	Function	Chamber resolution (RMS) in			Measurements/track	
		z/R	ϕ	time	barrel	end-cap
MDT	tracking	35 μm (z)	–	–	20	20
CSC	tracking	40 μm (R)	5 mm	7 ns	–	4
RPC	trigger	10 mm (z)	10 mm	1.5 ns	6	–
TGC	trigger	2-6 mm (R)	3-7 mm	4 ns	–	9

Table 3.3: Spacial and intrinsic time resolutions of the muon detector sub-systems, not including chamber alignment uncertainties [43]

3.2.5 Forward Detectors

Three smaller detector systems, depicted in Figure 3.23, dedicated to the coverage of the very forward region are installed in addition to the main ATLAS detector systems. They are named LUCID (LUminosity measurement using Cerenkov Integrating Detector), positioned at ±17 m from the IP, near the TAS (Target Absorber Secondaries), Zero-Degree Calorimeter (ZDC), embedded in the TAN (Target Absorber Neutral) at a distance ±140 m and ALFA (Absolute Luminosity For ATLAS) situated at ≈ ±220 m.

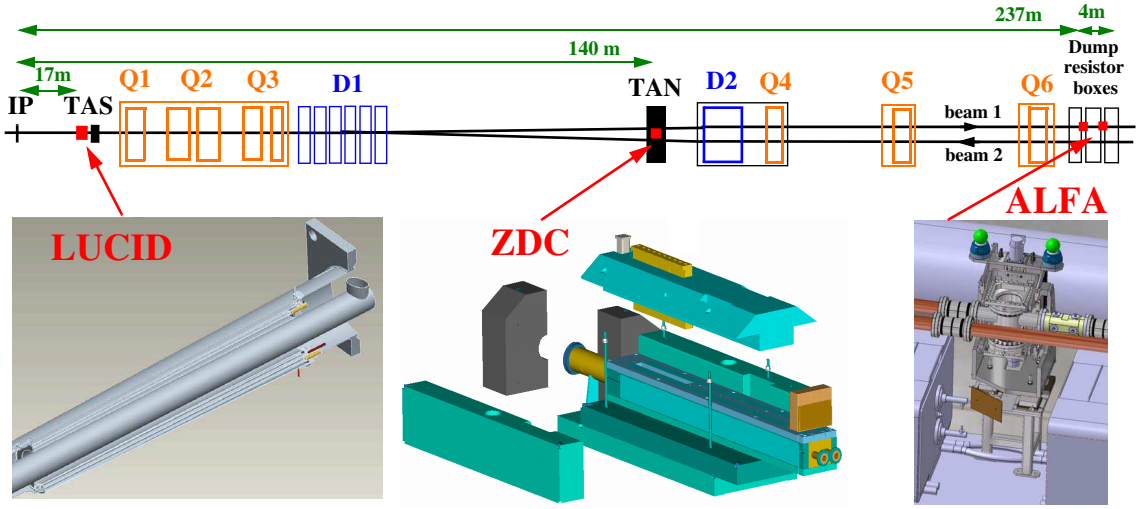

Figure 3.23: Placement of the forward detectors along the beam line, with the distances measured from the ATLAS IP [43].

LUCID is the main relative luminosity monitor for ATLAS. Detecting inelastic $p-p$ scattering it is dedicated to online luminosity monitoring. A use as a rapidity-gap veto trigger for ATLAS is conceivable. LUCID is based on the principle that the number of interactions in a bunch-crossing is proportional to the number of particles detected in the forward region covered by it. The concept of a luminosity detector build of an array of Cerenkov cones was developed by the CDF collaboration. For a first absolute

calibration during the initial period of LHC operation calculations based on LHC machine parameters will be used. Physics processes as $W^{\pm}$- and Z^0-counting and exclusive muon pair production via two-photon interactions can also be exploited. The best calibration source however will be the input from the ALFA measurements. So far only a reduced system was approved which will have to demonstrate its efficiency at luminosities of up to a few $10^{33}\,\frac{1}{\mathrm{cm^2 s}}$. After standing this test upgrades enabling it to function at LHCs design luminosity might be granted.

ZDC are located between the beam-pipes just after they split. Primarily they are designed and build to detect forward neutrons with $|\eta| > 8.3$ from heavy ion collisions. The neutron number in this very forward region is strongly correlated to the centrality of the collisions. Background neutrons, beam-gas and -halo effects are reduced by a coincidence trigger, requiring a signal from both ZDCs. One detector consists of four modules, one electromagnetic with about $29\,\mathrm{X_0}$ and three hadronic calorimeters, each with a depth of about $1.16\,\lambda$. Its time resolution of roughly 100 ps provides an, ID-independent, measurement of the vertex location with a precision of ± 3 cm along the beam axis.

ALFA follows the traditional approach, for hadron colliders, to measure the absolute luminosity via elastic scattering at small angles. Its detectors consist of scintillating-fibre trackers located inside Roman-pots. This technique, successfully used in the past, is based upon separation of the detector volume, called the pot, from the accelerators vacuum with a thin window. An interconnection with bellows to the beam-pipe made a proximity of the detector to the beam of 1 mm possible. The connection of the elastic-scattering amplitude in forward direction to the total cross-section by the optical theorem allows an extraction of the luminosity. Measurements of extremely small scattering angles, around $3\,\mu$rad, translate to a resolution requirement of $30\,\mu$m. As this is smaller than the nominal beam divergence, remoteness from the IP and vicinity to the beam are necessary. Two Roman-pot stations within 4 m are placed on each side at a distance of 240 m from the IP. The anticipated spatial resolution of ALFA is $(25 \pm 3)\,\mu$m.

Future upgrade plans consider additional proton-tagging detectors at distances of ± 420 m and new radiation hard detectors at ± 220 m.

3.2.6 Trigger and Data Acquisition

The trigger system plays an essential role in the Large Hadron Collider experiments, as the collision and data rates are significantly higher than the rates at which they can be stored. Each event produces $\approx 1 - 2\,\mathrm{MB}$ of zero suppressed data. A beam-crossing, occurring with a frequency of 40.08 MHz, on average results in 23 inelastic proton-proton collisions. This would lead to an approximate rate of $132\,\frac{\mathrm{TB}}{\mathrm{s}}$ data produced by the ATLAS detector. Currently installed systems for archival storage and data processing posses a capability corresponding to rates of $300 - 600\,\frac{\mathrm{MB}}{\mathrm{s}}$ [43]. The necessary rejection power in the order of 10^7 cannot be achieved by a single processing step. Large general purpose experiments currently use at least two entities for event selection. At ATLAS the trigger system consists of three levels of event selection, known as Level-1 (L1), Level-2 (L2) and event filter. L2

and the event filter together form the High-Level Trigger (HLT). Data of an event passing these filters is transferred to the data acquisition system (DAQ). An overview of the data flow is given in Figure 3.24.

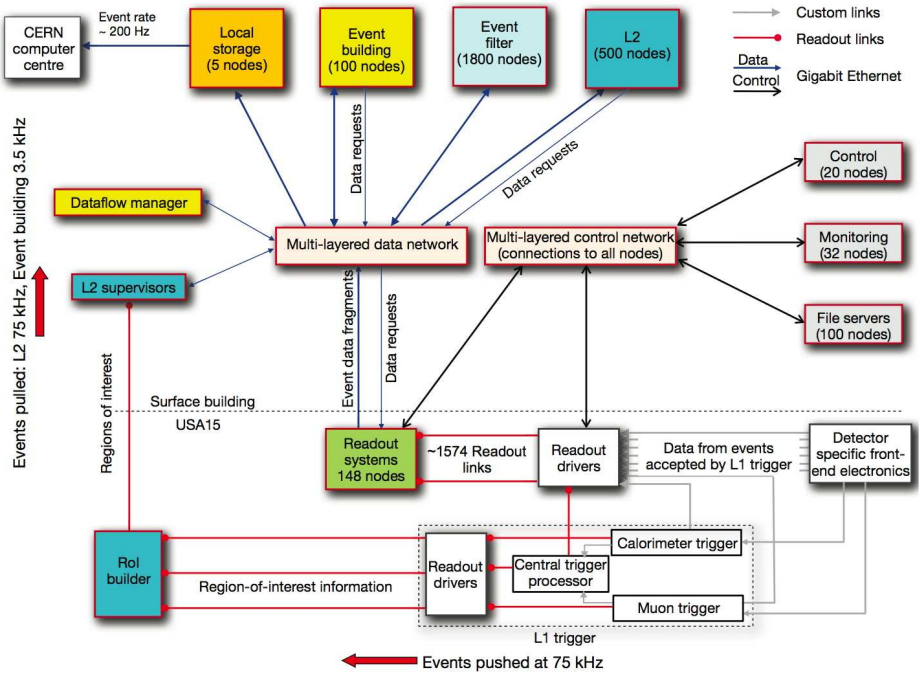

Figure 3.24: Block diagram depicting the interactions, connections, hardware and data-flow of the trigger and data acquisition systems [43].

The L1 trigger uses reduced granularity information from the muon spectrometers RPC and TGC, as well as all calorimeter subsystems. It searches for signatures of high-p_T muons, electrons/photons, jets, hadronically decaying τ-leptons, large total and large missing transverse energy ($E_{T,miss}$). Detector readout systems, especially a system called pipeline memories, require a L1 decision within 2.5 μs after the bunch-crossing occurred. Subtraction of the cable-propagation delays, results in an actual required L1 processing time of less then 1.5 μs. Commercially available computers and networking hardware, as almost entirely used for the HLT, could not meet these needs, therefore the L1 trigger was assembled from custom made electronics. The L1 consists of three major components. L1Calo, a pipelined digital system, works with about 7000 analogue trigger towers, with a granularity of 0.1×0.1 in $\Delta\eta \times \Delta\phi$, larger at higher $|\eta|$-values. It is located in a nearby service cavern, called USA15. Further details of this triggers architecture are depicted in Figure 3.26. The L1 muon trigger combines information of three triggers, one covering the barrel and two for the end-cap regions. Each trigger requires coincidence of hits in different trigger detector stations, which have to be reconstructable, within a certain road,

to the IP. The Central Trigger Processor (CTP) receives the signals from L1Calo and L1 muon, using look-up tables it creates trigger conditions from the input, compare Figure 3.25. While the decision is processed by the trigger all detector readout channel are stored in pipeline memories, placed on and around the detector. The muons time of flight to the spectrometer exceeds a bunch-crossing interval. The typical width of a calorimeter signal extends over four bunch-crossings. These effects are also accounted for. Vicinity to the detector, where radiation levels are high and therefore threaten data reliability, as well as the financial aspect led to the shortest feasible pipeline length. Regions-of-Interest (RoI's), identified as possible trigger sources by the CTP, are passed on to the L2 with a maximal rate of 75 kHz.

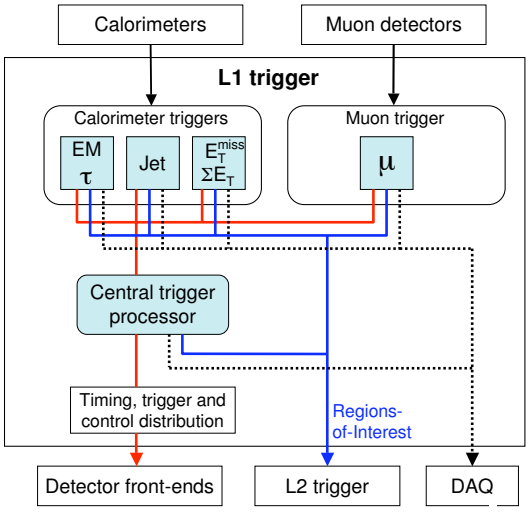

Figure 3.25: Block diagram of the L1 trigger with the data flow direction from left to right [43].

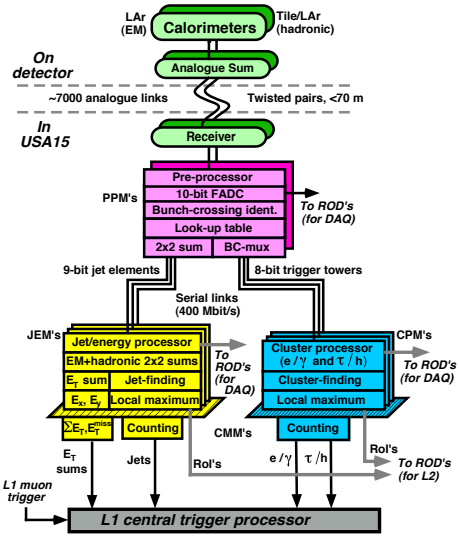

Figure 3.26: Architecture of the L1 calorimeter trigger listing the tasks performed by the three algorithmic processors [43].

The L2 trigger uses the RoI information to limit the amount of data transferred from the detector readout. In several refining steps, each using data from additional detector subsystems, a hypothesis algorithm determines whether identified features meet the selection criteria. The L2 will reduce the event rate below 3.5 kHz within an average processing time of less than 10 ms per event.

The event filter, a processing farm, runs tasks based upon standard ATLAS event reconstruction software. Event selection similar to L2 is repeated with full data access. A subset of tags, created during this decision process, is appended to the event data structure. Average processing times per event of around 1 s are estimated. An other important part of this step is the classification of events according to ATLAS physics streams: electrons, muons, jets, photons, E_T^{miss}, τ-leptons and B-physics. Event data passing this last filter, with an anticipated average rate of 200 Hz, is transmitted to the event-filter output nodes (SFO). Commercially available computer systems were planned and are used for the

HLT. Processing times for these steps reduced to one fourth of the in the Technical Design Report (TDR) anticipated values [48]. Accounting for this performance boost is the use of quad-core instead of single-core processors, as originally designed.

SFO, the interface between HLT and CERN's central data recording service, features an output bandwidth able to handle peak event rate values up to 400 Hz. In case of prolonged transmission failure its capacity allows storage of full event data of about 24 h. In addition to the above mentioned data streams a subset of events is written to calibration streams and an express stream. Selected are only events which fulfill special criteria, marking them as useful for data quality or detector status monitoring.

All triggers discussed above are configurable. Weights of tags may be edited to prefer or defer chosen signatures.

4 Electromagnetic Shower Parametrization

Charged particles loose energy when traversing matter. The higher the energy of the particle bremsstrahlung dominates as source of energy loss. In this process a real photon is emitted in the Coulomb field of a nucleus. High energetic photons can only produce an electron-positron pair in the presence of a nucleus or electrons Coulomb field. Thereby a particle cascade called electromagnetic shower is initiated. In the following an overview of energy loss processes for electrons and photons is given and the parametrization of electromagnetic showers based on P. Grindhammer and S. Peters Ansatz is introduced [49].

4.1 Energy Loss of Electrons and Positrons

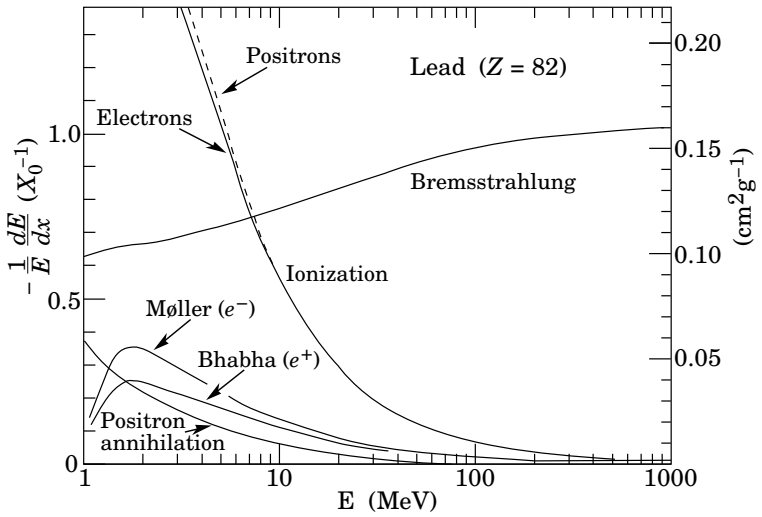

Figure 4.1: Fractional energy loss of electrons and positrons per X_0 in lead ($X_0 = 6.37\,\frac{g}{cm^2}$ was used) as a function of the particles energy [16].

4.1.1 Ionization

Electrons and positrons with energies above 10 MeV interact almost identically with matter, as shown in Figure 4.1. Differences are due to Møller- and Bhabha-scattering, as well

as positron annihilation which occur with significant rates only below this energy. With a low contribution to the overall energy loss they will be neglected in the following.

Ionization for electrons and positrons is defined as scattering at atomic electrons with an energy transfer smaller than 0.255 MeV per collision. The mean rate of energy loss $-\frac{dE}{dx}$ for moderately relativistic charged ions is given by the Bethe-Bloch formula [16, 50, 51]. For electrons their indistinguishability and their significantly lower mass has to be taken into account. This yields the Bethe formula [52, 53, 54]:

$$-\frac{dE}{x} = \frac{2\pi N Z e^4}{m_e v^2}\left[\ln\left(\frac{(\gamma+1)E^2}{2I^2}\right) - \left(\frac{2}{\gamma} - \frac{1}{\gamma^2}\right)\ln(2) + \frac{1}{\gamma^2} + \frac{1}{8}\left(1-\frac{1}{\gamma}\right)^2 - \delta\right] \quad (4.1)$$

with

$$\gamma = \frac{1}{\sqrt{1-\left(\frac{v}{c}\right)^2}}, \quad (4.2)$$

N the density of atoms, I the material mean excitation energy, Z the atomic number of the absorber, m_e the electron rest mass, v the electron velocity and δ the correction term for the density effect [55]. The original Formula 4.1, with $\delta = 0$ is valid from a few keV up to approximately 1 MeV. The lower bound is given by not taking into account atomic binding energies. For lead it rises to the order of 100 keV. At around 1 MeV the density effect reaches a minimum. Above the effects contribution rises logarithmic with the electrons energy and is parametrized by $\delta(E, I, \rho)$, with ρ the density of the material. This paramertization was introduced by Swann [56] and Fermi [57] as an extension of the Bethe equation.

4.1.2 Bremsstrahlung

Charged particles decelerated in the Coulomb field of a nucleus emit a part of their energy in form of a real photon. The term bremsstrahlung contains all radiation caused by acceleration of a charged particle. It even includes synchrotron radiation, produced by charged particles being accelerated for example in a magnetic field. Internal bremsstrahlung describes the radiation of non-virtual quanta, for example photons or gluons, by particles in an interaction. External bremsstrahlung is the exact term for radiation produced when moving through a field of atomic nuclei. As depicted in Figure 4.1 for electrons traversing lead with an energy above 100 MeV, it is the major contribution to the total energy loss. For high energetic electrons the energy lost by bremsstrahlung can be described by:

$$-\frac{dE}{dx} = \frac{4\alpha r_e^2 N_A Z^2}{A}\ln\left(\frac{183}{Z^{\frac{1}{3}}}\right)\cdot E, \quad (4.3)$$

with r_e the classical electron radius:

$$r_e = \frac{e^2}{4\pi\epsilon_0 m_e c^2}, \tag{4.4}$$

α the fine-structure constant, N_A the Avogadro constant and A the atomic weight of the traversed matter. With X_0 the radiation length defined as:

$$\mathrm{X}_0 = \frac{A}{4\alpha r_e^2 N_A Z^2 \ln\left(\frac{183}{Z^{\frac{1}{3}}}\right)} \tag{4.5}$$

Equation 4.3 can be rewritten as:

$$-\frac{dE}{E} = \frac{E}{\mathrm{X}_0}. \tag{4.6}$$

An appropriate scale for high energy particle cascades is provided by X_0, therefore t is defined as the longitudinal coordinate x scaled with the radiation length:

$$t := \frac{x}{\mathrm{X}_0}. \tag{4.7}$$

X_0 is commonly defined as the mean distance after which a high energetic electron looses all but $\frac{1}{e}$ of its initial energy E_0. Therefore one may follow from Equation 4.6 that:

$$E(t) = E_0 \mathrm{e}^{-t}. \tag{4.8}$$

A good approximation of X_0 in $\frac{\mathrm{g}}{\mathrm{cm}^2}$ for $Z > 2$ is:

$$\mathrm{X}_0 = \frac{716.4A}{Z(Z+1)\ln\left(\frac{287}{\sqrt{Z}}\right)}, \tag{4.9}$$

which, as stated by [16], agrees better than 2.5 % with the tabulated values. To express X_0 in cm, it has to be divided by the density ρ in $\frac{\mathrm{g}}{\mathrm{cm}^3}$ of the traversed material.
E_c, the critical energy of an electron, is sometimes defined as the energy value at which the loss rates of ionization and bremsstrahlung are equal. In Figure 4.1 this is the crossing point of the ionization and bremsstrahlung curves. An approximation for E_c in MeV for solids and liquids can be given by [16]:

$$E_c = \frac{610}{Z + 1.24}. \tag{4.10}$$

B. Rossi defines E_c as the energy at which the ionization loss per X_0 is equal to the electron energy. With the approximation [58]:

$$\left|\frac{dE}{dx}\right|_{brems} \approx \frac{E}{\mathrm{X}_0} \tag{4.11}$$

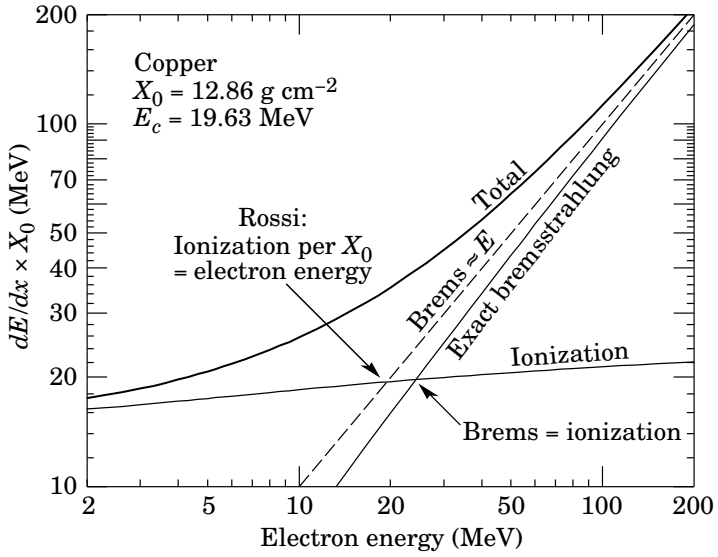

Figure 4.2: Two definitions of the critical energy E_c depicted for copper [16].

this is equivalent to the first definition. However Rossis form of E_c was found to describe the transverse electromagnetic shower development more exact. Figure 4.2 depicts a comparison of the two definitions for copper. Grindhammer and Peters chose:

$$E_c = 2.66 \left(\mathrm{X}_0 \frac{Z}{A} \right)^{1.1} \tag{4.12}$$

as approximation for E_c in MeV [49, 59]. The effective radiation length for compounds or a mixture of material can be calculated via:

$$\frac{1}{X_{0_{eff}}} = \sum_j \frac{w_j}{X_{0_j}}, \tag{4.13}$$

with w_j the fractions by weight and X_{0_j} the radiation length of the j^{th} element.

Muons ($\mu^{\pm}$) have except for their higher mass the same properties as electrons. If r_e in Formula 4.3 is substituted with Formula 4.4 and the muon mass ($m_\mu = 105.658\,\mathrm{MeV}$) instead of the electron mass ($m_e = 510.999\,\mathrm{keV}$) is used, an approximation for the muons energy loss through bremsstrahlung is achieved. Thereby muons loose a factor of $\left(\frac{m_e}{m_\mu}\right)^2 \approx 2.339 \cdot 10^{-5}$ less energy over the equal distance and material than electrons. The same approximation leads to a critical energy E_c of roughly 310 GeV for muons in lead. Therefore very high muon energies are needed to produce an electromagnetic shower. Should there be new physics leading to muons with energies above 1 TeV, calorimetry will gain importance for the muon energy resolution.

4.2 Energy Loss of Photons

Photon interaction in matter is dominated by three processes, as their absolute cross sections σ are the highest over certain photon energy ranges. Sorted by the photons energy the photoelectric effect (up to some keV), Compton scattering (in the order of MeV) and pair production in the nuclear field (above 100 MeV) are the main contributions to the total interaction cross section. These depend on the material traversed, as shown in Figure 4.3 for a light (carbon) and a heavy element (lead). Pair production is the most important process for the electromagnetic shower development.

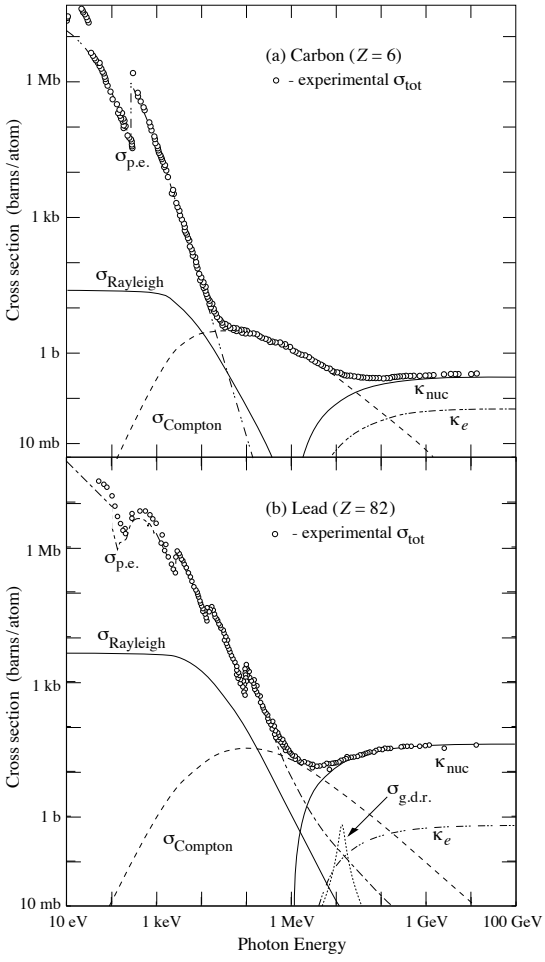

Figure 4.3: Total cross section as a function of photon energy for carbon and lead, showing contributions of different processes: $\sigma_{p.e.}$ = Atomic photoelectric effect, $\sigma_{Rayleight}$ = Rayleight coherent scattering, $\sigma_{Compton}$ = Incoherent Compton scattering of an electron, $\kappa_{nuc/e}$ = Pair production in presence of a nuclear/electron Coulomb field, $\sigma_{g.d.r}$ = Photonuclear reactions (giant dipole resonance) [16].

4.2.1 Photoelectric Effect

If a photons energy exceeds the electrons binding energy in an atom ${}^{A}_{Z}X$, it can be absorbed and a free electron is emitted:

$$ {}^{A}_{Z}X + \gamma \rightarrow {}^{A}_{Z}X^{+} + e^{-}. \tag{4.14} $$

For photon energies below the binding energy the electron may be lifted into a higher shell. The vacant space in the lower shell is refilled and results in either characteristic X-ray or Auger electron emission. The K-shell has the largest contribution to the total photoelectric absorption cross section $\sigma_{p.e.}$. It shows a proportionality $\propto \frac{Z^5}{E_\gamma^{\frac{7}{2}}}$ for $E_\gamma \lesssim m_e c^2$ and $\propto \frac{Z^{3\ldots4}}{E_\gamma}$ for $E_\gamma \gg m_e c^2$. Sharp edges occur if E_γ reaches the difference of the K-shell binding energy to other electron shells as depicted in the low energy part of Figure 4.3.

4.2.2 Compton Scattering

Compton scattering describes the energy loss of a photon by interaction with a loosely bound electron. The Compton effect cross section is exactly described by the Klein-Nishina formula, which for $E_\gamma \gg m_e c^2$ is approximated by [60]:

$$ \sigma_{Compton} = \frac{Z \pi r_e^2 m_e c^2}{E_\gamma} \left[\frac{1}{2} + \ln \left(\frac{2E_\gamma}{m_e c^2} \right) \right]. \tag{4.15} $$

The photons energy after Compton scattering $E_\gamma^{'}$ can be derived using the conservation of energy and momentum as:

$$ E_\gamma^{'} = \frac{E_\gamma}{1 + \frac{E_\gamma}{m_e c^2} (1 - \cos \theta_\gamma)}, \tag{4.16} $$

with the scattering angle θ_γ measured between incident and scattered photon direction. Participating electrons gain the highest possible kinetic energy E_e^{kin} in a back-scattering process ($\theta_\gamma = \pi$):

$$ E_e^{kin}(\theta_\gamma = \pi) = E_\gamma \frac{2 \left(\frac{E_\gamma}{m_e c^2} \right)}{1 + 2 \left(\frac{E_\gamma}{m_e c^2} \right)}. \tag{4.17} $$

For $E_\gamma \gg m_e c^2$ a the fraction is approximately one and therefore $E_e^{kin} \approx E_\gamma$ follows.

4.2.3 Pair Production

High energetic photons (above 1 GeV) almost exclusively interact via pair production with matter as can be evinced in Figure 4.3. Conservation of momentum requires a second particle for the photon to convert into an electron-positron pair. The nucleus Coulomb field is, except for Hydrogen, stronger and therefore has a larger spacial expansion than an

electrons field. This results in different orders of contribution to the total pair production cross section σ_{pair} depending on the materials Z. This effect is visible in Figure 4.3 above 10 GeV ($\frac{\kappa_{nuc}}{\kappa_e}(Z=82) > \frac{\kappa_{nuc}}{\kappa_e}(Z=6)$). An energy threshold for this process is given by:

$$E^{min}_{\gamma,pair} = 2m_e c^2 \left(1 + \frac{m_e}{m_{nucleus}}\right). \tag{4.18}$$

The second term is of very small orders and therefore deniable for most practical cases. Bremsstrahlung radiation and pair production Feynman diagrams are variations of one another. This is reflected in the closely related cross section formulas of these two processes. For E_γ greater than 1 GeV it is reasonable to approximate the total cross section with:

$$\sigma_{pair} = \frac{7}{9}\left(\frac{A}{N_A \mathrm{X}_0}\right). \tag{4.19}$$

X_0 therefore is $\frac{7}{9}$ of the mean free path for high energetic photons before pair production. Stated the other way around: after passing matter with a thickness of $\frac{9}{7}\,\mathrm{X}_0$ only a fraction of $\frac{1}{e}$ photons survives unconverted. The energy of the incident photon in first order (Born-approximation) is shared symmetrical between the e^+-e^--pair. Just above the pair production threshold (small velocities of e^- and e^+) and large Z the Coulomb effect becomes important, this favors higher positron energies. The cross section for asymmetric energy sharing rises above the uniform for $E_\gamma \geq 1\,\mathrm{GeV}$. Depicted in Figure 4.4 is the energy-partition function $f(\epsilon, Z, x)$ for intermediate Z and various values of the photon energy [61], with $\epsilon = \frac{E_\gamma}{m_e c^2}$ and x the so called energy-partition parameter, defined just below Figure 4.4.

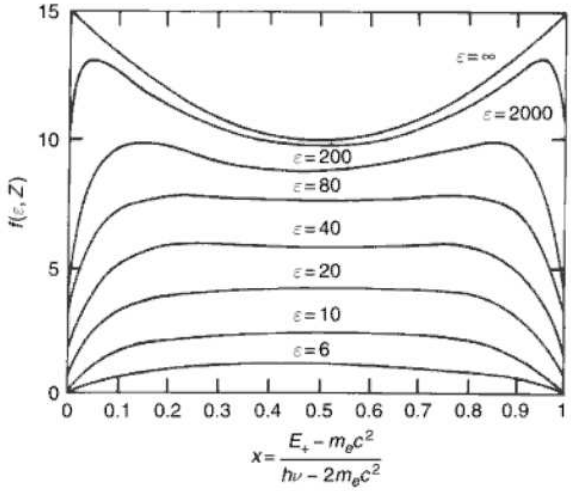

Figure 4.4: Form of the energy-partition function $f(\epsilon, Z, x)$ for pair production at intermediate Z. The total pair production cross section σ_{pair} is given by the area under the curves in units of $\mathrm{Z(Z+1)}\alpha\mathrm{r}_\mathrm{e}^2$ [61]. Pair production in the electron Coulomb field is included in this graph.

4.3 Qualitative Results using a Simple Shower Model

A very simple model is able to describe important features of an electromagnetic shower. For simplicity it is assumed that each photon shall undergo pair-production with exact symmetrical energy partition after traversing one X_0. Each electron and positron shall emit exactly one bremsstrahlung photon per X_0, by which they ought to loose half their energy [58]. This simple model shower shall be initiated by a photon with an energy of E_0. The first cascades using these assumptions are sketched in Figure 4.5. Evolution of

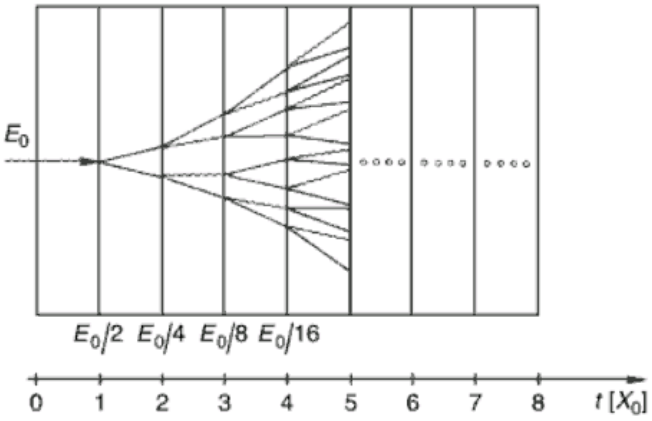

Figure 4.5: Sketch of a simple electromagnetic shower model evolution, initiated by a photon with an energy of E_0 [61].

the number of shower particles can be described as a function of the depth t:

$$N(t) = 2^t. \tag{4.20}$$

Due to the exact energy splitting assumption at each step ($1\,X_0$) the energy of one particle is only dependent on the depth t and initial energy E_0:

$$E(t) = \frac{E_0}{2^t}. \tag{4.21}$$

This cascade continues until the single particles energy falls below or is equal to E_c:

$$E_c \geq \frac{E_0}{2^{t_{max}}}. \tag{4.22}$$

Therefore the position of the shower maximum t_{max} can be calculated via:

$$t_{max} = \frac{\ln\left(\frac{E_0}{E_c}\right)}{\ln(2)}. \tag{4.23}$$

This equation derived from a fairly simple model correctly describes the shower maximum position proportionality to the incident particles energy as $t_{max} \propto \ln\left(\frac{E_0}{E_c}\right)$. Therefore the

design thickness of an electromagnetic calorimeter should rise proportional to the logarithm of the particles maximal anticipated energy.

The electromagnetic shower also has a lateral spread. Opening and emission angles $\Theta_{pair/brems}$ of pair production as well as bremsstrahlung are in the order of $\frac{m_e}{E_{\gamma/e^\pm}}$. Even at E_c the resulting angles are small, therefore these processes contribute only a small part to the lateral development of the shower. Multiple scattering processes dominated by deflections in the Coulomb field of nuclei are primarily responsible for the showers lateral spread. Distribution of the scattering angles are described by Molières theory [62]. Additionally larger scattering angles due to collisions of the charged particles with nuclei contribute. The average multiple scattering angle $\langle\Theta\rangle_{ms}$ at a distance t is given by:

$$\langle\Theta\rangle_{ms} = \sqrt{\frac{4\pi}{\alpha}}\frac{m_e}{E_e}\sqrt{t}. \tag{4.24}$$

Above $t \approx 0.2$ the multiple scattering dominates the two effects mentioned before. For $\langle\Theta\rangle_{ms} \propto \frac{1}{E_e}$ the lateral spread is maximal near the shower maximum. The transverse extension scales fairly exact with the Molière radius [63]:

$$\mathrm{R_M} = \frac{E_s}{E_c}\mathrm{X}_0, \tag{4.25}$$

with E_s the scale energy ($E_s = \sqrt{\frac{4\pi}{\alpha}}m_e \approx 21.2052\,\mathrm{MeV}$) and X_0 using Rossi's definition. A cylinder with the radius of one $\mathrm{R_M}$ contains 90 % of the shower energy. Expanding the radius to $2\,\mathrm{R_M}$ or $3\,\mathrm{R_M}$ includes 95 % or 98 % of the total shower energy. The fact that this radius is not a function of the particles energy is very important. For composite materials the Molière radius may be calculated by:

$$\frac{1}{R_{M_{eff}}} = \frac{1}{E_s}\sum_j \frac{w_j E_{c_j}}{X_{0_j}}. \tag{4.26}$$

This scaling holds up to $3.5\,\mathrm{R_M}$ around the shower axis containing 99 % of the shower energy. Beyond this radius composition effects become important and scaling fails. In shower parametrization this is called the core and everything beyond $3.5\,\mathrm{R_M}$ the tail of the transverse part of an electromagnetic shower.

4.4 Shower Parametrization

The following parameterization approach was developed for a fast simulation of electromagnetic showers. Longitudinal and radial profiles for homogeneous and sampling calorimeters are described. Further the dependence on shower development by materials and the sampling geometry is taken into account. The parametrization was verified with data from the liquid argon calorimeter of the H1 experiment.

An Ansatz by Longo and Sestili for the description of longitudinal shower profiles is used [64]. This Ansatz has been extended to the simulation of individual showers, taking

shower to shower fluctuations and correlations between the longitudinal and radial part of a shower into account. The transversal component parametrization does not show a perfect material independence. Parametrization in homogeneous media builds a base for the shower description in sampling calorimeters. Additional factors taking the material, geometry and sampling structure dependence of the parameters into account are needed for a correct parametrization. The difference mainly results from the transition effect and is depended on the shower depth.

Spatial energy distributions of electromagnetic showers are described by three probability density functions (pdf's):

$$dE(\vec{r}) \;=\; E\, f(t)dt\, f(r)dr\, f(\phi)d\phi. \tag{4.27}$$

The longitudinal shower profile is described by $f(t)$, with t measured in units of radiation length as defined in Formula 4.7. A two component Ansatz is used to describe the radial distribution. The radial distance r from the shower axis is measured in $\mathrm{R_M}$ and ϕ, which is the azimuthal angle. The assumption that the energy distribution is uniform in ϕ yields a constant $f(\phi) = \frac{\pi}{2}$.

4.4.1 Longitudinal Shower Profile in Homogeneous Calorimeters

Average longitudinal shower profiles can be described by a gamma distribution [64]:

$$\left\langle \frac{1}{E}\frac{dE(t)}{dt} \right\rangle \;=\; f(t) \;=\; \frac{(\beta t)^{\alpha-1}\beta e^{-\beta t}}{\Gamma(\alpha)}, \tag{4.28}$$

with

$$\Gamma(\alpha) = \int_0^\infty k^{\alpha-1}e^{-k}dk. \tag{4.29}$$

The depth of the maximum T can be calculated as a fraction of the shape parameter α and the scaling parameter β:

$$T \;=\; \frac{\alpha-1}{\beta}. \tag{4.30}$$

The center of gravity, $\langle t \rangle$, of a shower is calculated by:

$$\langle t \rangle \;=\; \frac{\alpha}{\beta}. \tag{4.31}$$

Rossis analytical studies of longitudinal electromagnetic shower development concluded that by using the energy in terms of E_c and thicknesses in units of $\mathrm{X_0}$ identical results are obtained for all elements [58]. This result is valid for the so called "Approximation B". It states that the Compton effect is disregarded, collision effects are taken into account as constant energy dissipation and further asymptotic formulas are used as an approximation for radiation processes and pair production. The basic assumptions of the "Approximation

B" are better justified in the case of light than heavy elements. For lead the asymptotic expressions used by Rossi predict the radiation loss a factor of 1.5 too high and the probability for pair production is off by a factor of 3. These wrong predictions occur in the lower energy region where the Compton effect and collision processes need to be taken into account.

The proportionality of the depth of the shower maximum, T, to the initial energy E won by the simple shower model is valid up to high energies:

$$T \propto \ln y = \ln \frac{E}{E_c}, \tag{4.32}$$

as predicted by Rossi. Therefore it is possible and for the radial parametrization desired to use T instead of y, the initial energy measured in E_c. The second parameter for the description of the longitudinal shower distribution is α. In homogeneous media it also shows linear proportionality to $\ln y$, though it is material dependent. The index "hom" in the following formulas indicates validity for homogeneous media. Whereas "sam" is used as index for sampling calorimeter parameters.

$$T_{hom} = \ln y + t_1 \tag{4.33}$$
$$\alpha_{hom} = a_1 + (a_2 + a_3/Z) \ln y. \tag{4.34}$$

The values for the coefficients of Formula 4.33 and 4.34 are summarized in the appendix of [49].

4.4.2 Longitudinal Shower Profiles in Sampling Calorimeters

Sampling calorimeters with a complicated but repetitive sampling structure are usually described by a single effective medium. Important material parameters for the shower parametrization may be calculated by the following equations:

$$w_i = \frac{\rho_i d_i}{\sum_j \rho_j d_j} \tag{4.35}$$
$$Z_{eff} = \sum_i w_i Z_i \tag{4.36}$$
$$A_{eff} = \sum_i w_i A_i \tag{4.37}$$
$$E_{c,eff} = X_{0,eff} \sum_i \frac{w_i E_{c,i}}{X_{0,i}} \tag{4.38}$$
$$F_S = \frac{X_{0,eff}}{d_a + d_p} \tag{4.39}$$
$$\hat{e} = \frac{1}{1 + 0.007(Z_p - Z_a)} \tag{4.40}$$

as well as Formula 4.13 and 4.26. The sampling frequency, F_S, and the signal ratio of electrons to minimum ionizing particles, $\hat{e}$, account for the transition radiation effect occurring in sampling calorimeters. Averaged over the whole shower length $\hat{e}$ proofs energy independent for incident particle energies above 1 GeV if the whole shower is contained in the calorimeter [46]. Sampling fluctuations, as scaling of the deposited energy to the visible energy are approximated by a further gamma distribution. The fluctuations and correlations of the parameters are approximated without explicit material or geometry dependence. The highest energy deposition of a shower, which occurs close to the shower maximum T, occurs earlier in a sampling than in a homogeneous calorimeter with the same effective material properties.

Average longitudinal profiles can be parameterized by:

$$T_{sam} = T_{hom} + t_1 F_S^{-1} + t_2(1-\hat{e}) \tag{4.41}$$

$$\alpha_{sam} = \alpha_{hom} + a_1 F_S^{-1}. \tag{4.42}$$

Expectation values of T and α do no longer scale with $\ln y$, but depend on the material and the sampling geometry. Including these sampling fluctuation effects, material and geometry parameters of the ATLAS calorimeter barrel formulas and coefficients resolve to:

$$\langle \ln T_{sam} \rangle = \ln\left(\ln(y) - 0.55 S_F - 0.45\right) \tag{4.43}$$

$$\langle \ln \alpha_{sam} \rangle = \ln\left(0.591 \ln(y) - 0.806 S_F + 0.81\right). \tag{4.44}$$

The values were calculated by [65], with the sampling fraction, S_F, as the inverse of F_S, with

$$X_{0_{eff}} = 22.799\,\text{mm} \tag{4.45}$$

$$E_c = 11.122\,\text{MeV} \tag{4.46}$$

$$S_F = \frac{\cosh(\eta)}{2.5685}. \tag{4.47}$$

These studies were conducted with the goal to implement a shower parametrization into GEANT4 [66], a detailed simulation program for the interaction of particles with detectors. It calculates and follows each particle and its secondaries. Predictions are very accurate, but also very time consuming. This is especially true for electromagnetic showers, where the number of secondary particles is huge, as can be estimated with Formula 4.20. Energy depositions for different electron energies calculated by GEANT4 are provided in Figure 4.6. A standalone fast simulation algorithm for the ATLAS detector proved as being too inaccurate for many physics analysis studies. The successful implementation [65] is the predecessor of a fully integrated package in the ATHENA framework called ATLFAST (A fast simulation package for ATLAS) [67]. Several options for fast simulation are included in the second version called ATLFASTII. A major improvement of this package was the implementation of a so called frozen shower library. This database stores low energetic electromagnetic showers that were simulated by GEANT4. They are used scaled for electrons in energy regions below 1 GeV [68, 69] where the parametrization is not able to

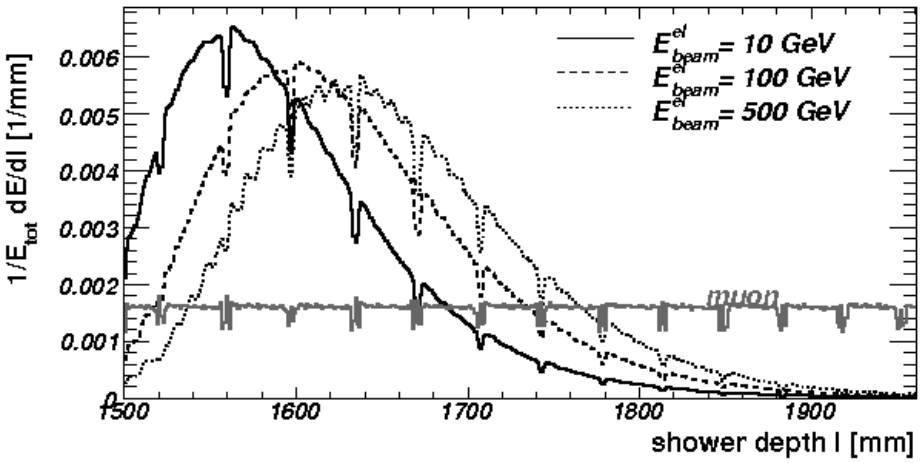

Figure 4.6: GEANT4 prediction of longitudinal electromagnetic shower energy deposition in the ATLAS electromagnetic calorimeter barrel for different incident electron energies, created for the test beam measurements in 2004 [46].

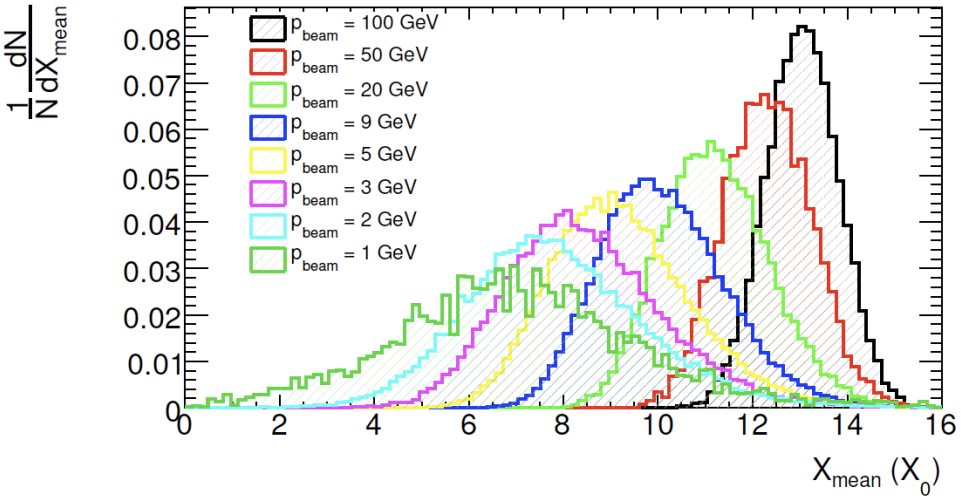

Figure 4.7: Mean shower depth X_{mean} of the ATLAS ECAL barrel measured in X_0 for different electron energies, a result of the combined test-beam run 2004. $X_{mean} = \frac{\sum_{i=0}^{3} E_i X_i^m}{\sum_{i=0}^{3} E_i}$ is comparable with the showers center of gravity, $\langle t \rangle$. Not equal to $\langle t \rangle$, for X_{mean} was calculated using four samples in the longitudinal direction only [47].

describe the shower accurately, as already concluded by [58]. ATLFASTII cuts the average simulation time down by a factor greater than two. In order to use events produced this way for physics analysis studies they always have to be validated with a smaller control sample which was fully simulated by GEANT4 (a so called FullSim sample).

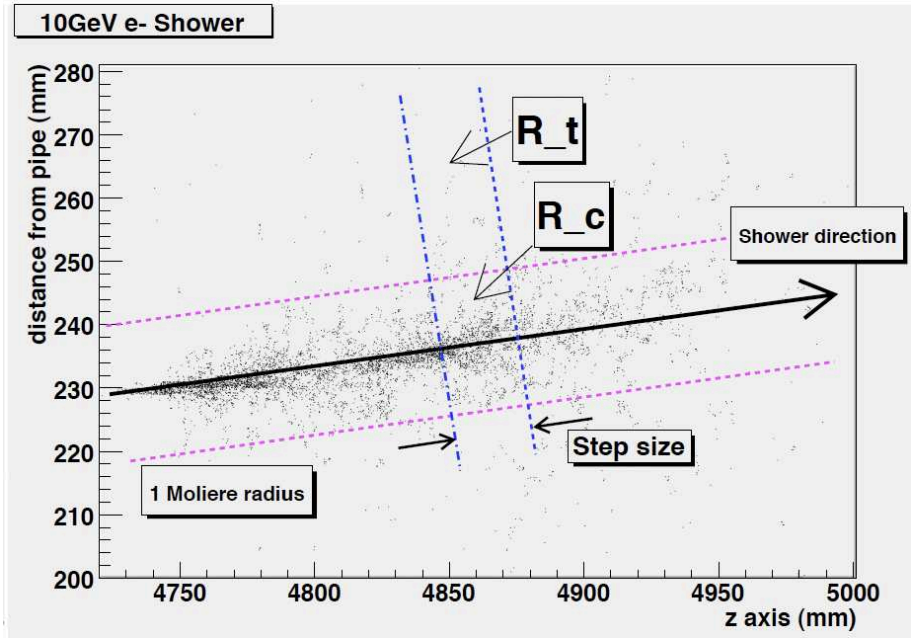

Figure 4.8: Illustration of core R_C and tail R_T of the radial shower distribution. Shown is a GEANT4 generated shower in the ATLAS ECAL initiated by a 10 GeV electron [70].

4.4.3 Radial Shower Profiles

The radial energy distribution

$$f(r) = \frac{1}{dE(t)} \frac{dE(t,r)}{dr} \tag{4.48}$$

is parametrized by an extension of [71]:

$$f(r) = p\frac{2rR_C^2}{(r^2+R_C^2)^2} + (1-p)\frac{2rR_T^2}{(r^2+R_T^2)^2}, \tag{4.49}$$

with $R_{C/T}$ the median of the core or tail and $0 \leq p \leq 1$ a relative probability weight of the core [49]. An illustration of R_C and R_T is provided by Figure 4.8. The distance from the shower axis r is measured in units of $\mathrm{R_M}$. For the ATLAS barrel ECAL $1\,\mathrm{R_M}$ was determinated to be 41 mm [65]. The variable $\tau := \frac{t}{T}$ is introduced. It allows a separation of the energy and material dependence of parameters. R_C is dominated by pair production and bremsstrahlung radiation and therefore increments linearly with τ. R_T shows a rather complicated material and shower depth dependent evolution, as its source are mainly low

energetic photons. Grindhammer and Peters use the following formulas to parametrize R_C, R_T and p:

$$R_{C,hom}(\tau) = z_1 + z_2\tau \tag{4.50}$$

$$R_{T,hom}(\tau) = k_1 \cdot \left[e^{\{k_3(\tau-k_2)\}} + e^{\{k_4(\tau-k_2)\}}\right] \tag{4.51}$$

$$p_{hom}(\tau) = p_1 \cdot e^{\left[\frac{p_2-\tau}{p_3} - e^{\left(\frac{p_2-\tau}{p_3}\right)}\right]}, \tag{4.52}$$

the used coefficients may be found in the appendix of [49].

Longitudinal and radial shower developments are correlated. Introducing the actual center of gravity

$$\langle t\rangle_i = \frac{\alpha_i}{\beta_i} = T_i\frac{\alpha_i}{\alpha_i - 1} \tag{4.53}$$

and by substituting τ with τ_i in Formulas 4.50, 4.51, and 4.52 :

$$\tau = \frac{t}{T} \longrightarrow \tau_i = \frac{t}{\langle t\rangle_i} \cdot \frac{e^{\langle \ln\alpha\rangle}}{e^{\langle \ln\alpha\rangle} - 1} \tag{4.54}$$

this effect is taken into account. The influence of a sampling geometry is small on the radial shower profiles. Minor deviations occur at the very beginning of the shower. With increasing depth the profiles approach shapes found in homogeneous media with the appropriate effective material. The mentioned differences for the radial distribution are corrected by:

$$R_{C,sam} = R_{C,hom} + z_1(1-\hat{e}) + z_2F_S^{-1}e^{-\tau_i} \tag{4.55}$$

$$R_{T,sam} = R_{T,hom} + k_1(1-\hat{e}) + k_2F_S^{-1}e^{-\tau_i} \tag{4.56}$$

$$p_{sam} = p_{hom} + (1-\hat{e}) \cdot \left(p_1 + p_2F_S^{-1}e^{-(\tau_i-1)^2}\right). \tag{4.57}$$

The accordion structure of the ATLAS electromagnetic calorimeter amplifies the correlation between longitudinal and radial profile. Therefore a modified gamma function was introduced to describe the core and tail of the transversal energy distribution [65].

$$\left\langle \frac{1}{dE(t)}\frac{dE(t,r)}{dr} \right\rangle = p^r g_1(r) + (1-p^r)g_2(r) \tag{4.58}$$

$$g_i(r) = \frac{1}{2\lambda_i^r}\left(\frac{r}{\lambda_i^r}\right)^{\left(\frac{\alpha_i^r}{2}-1\right)} \frac{e^{-\sqrt{\frac{r}{\lambda_i^r}}}}{\Gamma(\alpha_i^r)} \tag{4.59}$$

$$p^r = p^r(\tau, y) \tag{4.60}$$

$$\alpha_i^r = \alpha_i^r(\tau, y) \tag{4.61}$$

$$\lambda_i^r = \lambda_i^r(\tau, y). \tag{4.62}$$

Explicit formulas for Equations 4.60, 4.61 and 4.62 with the values of their parameters calculated for an energy range from 0.1 GeV to 50 GeV are given in [65]. The validity

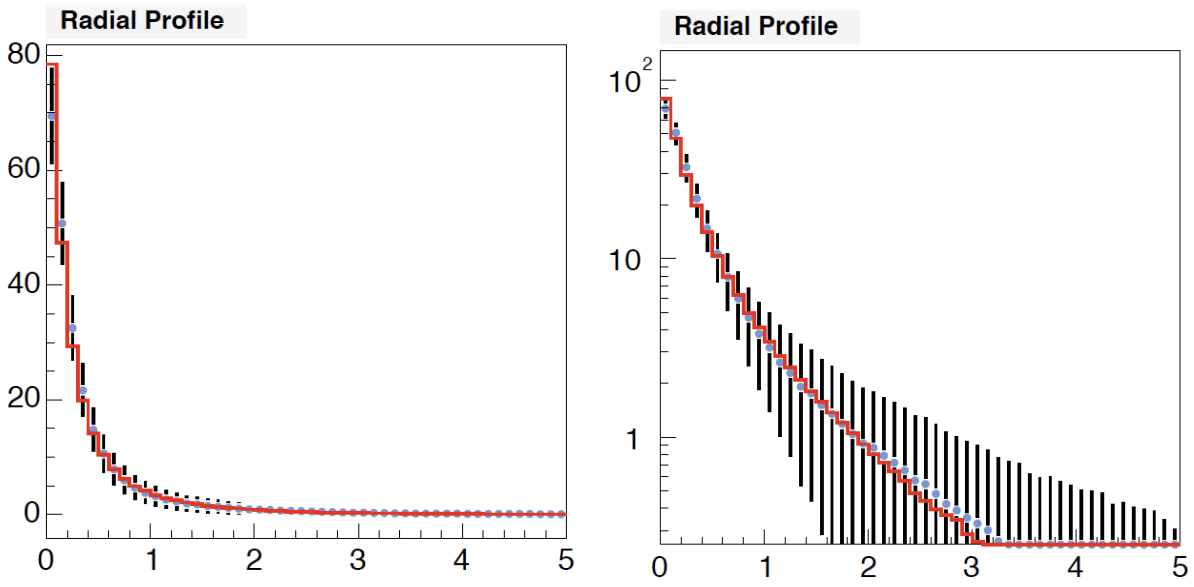

Figure 4.9: Comparison of radial shower shape obtained by parametrization (red histogram) and full GEANT4 simulation (blue dots with black error bars), created by an 10 GeV electron in the ECAL barrel at 0.65 η. In both plots (left: linear and right: logarithmic scale of the y-axis) the x-axis denotes the distance from the shower axis in R_M and the y-axis the energy deposited in arbitrary units [65].

for this radial parametrization was concluded from 1 GeV up to 100 GeV. A comparison of the radial shower distribution obtained by this parametrization and the full GEANT4 simulation is given by Figure 4.9.

The mean radial profiles integrated over the complete shower depth $\left\langle \frac{1}{E}\frac{dE(r)}{dr} \right\rangle$ are independent of incident particles energy.

5 The Reweighting Method and Improvement Studies

This chapter will cover a short motivation for the reweighting method and the implementation of the shower shape correction factors. An overview over the tools used in the ATLAS ATHENA reconstruction framework [1] is given. Then the reweighting algorithm is introduced. Further improvement ideas for this algorithm are studied. Conclusions of the studies and a short description of the implementation are given. The term electron will be used as a collective term for positrons and electrons, as their high energy interaction and therefore produced electromagnetic showers are indistinguishable.

5.1 Motivation

In ATLAS, studies are performed for estimation of the discovery potential of the neutral MSSM Higgs boson. They concluded that for low Higgs boson masses the decay into a τ-lepton pair is a well performing search channel [45, 13]. This is true for the light SM Higgs, H, in the vector boson fusion channel and the three neutral MSSM Higgs bosons, $h/A/H$, in b-associated production. The τ-lepton is not stable and thus decays into further particles. The different decay modes are summarized in Table 5.1. A secondary vertex tagging by the ID may be possible for τ leptons, as their mean free path before decay is $c\tau_L \approx 87\,\mu$m (with a mean life-time $\tau_L = (290.6 \pm 1.0) \times 10^{-15}\,$s) [16].

τ-decay mode	Fraction
$\tau^{\pm} \rightarrow e^{\pm}\bar{\nu_e}\nu_\tau$	17.84 %
$\tau^{\pm} \rightarrow \mu^{\pm}\bar{\nu_\mu}\nu_\tau$	17.36 %
$\tau^{\pm} \rightarrow h^{\pm}\, neut.\, \nu_\tau$	48.26 %
$\tau^{\pm} \rightarrow h^{\pm}h^{\pm}h^{\pm}\, neut.\, \nu_\tau$	14.65 %
all others	1.89 %

Table 5.1: The main τ-decay modes given in percent ($h^{\pm}$ stands for $\pi^{\pm}$ or $K^{\pm}$, neut. for γ's and/or π^0's) [16].

[1] version 14.4.0 was used for this work

The above mentioned studies identified several important backgrounds for the $h/A/H \rightarrow \tau\tau \rightarrow ll+4\nu$ channel. The dominant and not reducible background is the $Z \rightarrow \tau\tau \rightarrow ll+4\nu$ channel. Z bosons are produced in the Drell-Yan process and $Z+jets$, which will occur at high rates. Another background is due to the $W^{\pm}$ boson production, as heir production rate is estimated to be ten times higher than the production rate of Z boson. This contribution has to be considered. Other backgrounds for this signal channel with lower production rates are analyzed in References [45, 13].

For efficient reconstruction of the $h/A/H \rightarrow \tau\tau \rightarrow ll + 4\nu$ signal the $Z \rightarrow \tau\tau \rightarrow ll + 4\nu$ background has to be estimated with sufficient precision. The invariant $\tau\tau$-mass spectrum for signal and background is illustrated in Figure 5.1. The high energy tail of the invariant $Z \rightarrow \tau\tau \rightarrow ll + 4\nu$ mass distribution is caused by the large uncertainty of the missing transverse energy measurement ($E_{T,miss}$) [45]. A good estimation is therefore crucial for the signal extraction.

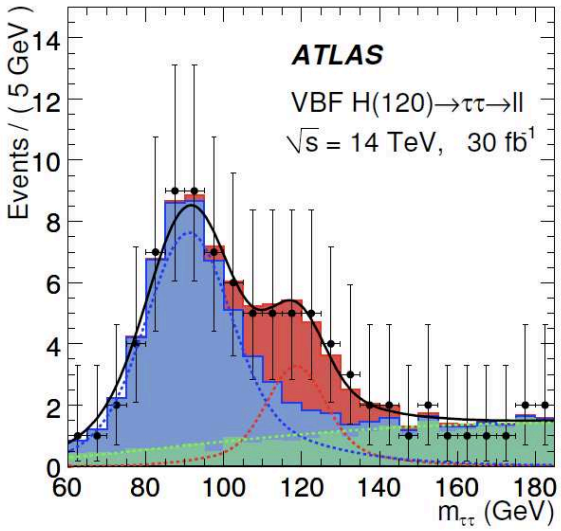

Figure 5.1: Invariant mass distribution for a 120 GeV neutral Higgs boson signal, considering only the pure leptonic decay channel together with background. The signal (red) is situated on top of the $Z \rightarrow \tau\tau$ (blue), the summed $W+Jets$ and top pair background (green). No pile-up is considered in this plot [45].

The goal of the analysis is to obtain a data-driven method to estimate the invariant $Z \rightarrow \tau\tau \rightarrow ee + 4\nu$ mass distribution from a very pure (97.3 %) sample of $Z \rightarrow ee$ events. This was first developed in [14]. The tools utilized by this method, the method itself and possible improvements will be described in the following.

5.2 Analysis Tools

The *tauRec* package of the ATHENA framework is used for τ lepton reconstruction and utilizes the TopoCluster algorithm [45]. It shall therefore be described shortly.

The TopoCluster algorithm, opposed to a sliding window algorithm, provides a variable cluster size. This avoids out-of-cluster energy leakage, as shown in Figure 5.2 for a schematic electromagnetic shower with a sliding window cluster. Both algorithms use cell energy splitting for cells belonging to more than one cluster. This avoids energy overestimation by double counting of energy depositions.

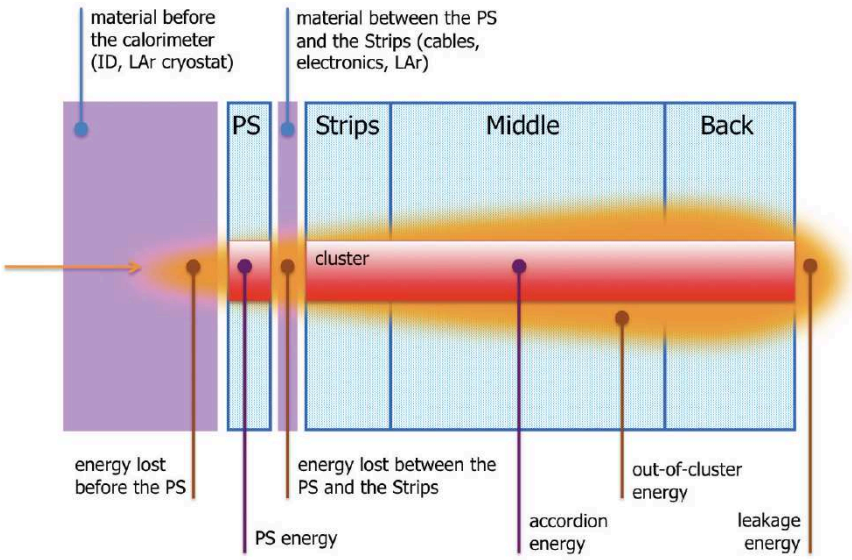

Figure 5.2: Schematic electromagnetic shower (orange) in the ATLAS LAr EMB, using a sliding window clustering algorithm (red) [47].

The sliding window algorithm scans the ECAL with a 5×5-cell window [72]. Clusters are build, wherever a local transverse energy maximum is found. The cluster sizes are refined in the barrel depending on the particle hypothesis, $N_\eta^{cell} \times N_\phi^{cell} = 3 \times 7$ for electrons or converted photons and to $N_\eta^{cell} \times N_\phi^{cell} = 3\times5$ for unconverted photons. Advantages of this algorithm are a very precise cluster energy calibration and its efficiency for electromagnetic shower reconstruction. A different approach, the TopoCluster algorithm is efficient at suppressing noise in clusters with large numbers of cells. It is used for jet and missing transverse energy reconstruction. Furthermore the topological clustering algorithm was found to be more efficient for τ reconstruction. It is based on signal to noise ratio of cells. Noise levels are estimated by the root mean square of the expected electronic noise. If a cell exceeds a certain signal-to-noise threshold, t_{seed}, it is used as a seed of a TopoCluster. In the next iterative step the neighbour cells are scanned, whether they exceed a second threshold, $t_{neighbour}$, unless they are seeds themselves. Cells not used as seeds and with a level above $t_{neighbour}$ are then added to the cluster. This step is repeated until no further neighbours fulfill the requirements. The last iteration adds the neighbours of all cells belonging to the TopoCluster, which have a ratio greater than t_{all}. Merger and Splitter algorithms are applied on the resulting clusters. The Splitter separates topological clusters if they contain spacial separated seed cells forming local maxima within one cluster. This allows to determinate the individual particle energy depositions, even if their topological

clusters overlap. Threshold parameters can be set by choosing a certain setting. "EM 633" and "Had 420" are available in the standard ATLAS reconstruction package, the threshold parameters are given in Table 5.2.

Setting	EM 633	Had 420
Calorimeter	EM only	All
Seed signal definition	E	$\|E\|$
Cluster cut before splitting	$E_T > 5\,\text{GeV}$	$E_T > 0\,\text{GeV}$
t_{seed}	6	4
$t_{neighbour}$	3	2
t_{all}	3	0

Table 5.2: Settings and thresholds for topological cluster available in the standard ATLAS reconstruction package [72].

The clustering algorithm can be extended to more than one sampling of the calorimeter by switching the option "all3D" on. In the "Had 420" setting the option "super3D" is available, which allows cells of other calorimeter parts, like the tile calorimeter, to be added to a TopoCluster.

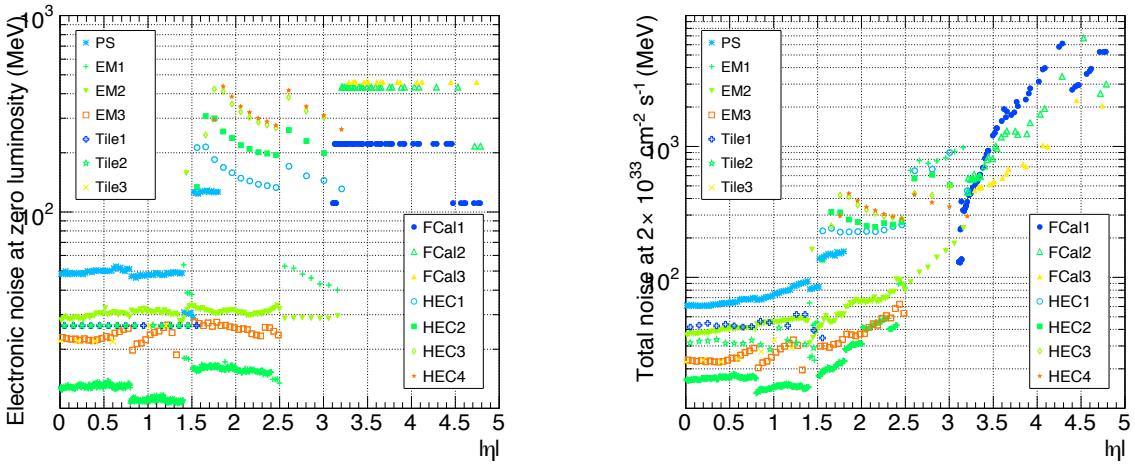

Figure 5.3: Expected noise level of calorimeter cells in different layers plotted over the pseudorapidity $|\eta|$, for zero luminosity (left) and at design luminosity including anticipated pile up (right) [43].

The "Had 420" setting is optimized to find low energy clusters and at the same time avoids a overwhelming noise contribution. A so called CaloNoiseTool provides a cell by cell noise calculation. The use of this tool reduces the number of expected TopoClusters

initiated by pure noise. With the "Had 420" setting at full luminosity below 12 clusters, considering 187562 cells. For the "EM 633" setting less than one pure noise initiated cluster per event was calculated with an input of 172160 cells (for $|\eta| < 2.5$) [72]. The following studies were conducted using the "Had 420" setting with the "super3D" option.

For *tauRec* TopoClusters with an energy above 1 GeV form a seed for a TopoJet. This TopoJet object contains all TopoClusters within a cone of $\Delta R < 0.4$. The definition of the distance ΔR in the $\eta - \phi$ plane is defined by:

$$\Delta R = \sqrt{(\Delta\eta)^2 + (\Delta\phi)^2}. \tag{5.1}$$

As ΔR is independent of the radial distance to the beam pipe it describes a cone originating at the IP. TopoJets containing an energy above 7 GeV are added to the Cone4H1TopoJet class. Cell weights are determinated and applied in order to minimize the jet energy resolution. This cell weighting algorithm is based on the same principle used at the H1 detector. A TopoJet is declared as a τ-candidate, if its transverse energy E_T exceeds 10 GeV. Further a τ-candidate has to be detected within a region of $|\eta| < 2.5$. As the last step all tracks within a cone $\Delta R < 0.3$ with a $p_T > 2$ GeV are associated with the τ-candidate.

Studies performed in the course of this diploma thesis showed, that $\approx 85\,\%$ of the τ-candidates associated with electrons consist of exactly one TopoCluster. The majority of the remaining is comprised of two TopoClusters. Whereas three or more clusters per candidate are seldom and add up to less than a percent.

Additional identification variables calculated by a package called *egammaRec* were used. This package is optimized for electron and photon reconstruction. Energies of the electrons of $Z \to ee$, their charges and their quality, at least medium electrons, were used from the *egamma*-container. The most important attribute why *egamma* information was used is the better charge reconstruction ability of the *egammaRec* package if compared to the *tauRec* package.

5.3 Reweighting Method

The reweighting method is based on the cell energy entries of the electromagnetic calorimeter in the ATLAS detector. It makes use of the cells, which are associated with a TopoCluster. In the rest frame of the Z boson both, electrons from $Z \to ee$ and the τ-leptons from $Z \to \tau\tau$, have the same energy of $\frac{m_Z}{2} \approx 45 - 46$ GeV. The τ decay, $\tau \to e + 2\nu$, is a three body decay. Electrons from this three body decay in the Z rest frame have an energy, distributed in a continuous spectrum from approximately 45 GeV down to 0 GeV, which peaks around 20 GeV. Thus the electrons from $Z \to \tau\tau \to ee + 4\nu$ always posses less energy, than electrons from $Z \to ee$ in the Z-restframe. The electron energy which initiates the electromagnetic shower and is measured by the calorimeter is the energy in the labframe. Therefore, the electron energy has to be Lorentz-boosted into the labframe. This can be done using the Z boson four vector as the Lorentz-boost vector.

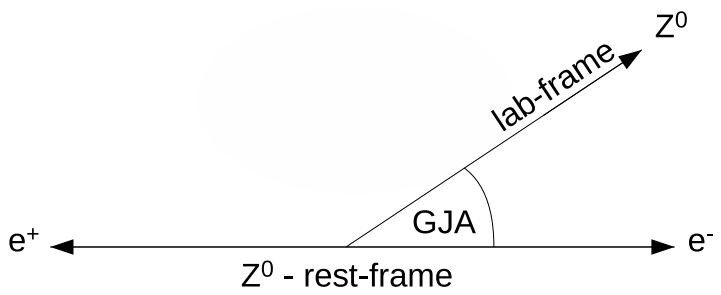

Figure 5.4: Illustrated definition of the Gottfried-Jackson angle θ_{GJA}.

The electron and positron energy distribution was found to depend on the Gottfried-Jackson angle θ_{GJA} [14]. It is the angle between the vectors of the Z boson in the lab frame and the negative lepton in the Z rest frame. This definition is illustrated in Figure 5.4. The θ_{GJA} distribution is flat for $Z \to ee$ and $Z \to \tau\tau$. If θ_{GJA} is calculated from the vector of the observed electron for $Z \to \tau\tau \to ee + 4\nu$ events this flat distribution is degenerated as shown in Figure 5.6.

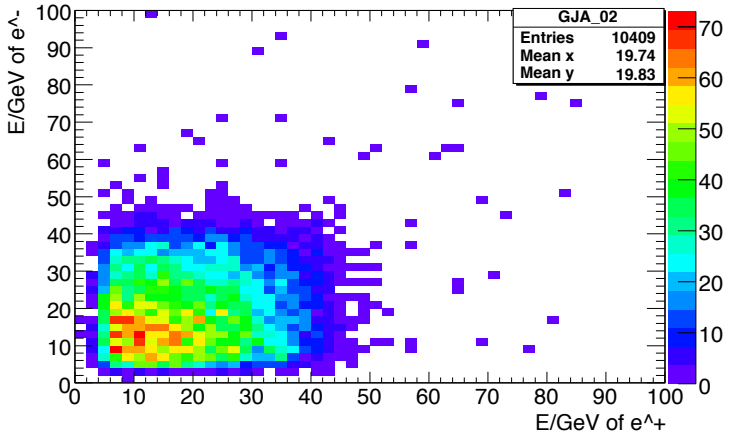

Figure 5.5: Reweighting reference histogram containing reconstructed energies of electron and positrons originating from a $Z \to \tau\tau \to ee + 4\nu$ decay. This plot was obtained using generator level information from Monte Carlo events. Events with $0 < |\theta_{GJA}| < 0.2$ are shown.

Reference plots containing reconstructed electron energies of $Z \to \tau\tau \to ee + 4\nu$ in the Z rest frame were filled for different bins of the Gottfried-Jackson angle. Five reference plots with bin sizes of 0.2 between $0 < |\cos(\theta_{GJA})| < 1$ were created. An example is shown in Figure 5.5. This task as well as most analysis was performed with ROOT, a data analysis framework [73]. To obtain the correct boost, the Z boson four vector which is also needed to calculate θ_{GJA}, is taken from Monte Carlo at generator level.

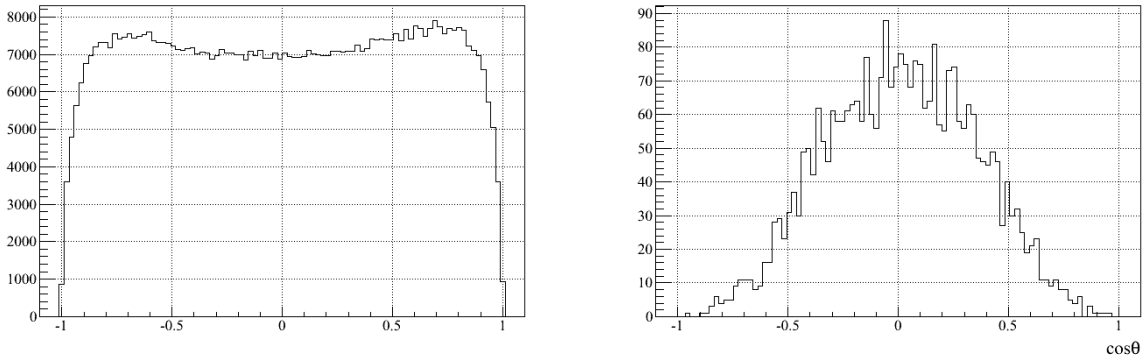

Figure 5.6: Distribution of the Gottfried-Jackson angle for $Z \rightarrow ee$ (left) and $Z \rightarrow \tau\tau \rightarrow ee + 4\nu$ (right) events [74].

Changes in the analysis are introduced: Event Summary Data (ESD) instead of Raw Data Objects (RDOs) was used. The ESD format has the same content as the Derived Physics Data (DPD) format, which will be used when real collision data is available. The cell information used in the reweighting algorithm may only be available in so-called Performance DPDs. Furthermore the *tauRec* package manipulation to read a newly created cell container was bypassed, by directly overwriting the old cell energy entries of the ESD with the reweighted values. Thus the reweighting algorithm was transformed from a *tauRec* plugin into a standalone package.

The reweighting procedure can be summarized by the steps it performs.

- First electrons from a $Z \rightarrow ee$ sample which have to pass several criteria are selected within $|\eta| < 2.5$. Criteria are: passing trigger cuts (two electrons with $E_e > 15\,\text{GeV}$ or one electron with $E_e > 25\,\text{GeV}$), the two electrons must have opposite charge, the calculated invariant mass of the two highest p_T electrons has to be within a window of $75 - 100\,\text{GeV}$ and a selected electron must match with a τ-candidate within a cone of $R < 0.4$. Furthermore both electrons have to exceed a transverse momentum of $p_T > 10\,\text{GeV}$. Together with a cut on the number of jets below three this selection results in a purity of the selected $Z \rightarrow ee$ sample of 97.3 % [14]. Pile-up effects are neglected.

- The second step combines the identified positron and electron to a Z, Lorentz-boosts them into its rest-frame and calculates θ_{GJA}.

- Depending on the θ_{GJA} new energies for the electron and positron are randomly drawn from the corresponding $Z \rightarrow \tau\tau \rightarrow ee + 4\nu$ reference histogram in the third step.

- The fourth step builds new four-vectors and Lorentz-boosts them back into the lab-frame.

- In the fifth step the cell entries of the TopoClusters associated with the τ-candidates are changed with the ratio of the reweighted to the original electron and positron lab-frame energy

$$E_{cell,rew} = E_{cell,orig} \cdot \frac{E_{ref,\tau}}{E_e}. \tag{5.2}$$

- Finally, as the sixth step, ATHENA reconstruction algorithm is rerun on the modified sample. All reconstruction algorithms calculate new values based on the new cell calorimeter entries. The second most important just after the *tauRec* reconstruction is the missing transverse energy measurement ($E_{T,miss}$), as this quantity is needed for the invariant mass calculation of the τ-pair.

5.4 Improvements in Modeling of the $\tau\tau$-Mass Spectrum and Implementation

The electromagnetic shower shape changes with the energy of the incident particle. In the existing reweighting method the rescaled electron energy is smaller than the original one. This change of the showershape is not taken into account. Therefore studies on the impact of this effect in the reweighting method are performed. Three possible improvement and correction options for the existing reweighting algorithm were studied. The maximal energy deposition along the shower axis follows approximately the logarithm of the initial electrons energy. The impact on the measured values and implementation possibilities in the algorithm was studied. Equivalent studies were conducted for the transversal part of the electromagnetic shower. An examination of the impact of taking into account the different Gottfried-Jackson angle distributions of the used $Z \rightarrow ee$ events and goal $Z \rightarrow \tau\tau \rightarrow ee+4\nu$ decay conclude this chapter.

5.4.1 Longitudinal Shower Shape Correction

To consider and correct for the shift of energy deposited in the direction of the shower axis has the largest potential for improvement of the reweighting algorithm. The pointing geometry of the ATLAS ECAL cells, as shown in Figure 3.12, proved to be advantageous for the calculations. Four sampling layers are available in the electromagnetic calorimeter, the presampler, strip, middle and the back layer, as illustrated in Figure 3.12. The studies have shown, that the sum of the energy deposited in the presampler and the last layer does not exceed approximately 5 % of the TopoCluster energy. Considering this, but also in view of the energy calibration and scaling uncertainty in first data these two layers, are neglected from now on.

The average energy deposited in each layer may be calculated via the longitudinal shower parametrization formula, by integrating over the beginning t_{j-1} and end t_j of each layer in

units of X_0.

$$dE(t) = E \int_{t_{j-1}}^{t_j} \frac{(\beta t)^{\alpha-1} \beta e^{(-\beta t)}}{\Gamma(\alpha)} dt \tag{5.3}$$

The sampling lengths and material in front of the calorimeter according to Figure 3.13 were used. Examples of used parametrization functions for different energy values are shown in Figure 5.7. The ratio of the layer energy content to the whole shower energy were calculated for five bins in pseudorapidity, $|\eta|$: [0−0.6], [0.6−0.8], [0.8−1.35], [1.55−1.8] and [1.8−2.5]. The region $1.35 < |\eta| < 1.55$ was omitted, due to the overlap of two calorimeters. This results in a complicated cell geometry, which makes a parametrization Ansatz very hard to implement. Showers occurring in this region are reweighted linearly. A fine tuning modification of the dead material in front of the calorimeter was performed. The latest detector description database implemented in the ATHENA framework showed deviations to the information used as shown in Figure 3.13. For this purpose, an evaluation of the minimum of a function resulting from the difference of measured to the by parametrization predicted fractions of the energy deposition in each layer per $|\eta|$ bin was performed. The evaluation resulted in the additional dead material in front of the ECAL used for the parametrization.

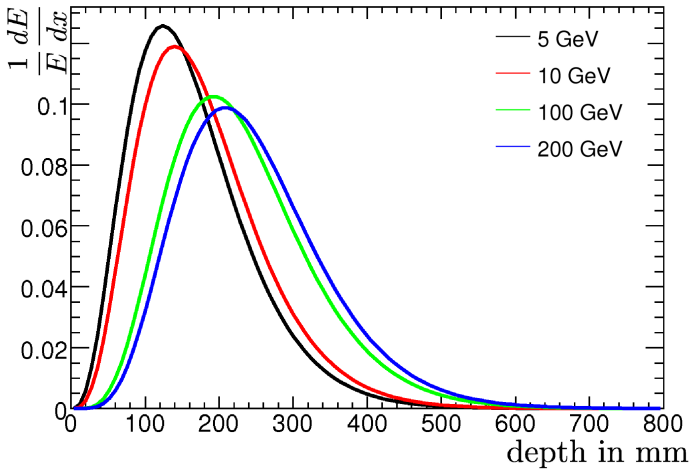

Figure 5.7: Shown are unscaled functions valid for $|\eta| < 0.6$ for different incident particle energies. The correction factors are calculated by integrating over a function with the appropriate energy. The depth of the layer dictates the integration borders. This value is then scaled by the sum won by integrating over all active layer intervals of the ECAL. The same procedure is performed with energies in steps of 10 GeV up to 200 GeV. The correction ratio is calculated from the fraction of two of these numbers for different energies, per layer. These are filled in histograms read out in the reweighting process.

After the validation of the longitudinal shower energy deposition parametrization correction factors for the strip and middle layer were calculated for each $|\eta|$ bin. These values were saved in reference histograms, from which they are read out during the reweighting

process. This technique uses less computing time than the calculation of four parametrization integrals per event. A correction factor considers the energy of the electron in the lab-frame before and after reweighting in bins of 10 GeV from zero up to 200 GeV.

The correction factor is calculated as a ratio of two fractions. The first fraction is the energy deposited by the reweighted electron in one layer divided by the whole deposited energy of this electron. The second fraction considers the same value for the reconstructed electron energy in the same layer. One correction factor is calculated per layer and possible energy combination.

The correction factor is multiplied to the right side of Equation 5.2. The higher the shower energy the more of the overall energy is deposited in the second layer and less in the first layer. During the reweighting procedure it is required that the new energy randomly drawn from reference histograms is smaller than the original one. The reason for this requirement is that an electron from a τ decay, which itself originated from a Z decay cannot have more energy than an electron coming directly from a Z decay, in the Z rest frame. The Lorentz-boost and directions stay the same. Therefore the longitudinal shower shape correction factors for the strip layer are always greater than one and for the second layer smaller than one. Figure 5.8 shows two examples of longitudinal shower shape correction factor histograms.

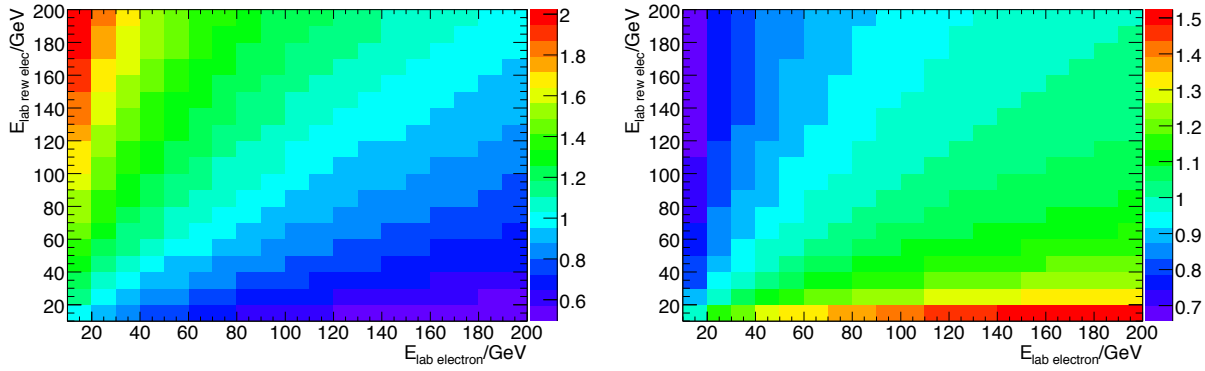

Figure 5.8: Reference histograms for longitudinal shower shape correction factors. Shown for $|\eta| < 0.6$ strip layer (left) and middle layer (right). The factor is read out according to the energy of the electron before and after the reweighting in the lab-frame.

5.4.2 Transversal Shower Shape Correction

The radial distribution of an electromagnetic shower changes with the energy, if considering one value of t ($t := \frac{x}{X_0}$). The calorimeter measures energy within entities, called cells. In case of the ATLAS detector, only the cells from the middle layer electromagnetic calorimeter are used for transversal shower distribution observation in this study. In contrast to the strip layer a symmetrical distribution in the $\eta - \phi$ plane is found. A shower axis originating in the IP was built using the mean of the energy weighted sum of all cell coordinates, which

belong to one TopoCluster. Then histograms containing energy weighted entries over the distance of a cell to the shower axis were filled. Only small differences are observed for different electron energies. This was confirmed applying the radial parametrization. The second layer is more than four times deeper than the first layer. The mean radial profiles integrated over the complete shower depth $\left\langle \frac{1}{E}\frac{dE(r)}{dr} \right\rangle$ are independent of incident particles energy. For electron energies above 25 GeV in average more than 70 % of the detected shower energy is contained in the middle layer. The great depth of the second layer therefore is responsible for the small visible deviations of the radial part of the shower shape. Therefore no significant changes in the radial shower distribution can be extracted from data. These, if significant, could have been corrected for by the use of a further correction factor. An example of detected transversal energy deposition of TopoClusters is shown in Figure 5.9. The energy dependence of the radial electromagnetic shower distribution is therefore not accounted for in the reweighting process.

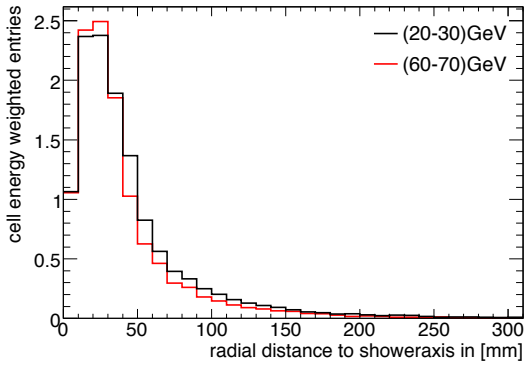

Figure 5.9: Visible radial distribution of a TopoCluster. Shown is the energy weighted sum over the cells of many TopoClusters, scaled to their integral within $10 - 250$ mm (noise entries beyond the shown interval exist), within two energy ranges as a function of the distance from the calculated TopoCluster axis.

5.4.3 Gottfried-Jackson Angle Correction

The observable difference in the Gottfried-Jackson Angle distributions, as depicted in Figure 5.6, does not influence the reweighting process. But it would have to be accounted for in the invariant mass distribution if calculated from a reweighted $Z \to ee$ instead of a $Z \to \tau\tau \to ee + 4\nu$ sample. The possibility of θ_{GJA}-correction factors calculated as a ratio of entries in the histograms shown in Figure 5.6 was studied. Bins of $|\cos\theta_{GJA}| = 0.1$ were chosen, because the distribution is symmetrical to the y-axis. The θ_{GJA}-correction factors were used as multiplicative weights for the calculated invariant $\tau\tau$-mass. The distribution resulting from the θ_{GJA}-correction weighted $Z \to ee$ samples showed a significantly worse agreement with the $Z \to \tau\tau \to ee + 4\nu$ sample than the not θ_{GJA}-corrected distribution. Further investigations revealed, that the selection made for before the reweighting

process created a subsample, witch shows an almost similar $\cos\theta_{GJA}$ compared to the $Z \to \tau\tau \to ee + 4\nu$ sample. Further cuts which are necessary for the use of the collinear approximation, explained in the next chapter, were applied. The collinear approximation is used to calculate the invariant $\tau\tau$-mass. After applying these criteria the $\cos\theta_{GJA}$ distributions agree much better, as shown in Figure 5.10.

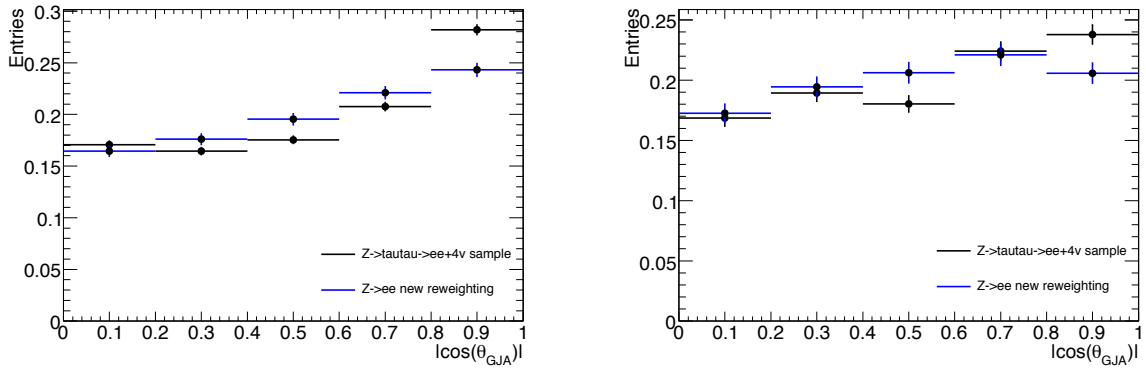

Figure 5.10: Gottfried-Jackson angle distribution of reweighted $Z \to ee$ samples and $Z \to \tau\tau \to ee + 4\nu$ samples, after applying the reweighting selection (left) and after the cuts necessary for the application of the collinear approximation (right).

Thus the result of this study is, that the different $\cos\theta_{GJA}$ distributions observed in $Z \to \tau\tau \to ee + 4\nu$ and $Z \to ee$ event samples do not have to be accounted for, if the cuts necessary for the collinear approximation are applied.

6 Data-driven Determination of the $\tau\tau$-Mass Spectrum

6.1 The Collinear Approximation

To reconstruct the energy of a τ-lepton which decayed into an electron the energy carried away by the two neutrinos has to be taken into account. The only weakly interacting neutrinos carrying a part of the τ-lepton momentum remain undetected. Nevertheless by the introduction of approximations and making use of certain assumption, described next, the invariant $\tau\tau$-mass, can be reconstructed.

The Z-mass is large compared to the τ-mass, therefore the τ-leptons are strongly Lorentz-boosted. Decay products of the boosted τ-lepton have approximately the same direction of flight. The measured missing transverse momentum may thus be allocated to the ν's as their direction is known to be approximately parallel to the electrons ($\vec{p}_{T,miss} = \sum_{i=1}^{4} \vec{p}_{T_{\nu_i}}$). This assumes that all missing transverse momentum originates from the neutrinos. Figure 6.1 illustrates this procedure called the collinear approximation. Z bosons with a transverse momentum of zero following the $Z \rightarrow \tau\tau \rightarrow ee{+}4\nu$ decay chain would also yield a measured missing transverse momentum of zero. Therefore the requirement of $p_{T_Z} \neq 0$ has to be introduced for validity of the collinear approximation.

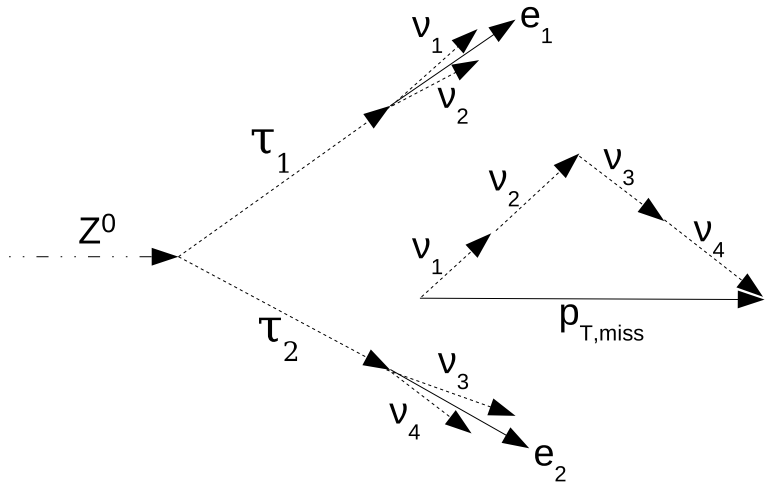

Figure 6.1: Illustration of the collinear approximation of the $Z \rightarrow \tau\tau \rightarrow ee + 4\nu$ decay. The missing transverse momentum is estimated as the sum of the p_T of the neutrinos.

A τ-pair emitted back-to-back in the lab frame, originating from Z boson decay would produce a non detected missing transverse momentum ($\vec{p}_{T,miss} = 0$). The reason is, that the sum of the not detected neutrinos from this decay compensates to zero in the transverse plane. An event with $\vec{p}_{T,miss} = 0$ cannot be used for the collinear approximation. Therefore in data a selection of back-to-back emitted leptons in the lab frame is avoided by a cut on the angle between them, requiring $|\Delta\Phi_{ll}| < 3$.

The invariant mass of the $\tau\tau$-system is calculated as:

$$m_{\tau\tau}^2 = (p_{\tau_1} + p_{\tau_2})^2 \,, \tag{6.1}$$

with the four momentum of the tau leptons

$$p_{\tau_i} = \begin{pmatrix} E_{\tau_i} \\ \vec{p}_{\tau_i} \end{pmatrix} . \tag{6.2}$$

With the relation $p_\tau^2 = m_\tau^2$ Formula 6.1 yields:

$$m_{\tau\tau}^2 = 2\left(m_\tau^2 + p_{\tau_1} \cdot p_{\tau_2}\right), \tag{6.3}$$

since $\frac{2m_\tau^2}{m_{\tau\tau}^2} \approx 8 \cdot 10^{-4}$, the τ-lepton mass can be neglected. Applying the assumptions stated above the p_T conservation of this decay chain yields:

$$\vec{p}_{T,\tau_1} + \vec{p}_{T,\tau_2} = \vec{p}_{T,e_1} + \vec{p}_{T,e_2} + \vec{p}_{T,miss}, \tag{6.4}$$

with

$$\vec{p}_{T,\tau_i/e_i} = \begin{pmatrix} p_{x,\tau_i/e_i} \\ p_{y,\tau_i/e_i} \end{pmatrix} \quad \text{and} \quad \vec{p}_{T,miss} = \begin{pmatrix} p_{x,miss} \\ p_{y,miss} \end{pmatrix} . \tag{6.5}$$

The introduction of x_i, the fraction of the τ_i momentum carried away by the detectable decay product, the electron e_i:

$$x_i \cdot \vec{p}_{T,\tau_i} = \vec{p}_{T,e_i}, \tag{6.6}$$

allows a substitution of $\vec{p}_{T,\tau_i}$ in Equation 6.4. This yields formulas for the calculation of the x_i's:

$$x_1 = \frac{p_{x,e1} \cdot p_{y,e2} - p_{y,e1} \cdot p_{x,e2}}{p_{y,e2} \cdot p_{x,miss} - p_{x,e2} \cdot p_{y,miss} + p_{x,e1} \cdot p_{y,e2} - p_{y,e1} \cdot p_{x,e2}} \tag{6.7}$$

$$x_2 = \frac{p_{x,e1} \cdot p_{y,e2} - p_{y,e1} \cdot p_{x,e2}}{p_{x,e1} \cdot p_{y,miss} - p_{y,e1} \cdot p_{x,miss} + p_{x,e1} \cdot p_{y,e2} - p_{y,e1} \cdot p_{x,e2}}. \tag{6.8}$$

Substituting p_{τ_i} in Formula 6.3 yields:

$$m_{\tau\tau}^2 \approx 2\left(\frac{p_{e_1} \cdot p_{e_2}}{x_1 \cdot x_2}\right). \tag{6.9}$$

Since also the electrons mass is negligibly small, the final result is:

$$m_{\tau\tau}^2 \approx \left(\frac{m_{ee}^2}{x_1 \cdot x_2}\right) \quad \Rightarrow \quad m_{\tau\tau} \approx \frac{m_{ee}}{\sqrt{x_1 \cdot x_2}}, \tag{6.10}$$

which contains only experimentally measurable quantities. Physical values of x_i are constrained to $x_i \in (0, 1)$. The $p_{T,miss}$-resolution is known to be limited. A discrepancy of around 10 % between $p_{T,miss}$ and $\sum_{i=1}^{4} p_{T_{\nu_i}}$ exists, as shown by studies, for example performed in Reference [13]. Therefore in some cases x_i's calculated from measured values are not within the range $(0, 1)$. These events cannot be subjected to the collinear approximation.

6.2 Comparison of the Result of a Reweighted $Z \to ee$ sample with a $Z \to \tau\tau \to 2e + 4\nu$ sample

The invariant $\tau - \tau$ mass, $m_{\tau-\tau}$, of the reweighted $Z \to ee$ sample will be compared to a $Z \to \tau\tau \to ee + 4\nu$ sample containing approximately the same number of events. For this study a sample containing 45000 $Z \to ee$ events was reweighted using the method described. This corresponds to an integrated luminosity of $\mathcal{L}_{int} = 30\,\mathrm{pb}^{-1}$. The $Z \to \tau\tau \to ee + 4\nu$ sample used for comparison contains exactly the same number of events as the reweighted sample.

In the following $m_{\tau\tau}$ distributions were calculated via the collinear approximation for both samples. These were then scaled with their integral value for better comparability. Two tests were applied to each histogram to evaluate their agreement. The tests were applied to distributions in an energy range from 40 GeV to 190 GeV, to avoid bins with no entries. The χ^2 test for histogram comparison is sensitive to bin-by-bin differences, while the Kolmogorov test evaluates the integrated difference.

Three $m_{\tau\tau}$ distributions using the same samples but with different cuts applied are shown. The cuts are given below each pair of histograms and the results of the applied tests are stated in the upper right corner of the right histogram. The left histogram shows the scaled histograms in a larger energy range, from 0 GeV to 250 GeV, this way the high energy tails are visible. Basic cuts were applied on both samples. This is necessary, as otherwise the selection criteria applied on the $Z \to ee$ before reweighting, would introduce a bias for this sample compared to the $Z \to \tau\tau \to ee + 4\nu$ sample. The common criteria applied on all distributions shown are:

- The pseudorapidity has to fulfill $|\eta| < 2.5$
- The trigger cuts: two leptons with $E > 15\,\mathrm{GeV}$ or one lepton with $E > 25\,\mathrm{GeV}$
- A cut on the angle between the leptons: $|\Delta\Phi_{ll}| < 3$, to avoid back to back emitted leptons

- The match of a medium electron and positron with a τ-candidate within a cone of $\Delta R < 0.4$
- And $x_i \in (0, 1)$ which is necessary to use the collinear approximation, therefore to calculate the entries of the following plots

The cut applied on the distribution shown in Figure 6.3, $x_i \in (0, 0.75)$, is usually not applied for leptonic decay studies. Both test in this plot show bad results. It was included, as it shows a tremendous mass shift of the distribution to higher masses. Reweighting and rescaling techniques are known to induce a mass shift compared to the distributions which they should mimic. Studying the difference, in correlations of the quantities which are used for the calculation invariant mass distribution, between target and reweighted sample might help to find further improvement possibilities.

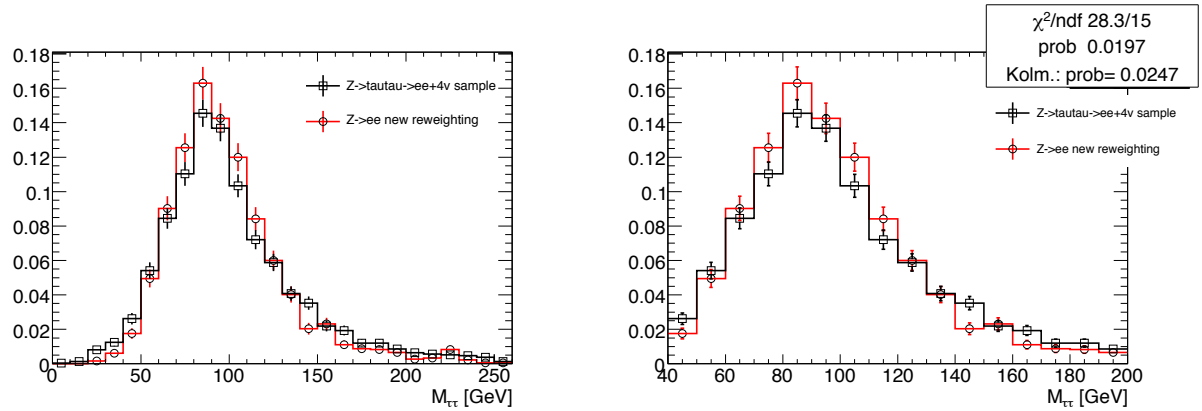

Figure 6.2: Invariant mass distribution, $m_{\tau\tau}$, with only the common and collinear approximation cuts applied ($0 < x_i < 1$).

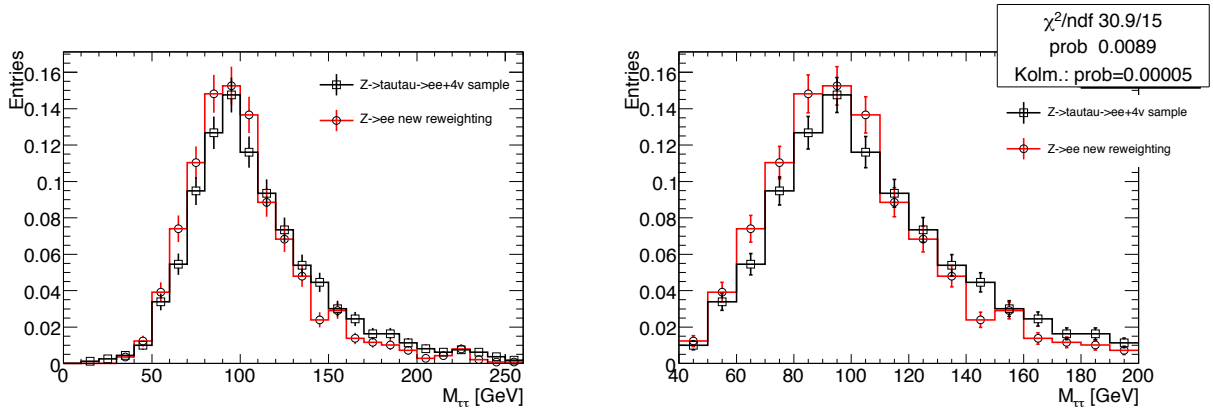

Figure 6.3: Invariant mass distribution, $m_{\tau\tau}$, with harder collinear approximation cuts applied ($0 < x_i < 0.75$). This cut was found to be used in some studies with hadronically decaying τ leptons.

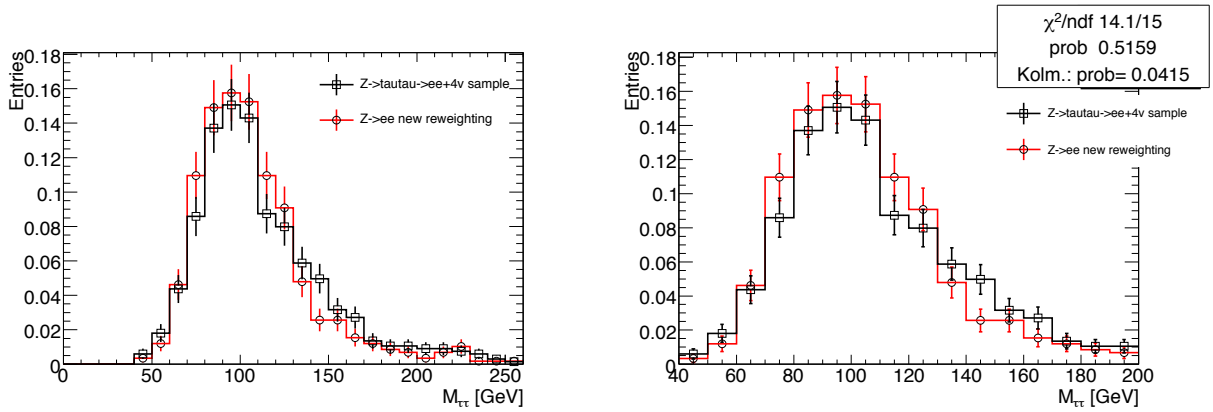

Figure 6.4: Invariant mass distribution, $m_{\tau\tau}$ with some selected cuts used for MSSM $H(@130\,GeV) \rightarrow \tau\tau$ studies [13].

The histograms in Figure 6.4 show distributions, with a selection of cuts used in a study of b-quark associated Higgs production decaying into a $\tau\tau \rightarrow 2l + 4\nu$ [13].
The selection criteria applied are the following:

- The invariant lepton-lepton mass has to lie within a $[0, 70\,\text{GeV}]$ window
- A harder cut on x_i, by demanding: $0 < x_1 \cdot x_2 < 0.5$
- Further a cut on the angle between the leptons: $2 < |\Delta\phi_{ll}| < 3$
- The highest allowed p_T of a lepton is $80\,\text{GeV}$
- A missing transverse momentum of $p_{T,miss} > 15\,\text{GeV}$
- Each lepton has to fulfill $p_T > 10\,\text{GeV}$

These selections are also used in studies for the MSSM light Higgs signal channel, therefore this set should be named as the most relevant one. After these cuts the reweighting method should deliver an invariant $\tau\tau$-mass distribution as close as possible to the real measured $Z \rightarrow \tau\tau \rightarrow ee + 4\nu$ distribution. In this study this was performed wit Monte Carlo simulated data of both channels to study the method.

7 Conclusion and Outlook

The method for simulating of the $\tau\tau$-mass shape $Z \rightarrow \tau^+\tau^- \rightarrow e^+e^- + 4\nu$ from future data was refined. From selected $Z \rightarrow e^+e^-$ events the electron and the positron energies are rescaled. These are drawn randomly from reference histograms containing reconstructed energies of electrons and positrons from simulated $Z \rightarrow \tau^+\tau^- \rightarrow e^+e^- + 4\nu$ events. The rescaling is done on calorimeter cell level. Additional correction factors take also the change of the electromagnetic shower shape due to the modified electron and positron energy is accounted. These depend on the position of each rescaled cell in the shower and in the calorimeter. For the computation of the correction factors an electromagnetic shower shape parametrization was customized for the ATLAS calorimeter. The reweighted samples are re-reconstructed. The changes made in the calorimeter cell entries are thereby taken into account when recalculating the τ-energies and momenta as well as in the re-computation of the missing transverse momentum, $p_{T,miss}$. These quantities are input to compute the invariant $\tau\tau$-mass, $m_{\tau\tau}$, distribution, which is determined in the collinear approximation. It assumes that the neutrinos, due to the high boost of the τ-leptons from the Z-decay, are emitted in the same direction as the electrons. The assumed direction of flight of the neutrinos allows to identify $p_{T,miss}$ with the sum of the neutrino momenta. These assumptions permit a calculation of the invariant $\tau\tau$-mass from values measured by the detector. The $m_{\tau\tau}$ distribution derived from $Z \rightarrow ee$ data can then be used as background shape for the $Z \rightarrow \tau^+\tau^- \rightarrow e^+e^- + 4\nu$ channel in $h/A/H \rightarrow \tau^+\tau^- \rightarrow l^+l^- + 4\nu$ analysis. Applying Higgs selection cuts does not change the good agreement of the $m_{\tau\tau}$ distribution derived with this method. The well reconstructable $Z \rightarrow e^+e^-$ signal provides a good estimation of the invariant $\tau\tau$-mass shape of the $Z \rightarrow \tau^+\tau^- \rightarrow e^+e^- + 4\nu$ channel for first data.
Due to the minimal influence of Monte Carlo information this method is largely model independent and can be used at low integrated luminosities. An update with the actual values of dead material in front of the electromagnetic calorimeter should be performed before application to real data. This information might be available soon after first ATLAS data will be taken. A recalculation of the longitudinal shower shape correction factors will then be necessary.
Possible improvements to the corrections developed here could be achieved by the individual parametrization for each reweighted shower and the input of the exact cell geometries using the detector description tool. This would however extend the time per reweighting process significantly. A similar method could be applied for hadronically decaying τ-leptons, since parametrizations also exist for hadronic showers. The preparation of a proper reference sample and the projection of the results to hadronic τ-jets is however

more complex than for leptonic τ-decays, studied here.

The method developed in this thesis is directly applicable to ATLAS data and provides an important contribution to the background estimation in Higgs searches from data.

List of Figures

List of Tables

Bibliography

[1] J. J. Thomson. Cathode rays. *Phil. Mag.*, 44:293–316, 1897.

[2] C. D. Anderson. The positive Electron. *Phys. Rev.*, 43:491–494, 1933.

[3] Carl D. Anderson and Seth H. Neddermeyer. Cloud Chamber Observations of Cosmic Rays at 4300 Meters Elevation and Near Sea-Level. *Phys. Rev.*, 50:263–271, 1936.

[4] S. H. Neddermeyer and C. D. Anderson. Note on the Nature of cosmic Ray Particles. *Phys. Rev.*, 51:884–886, 1937.

[5] Murray Gell-Mann. A Schematic Model of Baryons and Mesons. *Phys. Lett.*, 8:214–215, 1964.

[6] G. Zweig. An SU(3) model for strong interaction symmetry and its breaking. CERN-TH-401.

[7] S. L. Glashow. Partial Symmetries of Weak Interactions. *Nucl. Phys.*, 22:579–588, 1961.

[8] A. Salam. *in Elementary Particle Theory, p. 367.* Almqvist and Wiksell, Stockholm, 1968.

[9] Steven Weinberg. A Model of Leptons. *Phys. Rev. Lett.*, 19:1264–1266, 1967.

[10] P. W. Higgs. Broken symmetries and the masses of gauge bosons. *Phys. Rev. Lett.*, 13:508–509, 1964.

[11] G. Arnison et al. Experimental observation of lepton pairs of invariant mass around 95 $\frac{\mathrm{GeV}}{\mathrm{c}^2}$ at the CERN SPS collider. *Phys. Lett.*, B126:398–410, 1983.

[12] Combined CDF and DØ Upper Limits on Standard Model Higgs-Boson Production with up to 4.2 fb^{-1} of Data. arXiv:0903.4001 [hep-ex]. 2009.

[13] J. Schaarschmidt. A Study of b-Quark Associated Higgs Production in the Decay Mode $b\bar{b}\,h/A/H \to \tau\tau \to 2l + 4\nu$ with ATLAS at LHC. Diploma Thesis. TU Dresden (2007).

[14] K. Leonhardt. Determination of $Z \to \tau^+\tau^- \to e^+e^- + 4\nu$ Background Shapes from Data in Context of the $b-$Quark Associated Higgs Boson Production with ATLAS at the LHC. Diploma Thesis. TU Dresden (2008).

[15] Stephen P. Martin. A Supersymmetry Primer. arXiv:9709356 [hep-ph]. 1997.

[16] C. Amsler et al. *Phys. Lett.*, B667:1, 2008.

[17] M. Herrero. The Standard model. arXiv:9812242 [hep-ph]. 1998.

[18] F. J. Yndurain. Limits on the mass of the gluon. *Phys. Lett.*, B345:524–526, 1995.

[19] B. Pontecorvo. Mesonium and antimesonium. *Sov. Phys. JETP*, 6:429, 1957.

[20] B. Pontecorvo. Inverse beta processes and nonconservation of lepton charge. *Sov. Phys. JETP*, 7:172–173, 1958.

[21] B. Pontecorvo. Neutrino experiments and the question of leptonic-charge conservation. *Sov. Phys. JETP*, 26:984–988, 1968.

[22] V. N. Gribov and B. Pontecorvo. Neutrino astronomy and lepton charge. *Phys. Lett.*, B28:493, 1969.

[23] J. F. Donoghue, E. Golowich, and B. R. Holstein. *Dynamics of the Standard Model*. Cambridge, Great Britain: University Press, 1992. ISBN 0-521-47652-6.

[24] F. Halzen and A. D. Martin. *Quarks and leptons: an introductory course in modern particle phyics*. New York, USA: Wiley, 1984. 396p. ISBN 0-471-88741-2.

[25] David Griffiths. Introduction to elementary particles. Weinheim, USA: Wiley-VCH (2008) 454 p. ISBN 0-471-60386-4.

[26] C. Burgess and G. Moore. *The Standard Model, A Primer*. Cambridge, Great Britain: University Press, 2007. 396p. ISBN 0-521-86036-9.

[27] Jeffrey Goldstone, Abdus Salam, and Steven Weinberg. Broken Symmetries. *Phys. Rev.*, 127:965–970, 1962.

[28] P. W. Higgs. Spontaneous Symmetry Breakdown Without Massless Bosons. *Phys. Rev.*, 145:1156–1163, 1966.

[29] W. Greiner and B. Müller. *Theoretische Physik, Band 8, Eichtheorie der schwachen Wechselwirkung*. Thun, Germany: Harri Deutsch, 1986. ISBN 3-87144-712-9.

[30] M. Gomez-Bock, M. Mondragon, M. Mühlleitner, M. Spira, and P. M. Zerwas. Concepts of Electroweak Symmetry Breaking and Higgs Physics. arXiv:0712.2419 [hep-ph]. *CERN-PH-TH/2007-262*, 2007.

[31] R. Barate et al. Search for the standard model Higgs boson at LEP. *Phys. Lett.*, B565:61–75, 2003.

[32] Abdelhak Djouadi. The Higgs sector of supersymmetric theories and the implications for high-energy colliders. *Eur. Phys. J.*, C59:389–426, 2009.

[33] Rudolf Haag, Jan T. Łopuszanski, and Martin Sohnius. All Possible Generators of Supersymmetries of the S Matrix. *Nucl. Phys.*, B88:257, 1975.

[34] Sidney R. Coleman and J. Mandula. All possible Symmetries of the S Matrix. *Phys. Rev.*, 159:1251–1256, 1967.

[35] Hitoshi Murayama. Supersymmetry phenomenology. arXiv:0002232 [hep-ph]. 2000.

[36] Abdelhak Djouadi. The Anatomy of electro-weak symmetry breaking. II. The Higgs bosons in the minimal supersymmetric model. *Phys. Rept.*, 459:1–241, 2008.

[37] L. Evans, (ed.) and P. Bryant, (ed.). LHC Machine. *JINST*, 3:S08001, 2008.

[38] R. Adolphi et al. The CMS experiment at the CERN Large Hadron Collider. *JINST*, 3:S08004, 2008.

[39] K. Aamodt et al. The ALICE experiment at the CERN Large Hadron Collider. *JINST*, 3:S08002, 2008.

[40] A. A. Alves et al. The LHCb Detector at the CERN Large Hadron Collider. *JINST*, 3:S08005, 2008.

[41] G. Anelli et al. The TOTEM experiment at the CERN Large Hadron Collider. *JINST*, 3:S08007, 2008.

[42] O. Adriani et al. The LHCf detector at the CERN Large Hadron Collider. *JINST*, 3:S08006, 2008.

[43] ATLAS Collaboration. G.Aad et al. The ATLAS Experiment at the CERN Large Hadron Collider. *JINST 3 (2008) S08003*, 2008.

[44] D. Froidevaux and P. Sphicas. General-Purpose Detectors for the Large Hadron Collider. *Annu. Rev. Nucl. Part. Sci.*, 56:375–440, 2006.

[45] G. Aad et al. Expected Performance of the ATLAS Experiment - Detector, Trigger and Physics. arXiv:0901.0512v4 [hep-ex]. 2009.

[46] M. Aharrouche et al. Energy linearity and resolution of the ATLAS electromagnetic barrel calorimeter in an electron test- beam. *Nucl. Instrum. Meth.*, A568:601–623, 2006.

[47] M. Delmastro, M. Aleksa, T. Carli, R. Froesch, and I. Wigerter-Seez. Response of the ATLAS Liquid Argon Electromagnetic Calorimeter to Electrons from 1 to 100 GeV at the 2004 ATLAS Combined Test-Beam . *ATL-COM-LARG-2009-014*, 2009. not yet approved.

[48] ATLAS Collaboration. ATLAS Detector and Physics Performance. Technical Design Report. *CERN-LHCC-99-14/CERN-LHCC-99-15*, 1999.

[49] G. Grindhammer and S. Peters. The Parameterized Simulation of Electromagnetic Showers in Homogeneous and Sampling Calorimeters. arXiv:0001020 [hep-ex]. 1993.

[50] F. Bloch. *Ann. d. Physik*, 16:285, 1933.

[51] F. Bloch. *Z. Physik*, 81:363, 1933.

[52] H.A. Bethe. Zur Theorie des Durchgangs schneller Korpuskularstrahlen durch Materie. *Ann. d. Physik*, 5:325–400, 1930.

[53] H.A. Bethe. *Z. Physik*, 76:293, 1932.

[54] H.A. Bethe. *Handbuch der Physik*, 24:273, 1933.

[55] Seltzer S.M. Sternheimer, R.M. and M.J. Berger. Density effect for the ionization loss of charged particles. *Phys. Rev.*, B26:6067, 1982.

[56] W.F.G. Swann. Theory of energy loss of high energy particles. *J. Franklin Inst.*, 226:598, 1938.

[57] E. Fermi. The Ionization Loss of Energy in Gases and in Condensed Materials. *Phys. Rev.*, 57:485–493, 1940.

[58] B. Rossi. *High-Energy Particles*. Prentice-Hall, Inc., Englewood Cliffs, NJ, 1952. 569 p., Library of Congress Catalog Card Number: 52-8625.

[59] O. I. Dovzhenko and A. A. Pomansky. *Soviet Physics (JETP)*, 18:187, 1964.

[60] O. Klein and Y. Nishina. *Z. Physik*, 52:853&869, 1929.

[61] C. Grupen and B. A. Schwartz. *Particle detectors - Second Edition*. Camb. Monogr. Part. Phys. Nucl. Phys. Cosmol., 2008. 651 p., ISBN 978-0-521-840006-4.

[62] G. Moliére. *Winkel- und räumliche Verteilung der Elektronenkomponente der großen Luftschauer*. Springer, Berlin, 1953.

[63] W. Ralph Nelson, Theodore M. Jenkins, Richard C. McCall, and Joseph K. Cobb. Electron induced Cascade Showers in Copper and Lead at 1 GeV. *Phys. Rev.*, 149:201–208, 1966.

[64] E. Longo and I. Sestili. Monte Carlo Calculation of Photon Initiated Electromagnetic Showers in Lead Glass. *Nucl. Instrum. Meth.*, 128:283, 1975.

[65] E. Barberio and A. Straessner. Parameterization of electromagnetic shower for the ATLAS detector. *ATL-COM-PHYS-2004-015*, 2004.

[66] S. Agostinelli et al. GEANT4: A simulation toolkit. *Nucl. Instrum. Meth.*, A506:250–303, 2003.

[67] E. Richter-Was and D. Froidevaux. ATLFAST 2.0, A fast simulation package for ATLAS. *ATL-PHYS-98-131*, 1998.

[68] E. Barberio et al. The GEANT4-based ATLAS fast electromagnetic shower simulation. *ATL-SOFT-CONF-2007-002*, 2007.

[69] E. Barberio et al. Fast shower simulation in the ATLAS calorimeter. *J. Phys. Conf. Ser.*, 119:032008, 2008.

[70] W. Ehrenfeld. (Fast) Shower Simulation in ATLAS - Talk given at the DESY Computing seminar 07.01.2008 . www.desy.de/dvsem/WS0708/ehrenfeld_talk.pdf.

[71] G. Grindhammer, M. Rudowicz, and S. Peters. The fast Simulation of Electromagnetic and Hadronic Showers. *Nucl. Instrum. Meth.*, A290:469, 1990.

[72] W Lampl, S. Laplace, D. Lelas, P. Loch, H. Ma, S. Menke, S. Rajagopolan, D. Rousseau, S. Snyder, and G. Unal. Calorimeter Clustering Algorithms: Description and Performance. *ATL-LARG-PUB-2008-002*, 2008.

[73] R. Brun and F. Rademakers. ROOT: An object oriented data analysis framework. *Nucl. Instrum. Meth.*, A389:81–86, 1997.

[74] M. Mazur. $Z \rightarrow \tau\tau$ Background Estimation using Rescaling - Talk given at the $H \rightarrow \tau\tau$ Meeting 29.07.2009 .

Danksagung

Mein besonderer Dank gilt Anne Pfost, der wunderbaren Frau an meiner Seite, die während der Schreibphase dieser Arbeit viel Geduld für mich aufgebrachte, es schaffte "nichtphysikalische" Verpflichtungen von mir fernzuhalten, mich Zeit meines Studiums mit ihrer Energie und ihrem Blick für die schönen Seiten und Aspekte des Lebens motivierte und immer wieder aufbaute.

Ein besonderer Dank gilt Prof. Michael Kobel, welcher mich in seiner Gruppe im Institut für Kern- und Teilchenphysik aufgenommen hat und mir damit die Chance gab an diesem spannenden Thema zu arbeiten. Desweiteren gilt mein Dank Dr. Wolfgang Mader, meinem Betreuer und einem Experten auf dem Gebiet der τ-Physik, sowie Jun. Prof. Arno Straessner, der mir vor allem, aber nicht ausschließlich, mit seinem Fachwissen zum Thema Paramerisierungen weiterhelfen konnte.

Weiterer Dank gilt allen Mitgliedern der Teilchenphysikgruppe am IKTP der Technischen Universität Dresden, da Sie durch Freudlichkeit, Hilfbereitschaft und Zusammenhalt wirklich eine wunderbare Arbeitsatmosphäre schaffen.

Besonders erwähnen und bedanken möchte ich mich bei Felix Friedrich, der mit seinen umfangreichen Fachkenntnissen immer eine Lösung für meine leider nicht allzu seltenen IT-Probleme parat hatte, Kathrin Leonhardt, welche die Methode des Reweightings im Zuge Ihrer Diplomarbeit entwickelte und mich in dieses Thema eingeführt hat, sowie es auf sich genommen hat diese Diplomarbeit Korrektur zu lesen. Jana Schaarschmidt gilt mein Dank nicht nur für das blitzartige, aber dennoch sehr genaue, Korrektur lesen, sondern auch und vor allem, dass Sie mich mit den Cuts, welche für das $m_{\tau\tau}$-Spektrum, die kolineare Näherung und für einige spezielle Higgs Szenarien wichtig sind, vertraut gemacht hat. Special thanks also goes to Deepak Kar, as he was so kind to read over my diploma thesis, despite his not existing spare time.

Auch Danken möchte ich meinen Eltern die mir ein sorgenfreies Studium und vor allem das wunderbar lehrreiche und für mich wegweisende Praktikum am SLAC ermöglichten.

Selbständigkeitserklärung

Hiermit versichere ich, dass die vorliegende Arbeit selbständig und ohne unzulässige Hilfe Dritter angefertigt wurde. Keine als die angegeben Quellen und Hilfsmittel wurden genutzt. Resultate aus fremden Quellen sowohl direkt als auch indirekt übernommen, wurden als solche kenntlich gemacht.

Patrick Czodrowski
Dresden, den 09.11.2009